FORSCHUNGSZENTRUM ROSSENDORF
WISSENSCHAFTLICH-TECHNISCHE BERICHTE
FZR-284
Februar 2000

Annual Report 1999

Institute of Safety Research

Editors:
Prof. Dr. F.-P. Weiß
PD Dr. U. Rindelhardt

CONTENTS

Preface

The Institute of Safety Research (ISR) is one of the five scientific institutes of Forschungszentrum Rossendorf e. V.. The Forschungszentrum Rossendorf is a member of the "Wissenschaftsgemeinschaft Gottfried Wilhelm Leibniz". As such it is funded by the Federal Ministry of Education and Research and by the Saxon Ministry of Science and Arts with 50% each.

The work of the institute is directed to the assessment and enhancement of the safety of large technical plants and to the increase of the effectiveness and environmental sustainability of those facilities. Subjects of investigations are equally nuclear plants and installations of process industries. To achieve the above mentioned goals, the institute is engaged in two scientific fields, i. e. thermo-fluid dynamics including magneto-hydrodynamics (MHD) and materials/components safety.

To analyse thermo-fluiddynamic phenomena during normal plant operation and during accidents, basic physical models and computer codes are developed for one and two-phase flows, and for the space and time dependent heat release (neutron kinetics and chemical reaction kinetics). That theoretical work is based on experimental investigations of chemical reaction kinetics including runaway reactions, and of transient, spatial two-phase flows. The institute has started the construction of the multi-purpose TOPFLOW (Transient, Two-Phase Flow) experimental facility. As a first step in task sharing between the different centres of competence the research centres Jülich and Rossendorf decided to transfer the emergency condenser test set-up NOKO (Notkondensator) to Rossendorf where the main components of NOKO shall act as kernel of TOPFLOW. It shall be the specificity of TOPFLOW that it applies advanced two-phase measuring techniques which are developed in the ISR and which allow deep insight into the flow characteristics over a wide range of the void content and flow velocities. Recently a wire mesh sensor was developed that provides an image frequency of 10.000 frames per second with 16 x 16 measuring points per image.

MHD is relevant to flows of electrically conducting fluids, reaching from liquid metals to salt water, when there are inherent electromagnetic fields or when they can externally be imposed. The understanding and modeling of MHD effects offers technological and safety related applications in crystal growth, metallurgy, and other areas. However, the Rossendorf MHD department also deals with basic effects like the self-excitation of the magnetic field of the earth. For that, the Institute of Physics in Riga together with the Rossendorf group designed and constructed a sodium flow experiment in Riga. In November 1999 just during the first test run, a self-induced magnetic field has been observed and clearly been identified as solely caused by the sodium flow. That was for the first time in the world that magnetic field self-excitation was experimentally shown to occur.

In materials safety, the institute is specialised to the investigation of irradiated nuclear reactor materials. The susceptibility of the mechanical properties against neutron and gamma irradiation and the effect of thermal annealing is evaluated by mechanical tests. The microstructural mechanisms of materials degradation are studied by highly resolving methods of structural analyses like TEM and SAXS and by more integrating methods like SANS.

Monte Carlo methods for radiation field calculation have been developed and validated to get reliable information about the fluences to which the components have been exposed. Improved covariance analysis and spectrum adjustment methods are used to adjust the calculated fluences to activation measurements.

Starting from the estimated accident loads (pressure, temperature) and from the mechanical and thermal properties of the concerned components structural models are developed to assess the integrity of those components in the considered scenario. These calculations take into account the thermal and mechanical interaction between the fluids and the components. One scenario that particularly has attracted interest is the in vessel retention of molten corium in an LWR. Together with the Royal Institute of Technology (RIT) in Stockholm where the experiments are being performed, a finite element model is worked out that allows the prediction of the failure mode and the failure time of the reactor vessel. This model treats the thermal convection in the melt pool. The structural part is based on a sophisticated high temperature creep model.

The work of the ISR is closely linked with the activities of the other institutes of the research centre and with neighbouring research institutions. Together with the radiochemical institute, the chemical and physical phenomena are investigated ruling the transport of nuclides in unsaturated zones of soil. Dedicated column experiments were designed that will be operated by both institutes. The data from these experiments are needed to verify the theoretical approaches on which it's codes are based. The ISR together with the Dresden University of Technology and Hochschule für Technik, Wirtschaft und Sozialwesen (HTWS) Zittau/Görlitz constitutes one of the German centres of competence for nuclear energy and nuclear safety. As such it also takes care for the conservation and promotion of expertise in nuclear engineering.

The ISR is engaged in a large number of national and international research projects and activities. Amongst others, ISR contributes to several PHARE/TACIS projects of the EU on the safety of the Russian type VVER reactors. Further, ISR was invited for membership in the Design Institute for Emergency Relief Systems of the American Institute of Chemical Engineers to make available the Rossendorf code BRICK for depressurisation simulations of chemical reactors.

The following graphs give an overview about the sources and deployment of funding between the different research tasks. In 1999, 47% of the total budget came from external sources, with 38% from public research grants and with 9% from research orders mainly by the industry.

Distribution of funding sources 1999

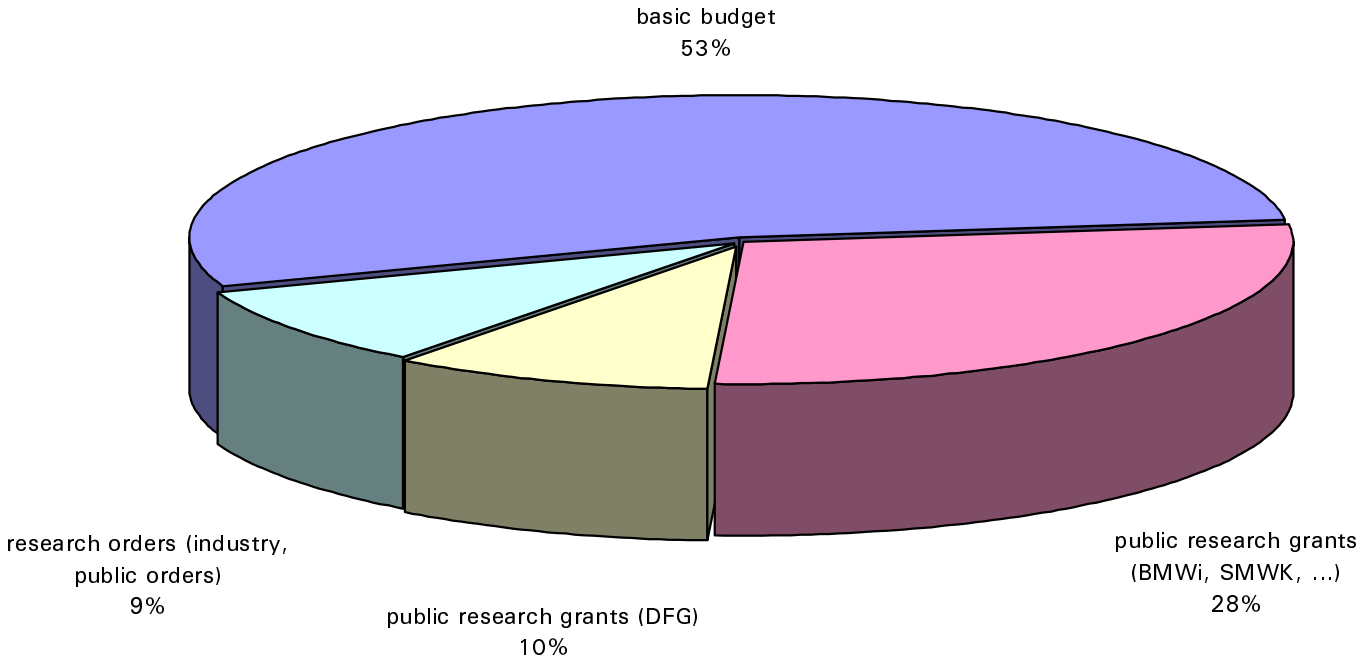

Deployment of funding on the various task/projects 1999

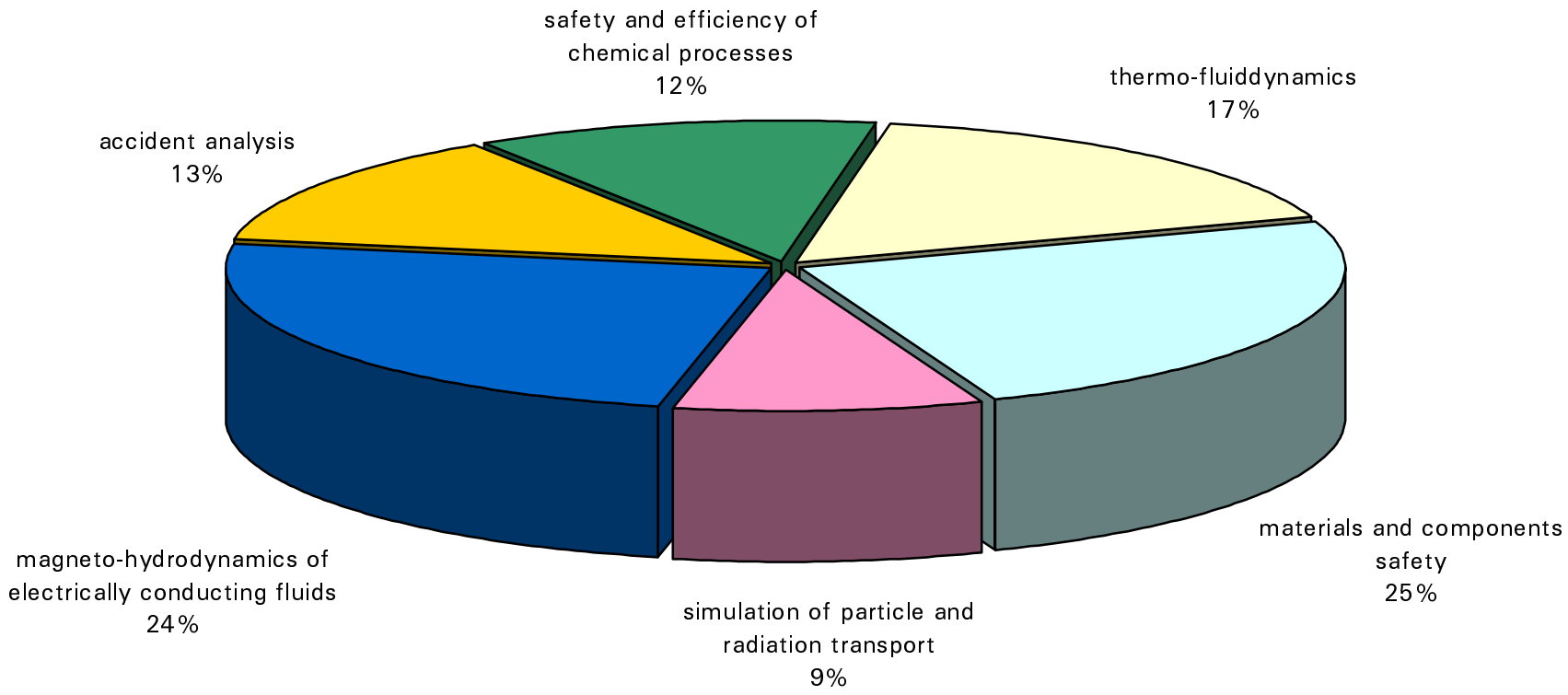

Selected Reports

CFD SIMULATIONS OF A BUBBLY FLOW IN A VERTICAL PIPE

Eckhard Krepper

1. Introduction

Even at the very simple conditions of two phase flow in a vertical pipe, strong 3D effects are observed. The distribution of the gas phase over the cross section varies significantly between the different flow patterns, which are known for the vertical two-phase flow. The air water flow in a vertical tube having a diameter of 50 mm and a length of about 3 m was investigated in steady state tests for different liquid and gas superficial velocities. Several two phase flow measuring techniques were used. Applying a wire mesh sensor, developed in FZR, the void fraction could be determined over the whole cross section of the pipe. The working principle is based on the measurement of the local instantaneous conductivity of the two-phase mixture (see H.-M. Prasser et. al [1] (1999), [2] (1998), [3] (1999)). At the investigated flow velocities, the rate of the image aquisition is sufficient to record the same bubble several times. This enables to determine bubble diameter distributions. Applying two similar wire mesh sensors with a distance of 50 mm one above the other, the influence of the wire mesh to the flow could be investigated. No essential disturbances of the two-phase flow by the mesh could be found for the investigated flow regimes. Performing an auto correlation between the signals of both sensors, also profiles of the gas velocity were determined.

In the CFD code CFX-4.2 several two-phase flow models were available. Using the code, volume fraction profiles were calculated and compared to the measured results for bubble flow regimes, to investigate the capability of these models (see also Krepper and Prasser [4] (1999)).

2. The experiments

Different tests at nominal temperature conditions and nominal pressure with different superficial velocities of liquid and air were performed. Figure 1 shows the Taitel/Dukler diagram with the investigated tests marked in different flow regimes. For each test stationary conditions were settled.

In the regime of bubble flow, a well known region exists for which a void maximum near the wall is observed (marked yellow in Figure 1). At a gas superficial velocity of 0.01 m/s and water velocities less than 0.2 m/s a void maximum in the centre of the tube

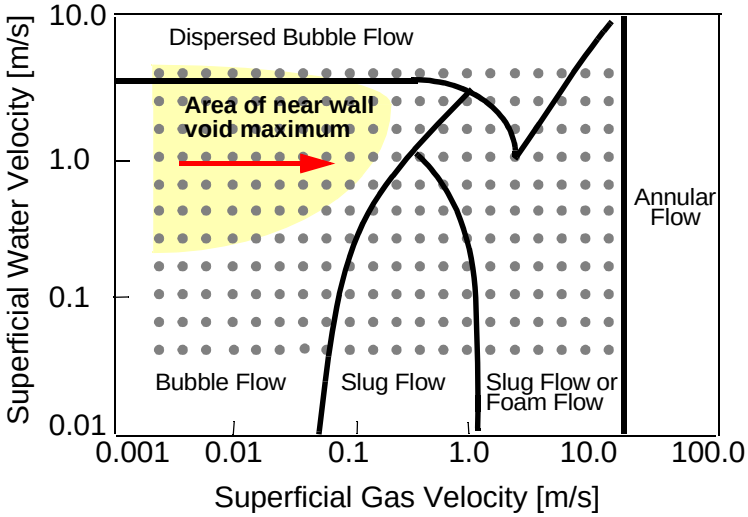

Fig. 1: Flow regime map (Taitel/Dukler)
The performed stationary tests are marked by points

was found. Both decreasing the water velocity or increasing the gas velocity shifts the void maximum to the centre of the tube.

3. CFX-4.2 calculations

The CFX-4.2 calculations aimed at the assessment of the capability of the code to describe two phase bubbly flow. For different tests of bubbly flow the void profiles in the tube cross section were analysed. The development of the void profile in the tube in dependency on the distance to the air injection and on the injection mode was investigated, too.

For the calculations, the two fluid model implemented in CFX-4.2 was applied. The liquid phase was represented as continuous and the gas as disperse phase with a constant bubble diameter of 4 mm.

Figure 2 shows the measured bubble size distributions of the investigated flow regimes at different distances from the gas injection (see Prasser [1] (1999)). The results show, that this regime with the given superficial liquid and gas velocities can be modelled using a monodisperse approach for the bubble size. For other flow regimes bubble size distributions were detected, which indicate coalescence (see example in [1] (1999)).

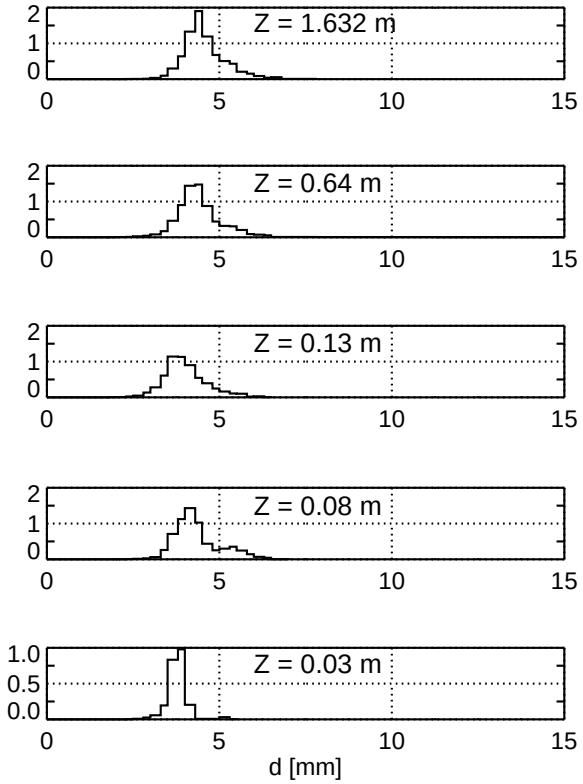

Fig. 2: Measured bubble size distribution at different distances above the gas injection
VL = 0.4 m/s; VG = 0.01 m/s

The drag force acting on the bubbles and the fluid were considered according to Ishii and Zuber [5] (1979). The particle induced turbulence was modelled according to Sato [6] (1975).

The establishment of the void profiles is mainly influenced by the “non drag forces”, which act perpendicular to the flow direction. A spherical obstacle in a profiled flow undergoes a lift force $F_{\alpha lift}$ perpendicular to the flow direction (see Zun [7] (1980)).

$$F_{\alpha\text{lift}} = r_\beta \cdot \rho_\alpha \cdot C_L \cdot \left(\overrightarrow{U_\beta} - \overrightarrow{U_\alpha}\right) \times \nabla \times \overrightarrow{U_\alpha}$$

The index α denotes the liquid and β the gaseous phase. r is the volume fraction, ρ the density and U the velocity. For a solid sphere, a coefficient for $C_L = 0.5$ is calculated. For weakly viscous flows the bubble shape deviates from the spherical form. Therefore $C_L = 0.05$ was used.

The turbulent dispersion force acts towards an even gas fraction distribution:

$$F_{\alpha diff} = C_{TD} \cdot \rho_{\alpha} \cdot k_{\alpha} \cdot \nabla r_{\beta}$$

k is the turbulent kinetic energy. The coefficient C_{TD} was set to C_{TD}= 0.1.

According to the profiles of velocity, k and ∇r_{β}, found for a flow in a tube, these two components of non drag forces are directed towards the wall. Therefore, considering only lift and dispersion force, the gas fraction near the wall is overestimated. Antal et. al [8] (1991) proposed, additionally to consider a lubrication force which drives the bubbles away from the wall. This force is the consequence of the no-slip condition for the continuous phase at the wall. The asymmetric fluid flow, to which a bubble of a diameter d is exposed to at a distance of y_w, causes the lubrication force:

$$F_{\alpha \mathrm{lub}} = \frac{r_{\beta} \cdot \rho_{\alpha} \left(\overrightarrow{U_{\beta}} - \overrightarrow{U_{\alpha}} \right)^2}{d} \cdot \max\left(C_1 + C_2 \cdot \frac{d}{y_w}, 0 \right) \vec{n}$$

$\vec{n}$ denotes the normal vector at the wall. The coefficients were fitted to the experimental results and were set to C_1 = -0.0064 and C_2 = 0.016.

The flow of both phases was modelled as turbulent. The calculations were performed in a three-dimensional cylindrical domain with a radius of R= 0.025 m and a length of Z = 3.0 m corresponding to the vertical test section. The whole grid with non equally divided cell dimensions consisted of 50,000 cells. For the liquid phase a no-slip and for the gas phase a free-slip boundary condition were chosen at the wall. The inlet boundary condition at the lower end of the cylinder corresponded to an equal gas flow distribution over the cross section at the inlet. The fluid velocity profile, the liquid turbulent energy k and the liquid turbulent dissipation rate ε were set to a fully developed single phase flow. A pressure boundary condition was assumed at the outlet on the top.

During the calculations the default difference schemes were used. The inter-phase slip algorithm was applied. The calculations were performed as transients with constant boundary condition. A constant time step corresponding to the Courant time step was applied. The mass balance between the inlet and the outlet was checked during the transient (see Figure 3).

$$BALANCE = \frac{\dot{M}_{IN} - \dot{M}_{OUT}}{\dot{M}_{IN}}$$

The figure shows, that even small discrepancies in the gas mass balance disappeared only after a transient time which corresponds to the time that a disturbance needs to pass the tube length of 3 m. Increasing the time step by a factor of 4 resulted in larger mass balance deviations during the tran-

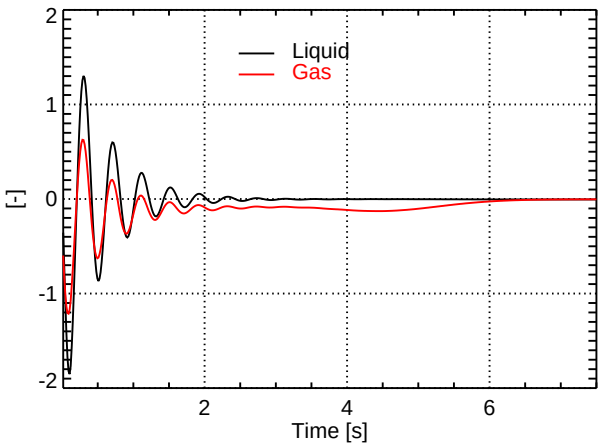

Fig. 3 : Relative liquid and gas mass balance between tube inlet and outlet
VL = 0.4 m/s; VG = 0.01 m/s

sient, but also converged to equalized balance after 7.5 seconds.

Figure 4 shows the calculated velocity profiles and the comparison to the experiment at about 3 m behind the air injection. A typical flow profile for the fluid is found. The gas velocity profile was experimentally determined by auto correlation of the signals of two wire mesh sensors arranged at a distance of about 50 mm.

Considering all three non drag forces, the calculated void profiles agree at least qualitatively with the measurements (see Figure 5). Injecting the gas from the bottom, the void fraction maximum immediately near the wall is established (see Figure 5 for Z = 0.1 m). With increasing distance from the air injection, the volume fraction maximum is shifted away from the wall (see Figure 5). These relations were observed in the tests, too.

Figure 6 shows the different contributions of the non drag forces. A positive value means the direction towards the wall. Corresponding to a liquid velocity profile found in a vertical tube, the lift force is directed towards the wall. Only near the wall the turbulent dispersion force which depends on the profiles for k and ∇r_β is directed towards the centre of the tube. The lubrication force acts away from the wall, but only immediately near the wall. Therefore the description of a flow regime with a volume fraction in the tube centre will not be possible considering only these three forces and assuming a monodisperse bubble size distribution.

Figure 7 shows the measured void fraction profiles for a test series with a liquid superficial velocity of 1.0 m/s. The gas superficial velocity for the different tests is increased from 0.01 to 0.125 m/s. The establishment of a second

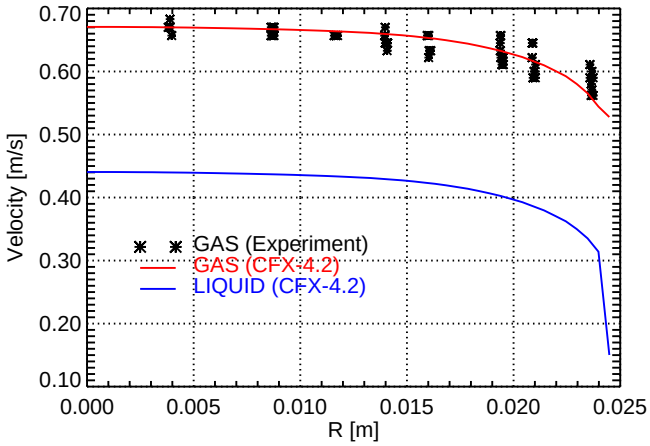

Fig. 4: Measured and calculated velocity profiles near the top of the tube
VL = 0.4 m/s; VG = 0.01 m/s

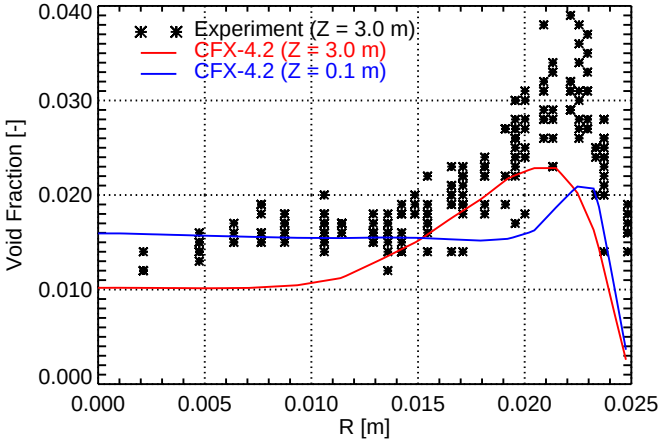

Fig. 5: Measured and calculated gas volume fraction profiles at different distances from the gas inlet
VL = 0.4 m/s; VG = 0.01 m/s

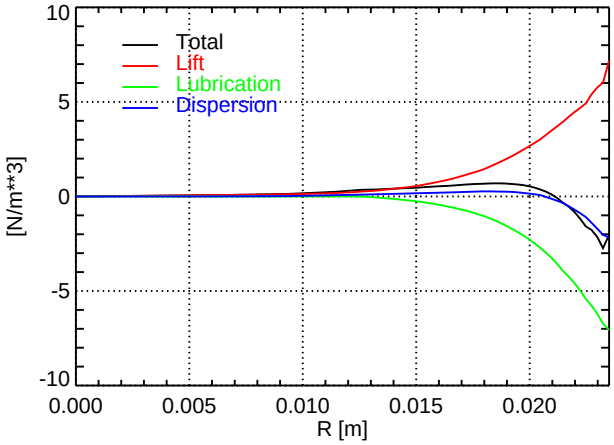

Fig. 6: Components of the considered non drag forces
VL = 0.4 m/s; VG = 0.01 m/s

void maximum in the tube centre is seen in the experiments. For larger gas velocities this second maximum is enlarged and dominates the whole profile. Figure 8 shows the calculated results. The figure shows, that with increasing gas velocity the near wall void maximum is overestimated, but the second maximum in the centre does not develop. The reason might be found in the occurrence of bubble coalescence and bubble diffraction, which is not considered in the models. For these flow regimes different bubble classes have to be considered. Larger bubbles having dimensions in the order of the tube diameter will be exposed to other forces than modelled here.

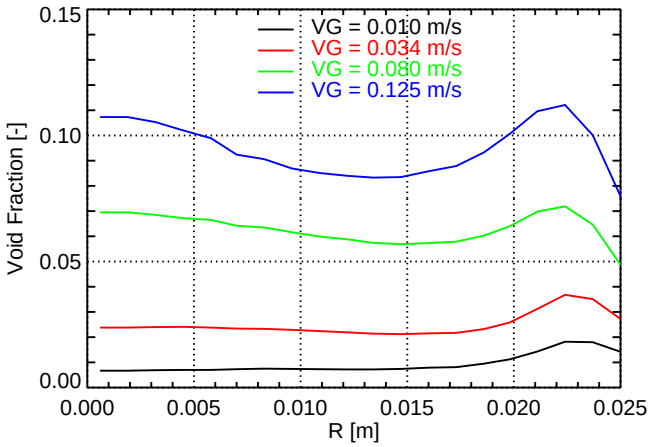

Fig. 7: Measured void fraction profiles for a liquid superficial velocity of VL = 1.0 m/s

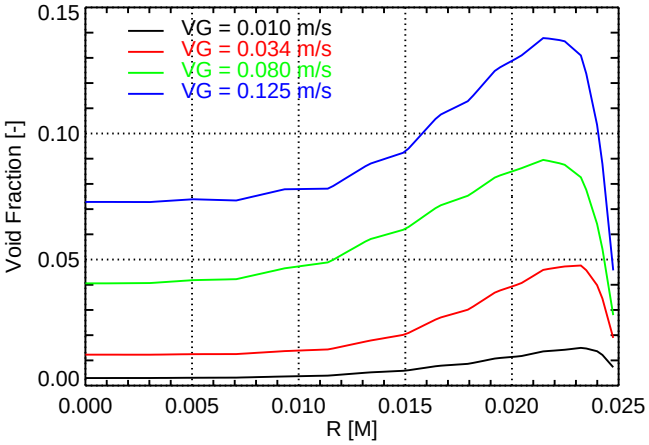

Fig. 8: Calculated void fraction profiles for a liquid superficial velocity of VL = 1.0 m/s

4. Summary and conclusions

For the calculation of void profiles in a vertical upward bubbly flow, the consideration of the non drag forces is essential. The two phase models implemented in the code version CFX-4.2 can describe void profiles with a near wall void maximum, when the model constants are well fitted to the tests. The investigated tests show the limits of the assumption of a single bubble diameter. Model extensions are necessary which consider the bubble diameter distribution due to bubble coalescence and bubble diffraction. The consideration of bubbles having a size in the order of the tube diameter requires the development of new bubble force models. The experiments at the measuring techniques test loops yield valuable information for the development and validation of such models.

References

[1] H.-M. Prasser (1999), Wire-mesh sensors for two-phase flow investigations, F.-P. Weiß, U. Rindelhardt (Ed.) Forschungszentrum Rossendorf, Institute of Safety Research, Annual Report 1998

[2] H.-M. Prasser, A. Böttger, J. Zschau (1998), A new electrode-mesh tomograph for gas-liquid flows; Flow Measurement and Instrumentation 9, pp. 111-129

[3] E. Krepper, A. Krüssenberg, H.-M. Prasser, A. Schaffrath (1999), High Resolution Void Fraction Measurements for the Validation of Flow Maps and CFD Codes, 2nd International Symposium on Two-Phase Flow Modelling and Experimentation, Pisa 1999, Proceedings Vol. III, pp. 1371-1378

[4] E. Krepper, H.-M. Prasser (1999), Measurements and CFX-Simulations of a Bubbly Flow in a Vertical Pipe, CFX International Users Conference, Friedrichshafen, Juni 1999

[5] M. Ishii, N. Zuber (1979), Drag coefficient and relative velocity in bubbly, droplet or particulate flows; AIChE Journal Vol. 25(1979)5, 843-855

[6] Y. Sato, Sekoguchi, K. (1975), Liquid velocity distribution in two phase bubble flow; Int. J. Multiphase Flow 2(1975), p. 79

[7] I. Zun (1980), The transverse migration of bubbles influenced by walls in vertical bubbly flow; Int. J. Multiphase Flow 6, pp. 583-588

[8] Antal, S.P., Lahey Jr., R.T., Flaherty, J.E. (1991), Analysis of phase distribution in fully developed laminar bubbly two phase flow; Int. J. Multiphase Flow 17(1991)5,635-652

NUMERICAL INVESTIGATION OF THE COOLANT MIXING DURING FAST DEBORATION TRANSIENTS FOR VVER-440 TYPE REACTORS

Thomas Höhne and Ulrich Rohde

1. Introduction

Complex computer codes modeling the whole reactor system including 3D neutron kinetics in combination with advanced thermohydraulics plant models become more and more important for the safety assessment of nuclear reactors. Such codes only are capable of estimating the feedback effects in a realistic way, for instance reactivity initiated accidents with strongly asymmetric neutron flux distribution in the core caused by a perturbation in one of the coolant loops.

At Forschungszentrum Rossendorf (FZR), Institute of Safety Research, both the hexagonal and the cartesian versions of the 3-dimensional neutron kinetics code DYN3D were coupled with the advanced thermohydraulics system code ATHLET [2]. The 3-dimensional reactor core model DYN3D [3] has been developed for the simulation of reactivity initiated accidents, where space-dependent effects in the reactor core are relevant. These are, e. g. steam line breaks or boron dilution transients. Since a 1D thermohydraulics code and a 3D reactor core model are coupled, there is a need for an interface between the different spatial resolutions. This interface simulates 3D mixing in the RPV by relating the 2D concentration and temperature fields at the core inlet to the 1D concentration and temperature profiles in the single loops.

In the past, an analytical model for the description of coolant mixing in the RPV of VVER-440 reactors based on the analytical solution of the Navier-Stokes equations in the potential flow approximation has been developed to replace the non-conservative approach of homogeneous mixing inside the RPV. This model is included in the coupled code DYN3D/ATHLET [3]. Another way to calculate the 3D flow distribution in the downcomer and the lower plenum is the use of the results of computational fluid dynamics (CFD) codes. At present, the direct coupling of CFD and thermohydraulics system codes is impossible due to the high demands on computation time in the CFD-calculations. Therefore, simplified mixing models validated by CFD calculations are still required for coupled codes.

The VVER-440 (440 MW) V-230 was considered for analyzing the flow field and mixing processes. The V-230 has no elliptical sieve plate in the lower plenum. Previously, the 3D flow distribution in the downcomer and the lower plenum of the VVER-440 reactor have been calculated by means of the CFD code CFX-4 [4] for operational conditions [1]. The CFX-calculations were compared with the experimental data and the analytical mixing model.

In this paper, CFD calculations for the start-up of the first main coolant pump in a VVER-440 type reactor are reported about. This scenario is important in case that there is a plug of lower borated water in one of the primary coolant loops.

2. Calculation of mixing processes with a CFD code

2.1 Model assumptions, geometry preparation and grid generation

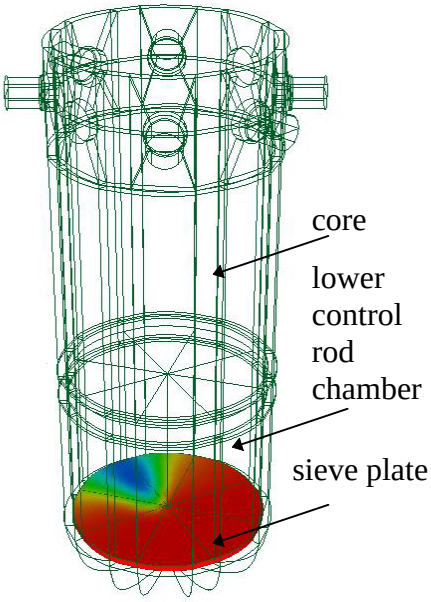

Fig. 1: CFD block structure (VVER-440)

For the coolant flow simulation in the downcomer and lower plenum of a VVER-440 type reactor an incompressible fluid was assumed. The turbulence was modeled using the standard k-ε approximation. The calculations were done on a SGI Origin 200 (1 GB RAM, 4x R 10000 180 MHz, 64 Bit CPU) workstation platform. For the calculations, a geometrical model of the VVER-440 RPV has been developed (see Fig. 1). The parameters of the corresponding computational grid are given in Table 1. In order to receive an optimal net griding for the later flow simulation one must consider the following items: Checking grid number in special regions to minimize numerical diffusion, refinement of the griding in fields with strong changes of the dependent variables, adaptation of the griding to estimated flow lines, generation of nets as orthogonal as possible (angle >20°).

Table 1: Discretization of the VVER-440 type reactor

PWR	No. of blocks	No. of patches	No. of grid cells
VVER-440	236	912	159800

Inlet boundary conditions were set at the inlet nozzles as given velocity and temperature. The outlet boundary conditions were set to pressure controlled at the core inlet. The core was not modelled. The control rod chamber below the core is separated from the lower plenum by a sieve plate. The sieve plate is modeled as a porous region. The porosity value γ for perforated plates is determined by relating the area of orifices to the total area of the sieve plate . Body forces B are added to the momentum equation (1), to take into account distributed friction losses in the sieve plate. Using the Cartesian coordinate system, the momentum equation is written:

(j=1,2,3)
$$\rho\left(\frac{\partial U_j}{\partial t} + U_i \frac{\partial U_j}{\partial x_i}\right) = B_j - \frac{\partial}{\partial x_i}\tau_{ij} \qquad (1)$$

$$B = B_F - \left(R_C + R_F|\bar{u}|\right)\bar{u} \qquad (2)$$

In the equation (1) U_j are the components of velocity and τ is the shear stress, in equation (2) B_F, R_C and R_F are the coefficients of the body force dependence on the velocity. In the

model, only the second order contribution of the body forces according to relation (2) is used being typical for turbulent flow. The corresponding coefficient is obtained from measured values for the flow resistance at the perforated plate of the VVER-440.

2.2 Assumptions for modeling of a transient boron dilution scenario for VVER-440 type reactors

The boron dilution at the primary circuit of a PWR has become one of the most important issues in PWR safety. Inhomogeneous boron dilution events may occur in the PWR's, if partially diluted or completely unborated slugs form in the primary system under stagnated loop flow conditions. The slugs could be transported into the core after restart of a reactor coolant pump or re-establishment of natural circulation in the loop. Coolant mixing provides an inherent safety mechanism, which is the most important mitigative feature against diluted slugs.

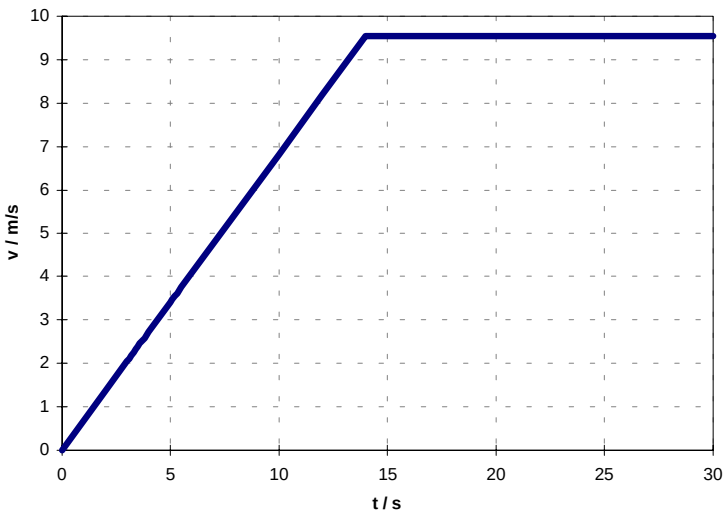

Fig. 2: Velocity at the inlet nozzle of the starting pump

Model experiments for studying mixing of diluted slugs have been performed in Sweden [7], France [8], Russia etc. and at the Mixing Test Facility ROCOM at FZR Rossendorf / Germany. Many of the studies are concentrated on the scenario 'Start-up of the first pump'. In this scenario the diluted slug is transported from the loop to the core by starting a main coolant pump (MCP). The flow in the starting loop accelerates rapidly. Besides the flow through the core, the experiments show a back flow through the open non operating loops.

The following additional boundary conditions were assumed for the transient numerical simulation of a pump start-up scenario:

- initially all pumps are stopped, no natural circulation occurs
- in one loop the MCP starts linearly from 0 to 8550 kg/s in 14 s, after 14 s the mass flow rate is constant at 8550 kg/s (Fig.2)
- the unborated slug is given as a scalar pulse from 3.0-5.0 s after the beginning of the start-up of the MCP (Fig. 3), the unborated slug corresponds to 7.3 m^3 of unborated water (assumed volume of unborated water caused by external dilution)
- no counter flow through the other loops was considered as a conservative assumption, the slug is completely passing the core

The scalar representing the boron content of the slug is treated in normalized form by setting the original boron concentration deficit of the slug equal to unity. In [9] a sensitivity study on the turbulence models, the difference schemes and the choice of time discretization was made

to show the influence of these patterns on the result of the calculation. An important fact was the right choice of time discretization (0.05 s) to minimize numerical diffusion.

2.3 Results of pump start-up simulation

The results of a pump start-up simulation are shown in Fig. 5. The results show a very complex flow in the downcomer. The injection is distributed into two main jets, the so called butterfly distribution. In addition, several secondary flows are seen in various parts of the downcomer. Especially strong vortices occur in the area below the injection loop. Here a strong recirculation area occurs. The complex flow field promotes strong mixing of the slug in the downcomer.

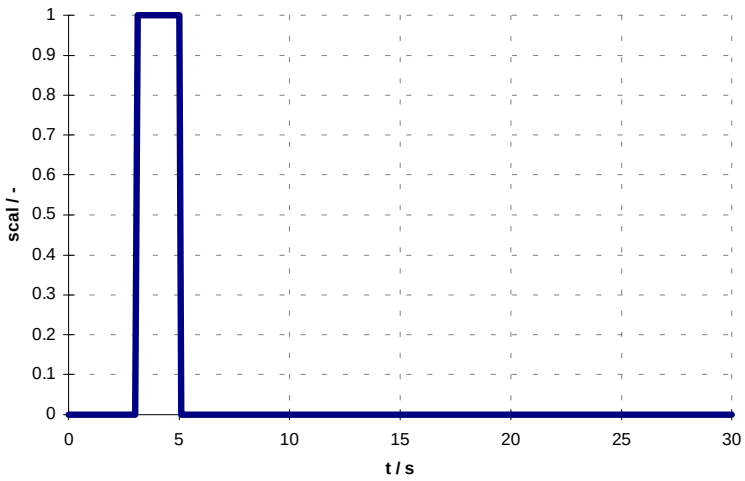

Fig. 3: Scaled concentration level at the inlet nozzle of the starting pump

Although the slug divides into several parts two main fronts propagate towards the core on the left and right side of the injection loop. Parts of this main front are less mixed. The front of the mixed slug reaches first the sieve plate and then a few seconds later the core inlet.

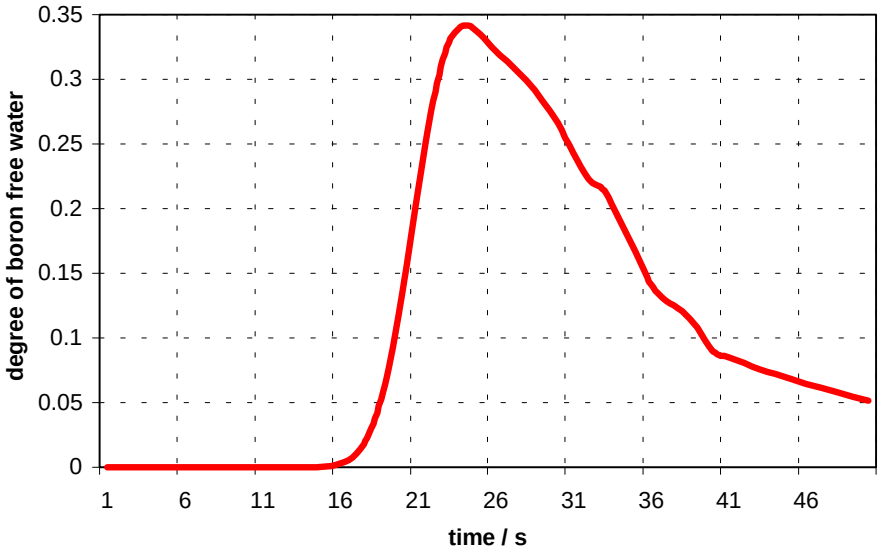

Fig. 4: Time dependent maxima of the lower borated plug at the core inlet

The control rod chamber is also playing an important role for mixing the slug front. Fig. 4 shows the time dependence of the maximum boron deficit (1 corresponds to the boron deficit in the loop) which is found at the core inlet plane. Because of the large coolant volumes of the downcomer and lower plenum compared to the loops (ratio 3:1), the maximum of the disturbance arrives only about 24 s after the beginning of the start-up of the pump. Due to the long flow path and the relative small volume of the unborated plug, only 34.1% decrease of boron concentration compared to 100% at the inlet nozzle was obtained. The results show

that the high downcomer of the VVER-440 and the lower control rod chamber support coolant mixing. For the investigation of possible recriticality of the scramed reactor after the insertion of a plug of lower borated water into the core, reactor dynamics calculations have to be performed, where the obtained CFD results can be used to provide the time dependent boron concentration at the core inlet.

Time / s	Downcomer	Core Inlet	Sieve Plate
		> 3.5000E-01 2.9615E-01 2.3558E-01 1.7500E-01 1.1442E-01 5.3846E-02 < 0.0000E+00 scal	> 3.5000E-01 2.9615E-01 2.3558E-01 1.7500E-01 1.1442E-01 5.3846E-02 < 0.0000E+00 scal
7.0	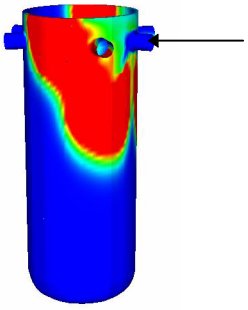	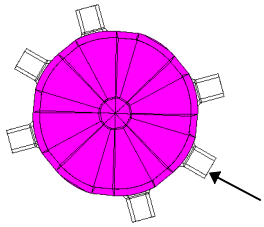	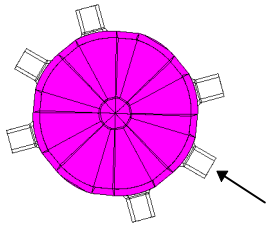
12.0	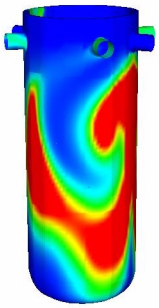	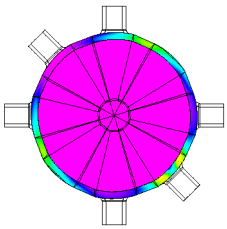	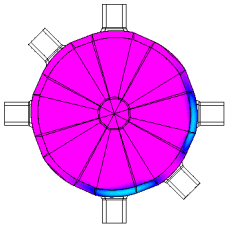
16.0	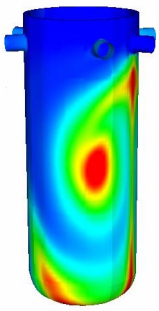	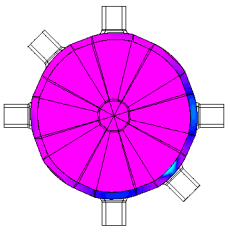	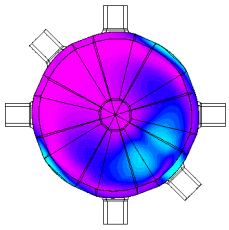
23.0	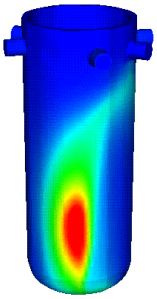	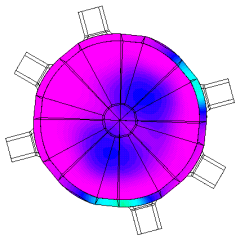	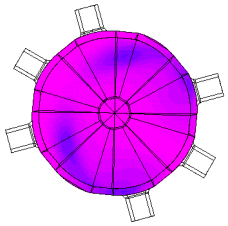

Fig. 5: Time dependent mixing conditions at the pump start-up scenario

3. Outlook

Further investigations are necessary to model the internals with more details. To validate the CFX-4 calculations it is necessary to compare the results with experiments for VVER-440 reactor types. To analyze the dependencies of the power output of the reactor on the temperature and/or boron concentration distribution an interface between CFD models and the neutron kinetic code DYN3D has to be set up at the core inlet region.

References

[1] Kliem, S., Höhne, T., Weiß, F.-P. (1999), Main steam line break analysis of a VVER-440 reactor using the coupled thermohydraulics system/3D-neutron kinetics code DYN3D/ATHLET in combination with the CFD code CFX-4, 9th International Topical Meeting on Nuclear Reactor Thermal Hydraulics (NURETH-9), San Fransisco, California, Oct. 3-8

[2] Burwell, M.J., Lerchl, G., Miro, J., Teschendorff, V., Wolfert, K. (1989), The Thermalhydraulic Code ATHLET for Analysis of PWR and BWR Systems, NURETH-4, Proceedings Fourth International Topical Meeting on Nuclear Reactor Thermal-Hydraulics, Vol. 2, Karlsruhe, 1234

[3] U. Grundmann, S. Kliem, U. Rohde (1997), The coupled code complex DYN3D/ATHLET-application to main steam line break analysis, Proc. M&C and SNA '97, Saratoga Springs, New York, USA, October 6-9

[4] CFX-4.2 User Manual (1997), AEA Technology

[5] P. Dräger (1987), Makroskopische Kühlmittelvermischung in Druckwasserreaktoren, Dissertation TH Zittau

[6] Höhne,T., Grunwald, G., Rohde, U. (1998), Coolant Mixing in Pressurized Water Reactors", FZR-Bericht, FZR-237

[7] F. Alavyoon, B. Hemström, N.G. Andersson, and R.I. Karlsson (1995), Experimental and Computational Approach to Investigating Rapid Boron Dilution Transients in PWRs, CSNI Specialist Meeting on Boron Dilution Reactivity Transients, State College, PA, U.S.A., 18th-20th October

[8] D. Alvares, F.Cases, A. Martin, and S. Stelleta (1995), Boron mixing transients in a PWR vessel - Physical studies. CSNI Specialist Meeting on Boron Dilution Reactivity Transients, State College, PA, U.S.A., 18th-20th October

[9] Höhne, T. (1999), Sensitivitätsanalysen von numerischen Strömungsberechnungen bei Kühlmittelvermischungstransienten in einem vereinfachten Downcomermodell eines Druckwasserreaktors mit CFX-4.2, interner Bericht

WIRE-MESH SENSOR - NOW 10,000 FRAMES PER SECOND

Horst-Michael Prasser, J. Zschau
Dieter Peters[1], Gerd Pietzsch[1], Wolfgang Taubert[1], Manuel Trepte[1]

1. Introduction

In the annual report 1996 a new wire-mesh sensor for gas-liquid flows was presented [1]. In the last two years the sensor was applied to an air-water flow in a vertical pipeline (inner diameter D=51.2mm) to study the flow structure in a wide range of superficial velocities. Besides the void fraction distributions, the high resolution of the sensor was used to calculate bubble size distributions from the primary measuring data. This allowed to study the evolution of the flow structure along the pipe [2]. The maximum time resolution available to perform these experiments was 1,200 measurements per second. Now we can report about the increase of the measuring frequency to 10,000 frames per second. In the result it is possible to visualise and quantify individual bubbles or droplets at a much higher flow velocity, than before.

2. Working principle of the wire-mesh sensor

The function is based on the measurement of the local instantaneous conductivity of the two-phase mixture. The sensor consists of two electrode grids with 16 electrodes each, placed at a small axial distance behind each other (Fig. 1). The conductivity is measured at the crossing points of the wires of the two grids. One plane of electrode wires is used as transmitter, the other as receiver plane. During the measuring cycle, the transmitter electrodes are activated by a multiplex circuit in a successive order, as illustrated in Fig. 2 for an example of 2 x 4 wires.

The measurement for one row is started by closing one of the switches S1-S4. The currents arriving at the receiver wires are transformed into voltages by operational amplifiers and sampled by individual sample/hold circuits. After an analogue/digital conversion the signals are transferred to a data acquisition computer and stored for each receiver electrode separately. This procedure is repeated for all transmitter electrodes [3].

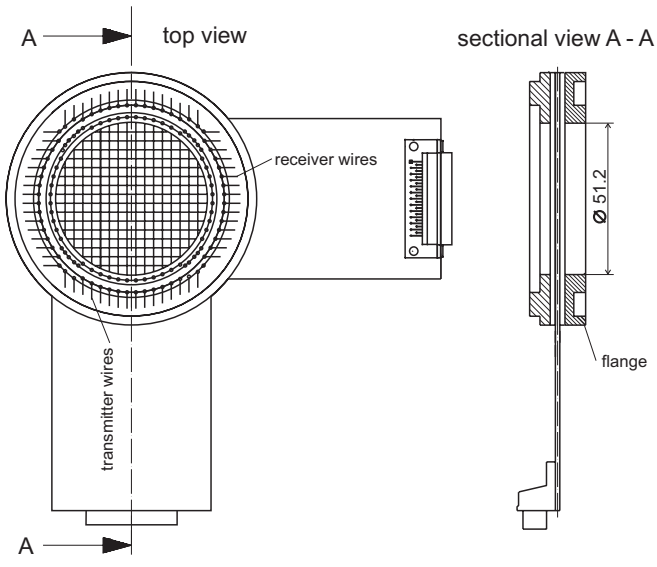

Fig. 1: Wire-mesh sensor (2 x 16 electrode wires)

After the first laboratory prototype was successfully built, the wire-mesh sensor including the signal acquisition unit was qualified for

[1] TELETRONIC Ingenieurbüro, GbR, Bautzner Landstraße 45, 01454 Großerkmannsdorf

series production in co-operation with the TELETRONIC Ingenieurbüro GbR. It is now commercialised by this company. The signal acquisition unit of this device contains the elements shown in Fig. 2. The timing of the transmitter activation, the sample/hold triggering and the AD conversion is controlled by a Freely Programmable Gate Array (FPGA). The unit must be linked to a data acquisition computer (PC) to be operated. A parallel interface (16 bit) is used to transfer the AD conversion results to the personal computer. This interface is coupled to the ISA-bus of the PC. This is the main factor limiting the measuring frequency of the system to 1.200 frames per second.

When we look at this time resolution from the point of view of flow visualisation, we find for example that bubbles of several millimetres magnitude are mapped in several successive instantaneous gas fraction distributions (frames), if the flow velocity is not too large. At 1 m/s the bubble travels about 1 mm in 1 ms, i.e. a bubble of 5 mm diameter is displayed in approximately 5 - 6 successive frames. When the flow velocity is increased, the situation soon becomes worse. In the interesting region of transition from slug flow to annular flow, which takes place at velocities of about 10 m/s, bubbles or droplets of the mentioned size can even cross the measuring plane without being visualised. For this reason efforts were made to increase the measuring frequency to 10,000 frames per second. In December 1999 the first prototype of the new generation of signal acquisition units was successfully tested at the two-phase flow loop of the institute.

The analogue part of the first generation of signal acquisition units was already designed for a higher measuring frequency. A sufficient improvement of the signal quality was achieved by placing the preamplifiers of the receiver electrodes as well as the driver circuits for the transmitters into the casing of the connectors at the end of the cables to the sensor.

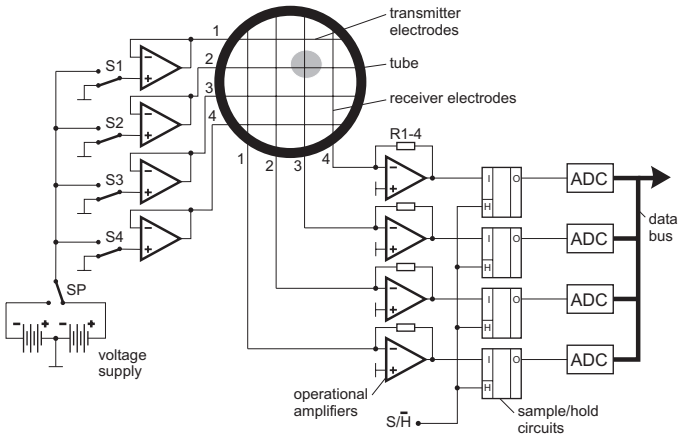

Fig. 2: Simplified scheme of a 2 x 4 wire-mesh sensor with signal acquisition system

The main optimisations had to concern the digital part, i.e. the AD conversion, the data storage and the data transfer to a data evaluation computer. The main feature of the second generation unit is an integrated digital signal processor (Analog Devices Sharc DSP 21065L) managing a data storage of 64 MB external SDRAM. The activation of the transmitter electrodes and the work of 16 AD converters is again controlled by an FPGA (Freely Programmable Gate Array). The pulse width for the transmitter electrode activation is 3 µs. Within this time, the transient of the receiver amplifiers is settled. The ADCs, one for each receiver electrode, have a conversion time of 2.3 µs. For noise reduction, every measurement is carried out twice - once for the positive half-period of the transmitter pulse and a second time for the negative half-period. Afterwards, the conversion results are subtracted from each other by the FPGA, the DSP takes over the data into the RAM. The AD conversion for both half periods is carried out during the build-up time of the signal of the other half period. In this way, a total measuring period for one transmitter wire of 6 µs and the corresponding measuring frequency of 10,000 frames per second were achieved.

The transfer of the measured data to the data acquisition PC is performed only after the completion of the measuring series. For this purpose, the DSP is equipped with an ETHERNET interface. The memory size is sufficient to store 170,000 individual measuring results for all 16 x 16 crossing points of the sensor, i.e. a continuous measurement over 17 s is possible.

3. Flow pattern visualisation

The output of the wire-mesh sensor consists of a time sequence of local instantaneous void fractions that characterise the presence of the gaseous phase in a grid of measuring positions in the cross section. These data sets can be used for a visualisation of the two-phase flow. With the help of a special software the individual gas fraction distributions can be displayed as a sequence of frames. Eulerian sectional views of the gas fraction distribution in the vertical center plane of the pipe can be obtained, if successive void fraction distributions over the diameter are plotted in a vertical stack, beginning from the top and moving downwards. The resulting graphs give the impression of a side view of the flow. In Fig. 3, the increase in resolution gained by the new signal acquisition unit is illustrated for a slug flow. At the right side the flow pattern is shown in the high resolution of 10,000 frames per second. At the left, the same data is shown with a time axis compressed by a factor of 8. In this way, a comparison to the resolution of the first generation of signal acquisition units for one and the same experiment run is possible. It is clearly visible, that the bubble cloud in the wake of the slug is resolved in much more detail.

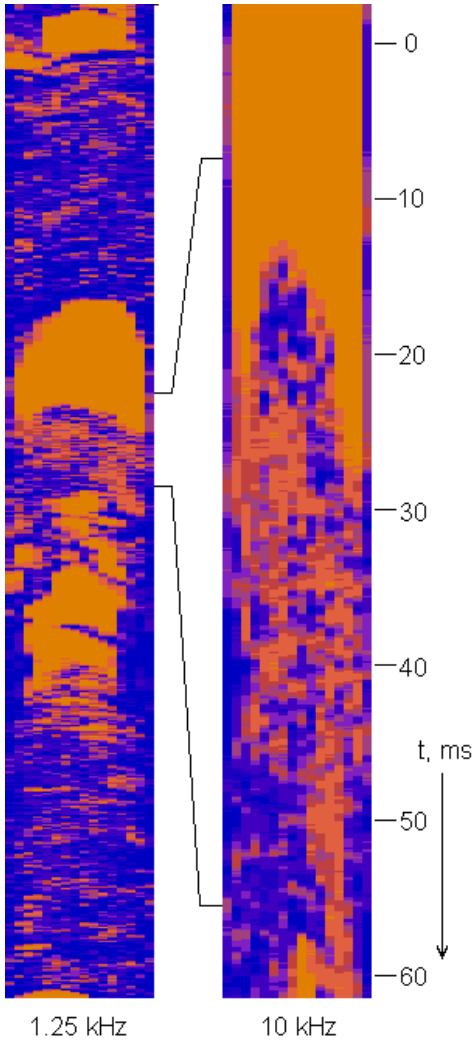

Fig. 3: Resolution increase gained by the new signal acquisition unit

The comparison of signals, obtained at different experiment runs with both the old and the new device is shown in Fig. 4. Here, different realisations of the flow pattern at identical superficial gas and water velocities are presented. The examples are taken from the region of higher flow velocities. The signal recorded at the higher measuring speed offers much more details. Furthermore, it is very important for the bubbles size measurement, that individual bubbles are visualised in several successive frames at the high measuring speed, while they are found only in one single frame at the low speed (one line in the sectional plots).

4. Conclusion

The new generation of signal acquisition units is able to deliver a flow visualisation with a resolution of 10,000 frames per second. This gains much more details of the flow structure, than before. The achieved measuring frequency extends the applicability of the wire-mesh

sensors towards the two-phase flow at velocities in the range of 10 m/s. In the next step, it is planned to increase the number of electrodes in order to make it possible to increase the sensor diameter without losing spatial resolution.

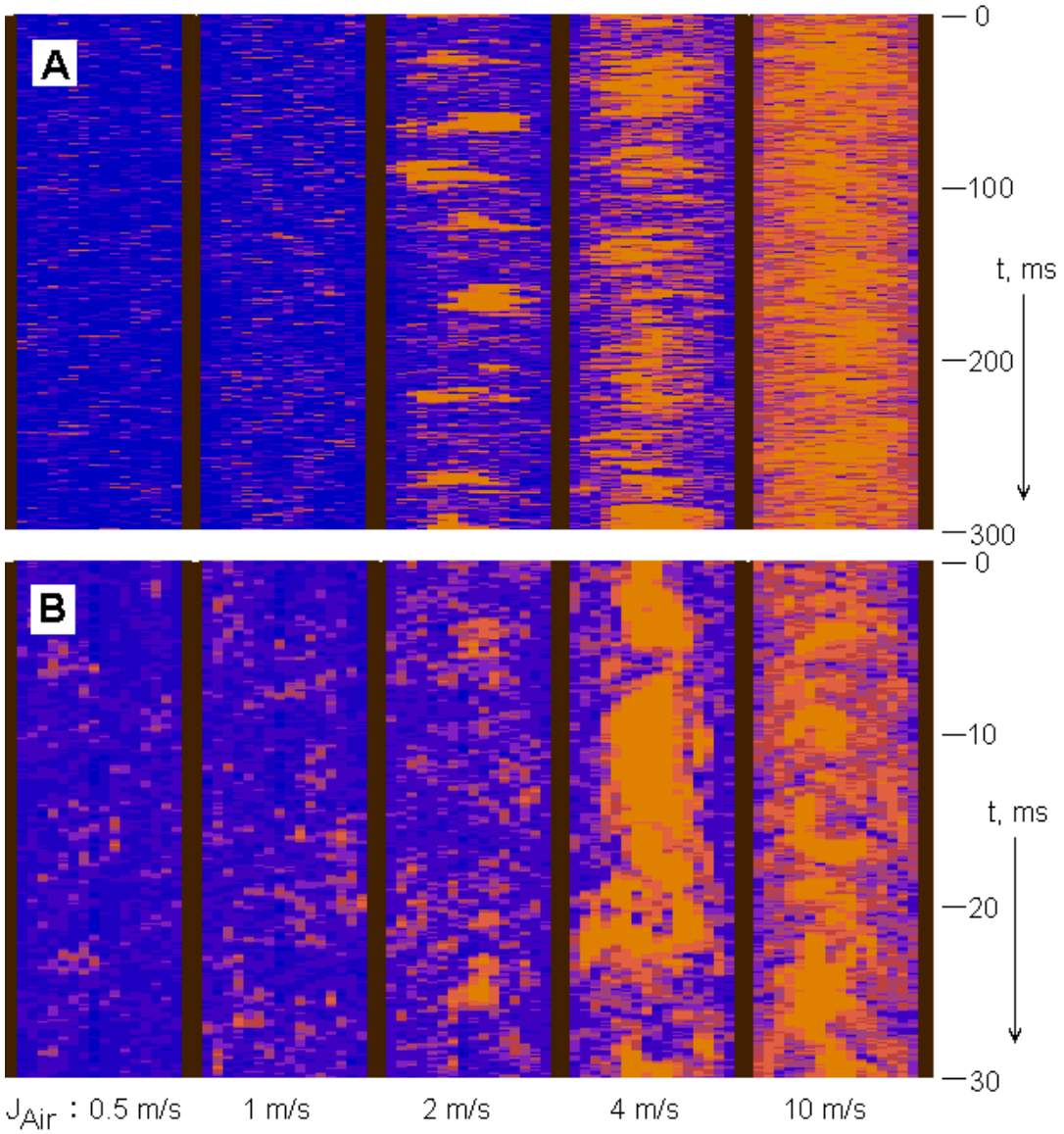

Fig. 4: Two-phase flow structure at J_{Water}=4 m/s and high air flow, A: first generation of signal acquisition units (1,200 Hz), B: second generation (10,000 Hz)

References

[1] H.-M. Prasser, A. Böttger, J. Zschau (1997), A New wire-mesh tomograph for gas-liquid flows, in F.-P. Weiß, U. Rindelhardt (Ed.), Annual Report 1996, Institute for Safety Research, FZR-190, 34-37

[2] H.-M. Prasser, Wire-Mesh Sensors for Two-Phase Flow Investigations, F.-P. Weiß, U. Rindelhardt (Ed.), Annual Report 1998, Institute for Safety Research, FZR-268, 23-28

[3] H.-M. Prasser, A. Böttger, J. Zschau (1998), A new electrode-mesh tomograph for gas-liquid flows, Flow Measurement and Instrumentation 9, 111-119

ATHLET CALCULATIONS OF THE PRESSURIZER SURGE LINE BREAK (PH-SLB TEST) AT THE PMK-2 TEST FACILITY

Eckhard Krepper and Frank Schäfer

1. Introduction

At the Hungarian integral test facility PMK-2 a pressurizer surge line break experiment (PH-SLB test) was carried out within the PHARE 4.2.6b project, [1]. The primary objective of the test was to provide experimental data for a surge line break transient at VVER-440 reactors with reduced injection from the emergency core cooling systems (ECC). At the Institute of Safety Research calculations of the experiment were performed with the thermohydraulic computer code ATHLET, which was developed by GRS (Gesellschaft für Anlagen- und Reaktorsicherheit) mbH. In the context of the PHARE 4.2.6b project the Institute of Safety Research has also supplied the void fraction measurement system for the PMK-2 test facility and was involved in the evaluation of the experimental results.

2. The PMK-2 test facility

The PMK-2 test facility (Fig. 1) is a full pressure, volume-scaled model of the Paks Nuclear Power Plant. The facility was constructed by the KFKI Atomic Energy Research Institute Budapest, [2] and is mainly designed to investigate small and medium size breaks in the primary system and to study the natural circulation behaviour of VVER-440 type reactors. The 6 loops of the plant are modeled by a single loop with a scaling ratio of 1:2070. The core model consists of an electrically heated 19-rod bundle.

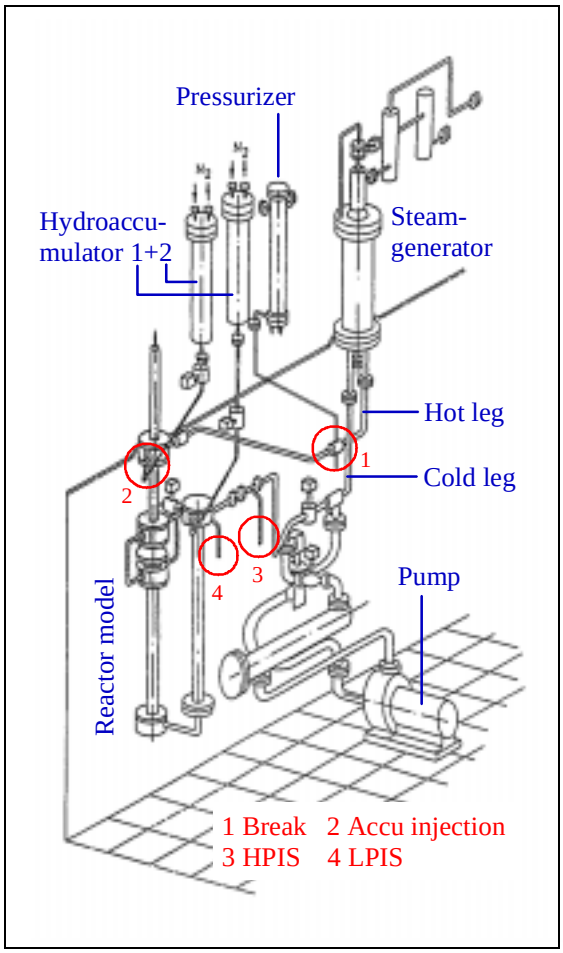

Fig. 1: The PMK-2 test facility

3. Description of the experiment

The experiment PH-SLB simulates a break of the pressurizer surge line with the assumption that only one of two hydroaccumulators and one of three high pressure injection systems (HPIS) work. The low pressure injection system (LPIS) is available. The break is located at the connection between surge line and hot leg (see Fig. 1). The available hydroaccumulator injects into the upper plenum of the reactor model. The HPIS and LPIS inject into the cold leg and the downcomer. The experiment starts with nominal conditions (full power, nominal mass flow). The

break of the pressurizer surge line leads to a fast pressure decrease in the primary system within approximately 30 seconds after the transient initiation. The injection from the hydroaccumulator and HPIS cannot compensate the loss of coolant in the primary side. Therefore, the reactor is fully emptied during the transient and a fast increase of the fuel cladding temperatures takes place. Because of the counter current flow in the reactor model, the water from the hydroaccumulator cannot reach the reactor core. Only with the injection from the LPIS the dry-out of the reactor core is stopped. The general course of events is presented in Table 1.

Table 1: Comparison of measured and calculated sequence of events

Event	Experiment	Calculation
Break initiation	0 s	0 s
Scram initiation	0 s	0 s
Start of pump coast down	0 s	0 s
Start of HPIS	17 s	17 s
Initiation of hydroaccumulator injection	20 s	18 s
Reactor coolant level at hot leg elevation	28 s	38 s
Primary pressure equals secondary pressure	31 s	30 s
Hot leg loop seal first clearing	70 s	70 s
Pump coast down ended	148 s	150 s
Start of core dry-out	210 s	236 s
End of hydroaccumulator injection	218 s	217 s
Hot leg loop seal final clearing	220 s	230 s
Reactor coolant level minimum	255 s	260 s
Start of LPIS	304 s	293 s
Maximum cladding temperature	444 s	398 s
Reactor coolant level is stabilizing	750 s	850 s
End of experiment	1000 s	1150 s

4. Thermohydraulic model

The presented results were obtained with the code version ATHLET Mod 1.1 Cycle C. The complete PMK-2 model consists of 169 control volumes and 128 heat conduction elements. For modeling the thermofluid objects in general the five-equation model of ATHLET was used and the one-dimensional steady state critical discharge model (CDR1D) was applied to calculate the break flow. Before starting the transient, a zero transient calculation at stationary boundary conditions was performed over a problem time of 1000 s. By means of the zero transient calculation the stationary mass flow in the primary loop, the pressure differences and the heat losses were adjusted. The secondary pressure was controlled by the steam outlet. The initiation of power scram, pump coast down and the start of the emergency cooling systems were controlled by time and pressure dependent signals. The power scram and pump coast down were started at t=0.1 s,

the HPIS was started at t=17 s, the hydroaccumulator injection was initiated at a primary pressure of PR21=5.94 MPa and the LPIS was started at PR21=0.85 MPa. The time dependence of the reactor power followed the characteristic decay heat curve.

5. Results

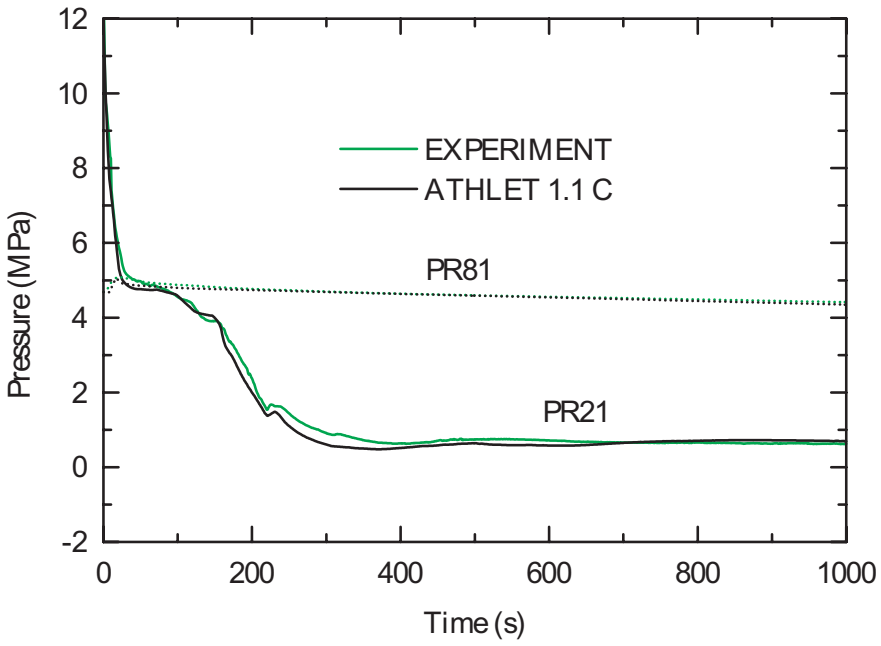

Fig. 2: Primary pressure (PR21) and secondary pressure (PR81)

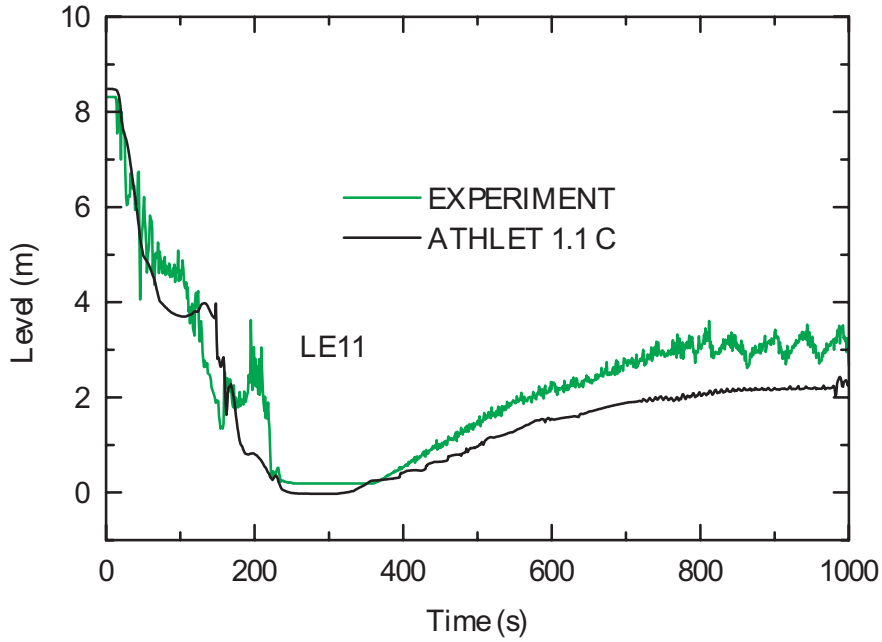

Fig. 3: Level in the reactor model (LE11)

An overview about measured and calculated events during the whole transient is given in Table 1. The transient was started by opening the break valve at t=0 s. Caused by the rapid primary pressure decrease the reactor scram and the pump coast down were initiated already at approximately t=0 s. At t=8 s the steam generator secondary side was isolated by closing the steam line and the feed water supply. The high pressure injection system was started triggered by the primary pressure signal at t=17 s. The most important event in this early phase of the transient is the fast depressurization of the primary system, see Fig. 2. Due to the break the pressurizer surge line is practically disconnected from the primary loop and the pressurizer is emptied at t=12 s. The reactor coolant level (LE11, Fig. 3) decreases very fast, reaching the hot leg elevation at t=38 s. Already at t=12 s a first flashing can be observed in the hot leg and at t=100 s the void fraction reaches a maximum. In this phase a transition to higher void fraction in the break flow (FL01, Fig. 4) can be observed and the reactor coolant level (LE11,

Fig. 3) stagnates. The setpoint of the hydroaccumulator injection was reached at t=20 s (LE92, Fig. 5) and the vaporization in the hot leg was temporary interrupted by the cold water flow towards the hot leg. At approximately t=30 s the primary pressure (PR21) equals the secondary pressure (PR81), see Fig. 2. A first hot leg loop seal clearing can be observed at t=70 s, indicated by the hot leg loop seal level (LE31, Fig 6). Up to this point the ATHLET calculation shows a very good agreement with the measured results.

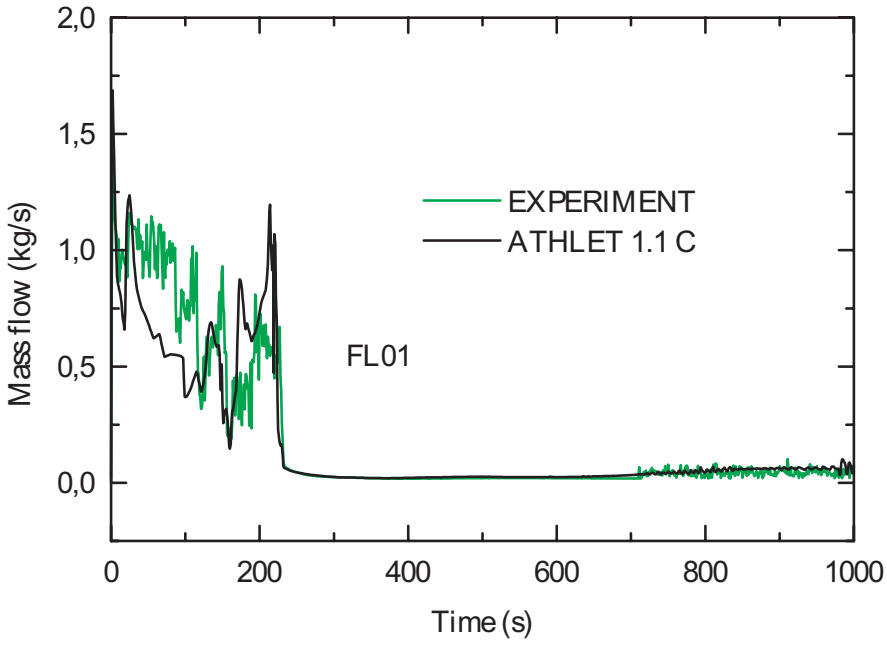

Fig. 4: Break mass flow (FL01)

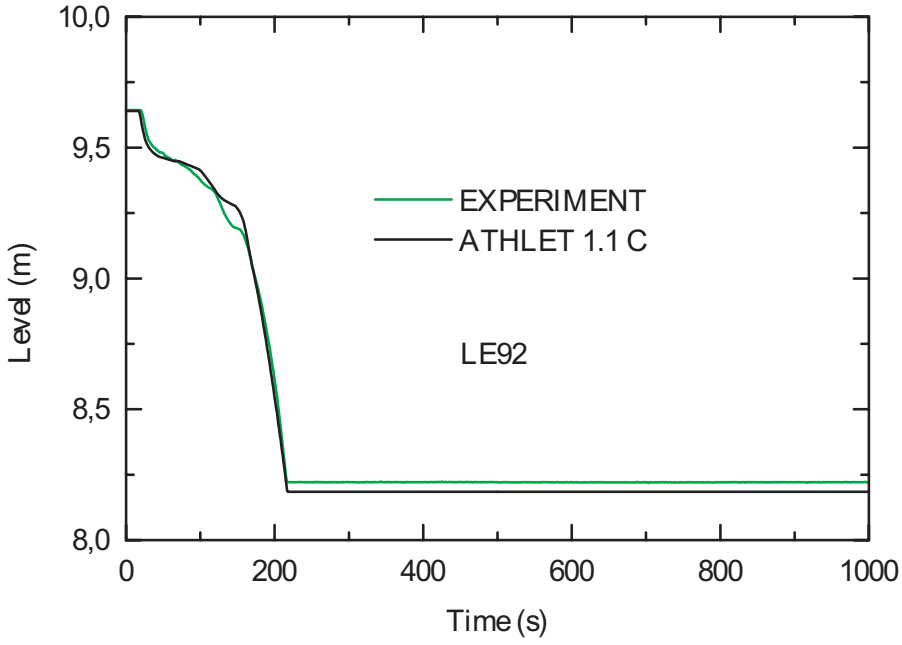

Fig. 5: Level in the hydroaccumulator (LE92)

The cold water injected from the hydroaccumulator flows partly to the upper plenum and to the hot leg. In the period from 70 s to 230 s strong oscillations in the hot leg loop seal level (LE31, Fig. 6) can be observed, the void fraction in the hot leg fluctuates between 0 and 100 %. In the experiment the hot leg loop seal is cleared and refilled four times. The calculation shows clearly the same phenomenon, but the hot leg loop seal is emptied and refilled only three times. The final loop seal clearing can be observed when the injection from the hydroaccumulator has stopped. The hydroaccumulator is emptied at t=217 s (LE92, Fig. 5) and the final loop seal clearing takes place at t=220 s in the experiment and at t=230 s in the calculation (LE31, Fig. 6). After the final loop seal clearing the void fraction in the hot leg reaches 100 % and the break flow changes to single phase vapor flow (FL01, Fig. 4). After t=200 s measured and calculated void fraction indicate steam flow even in the steam generator cold collector and the cold leg of the primary loop.

The fast decrease in the reactor coolant level (LE11, Fig. 3) leads to an extended dry-out in the reactor core (TE11-15, Fig. 7 and Fig. 8). In the experiment this dry-out starts at t=210 s, in the calculation at t=236 s. In the experiment the maximum cladding temperature was reached at t=444 s and in the calculation at t=398 s. The reactor coolant level (LE11, Fig. 3) reached an

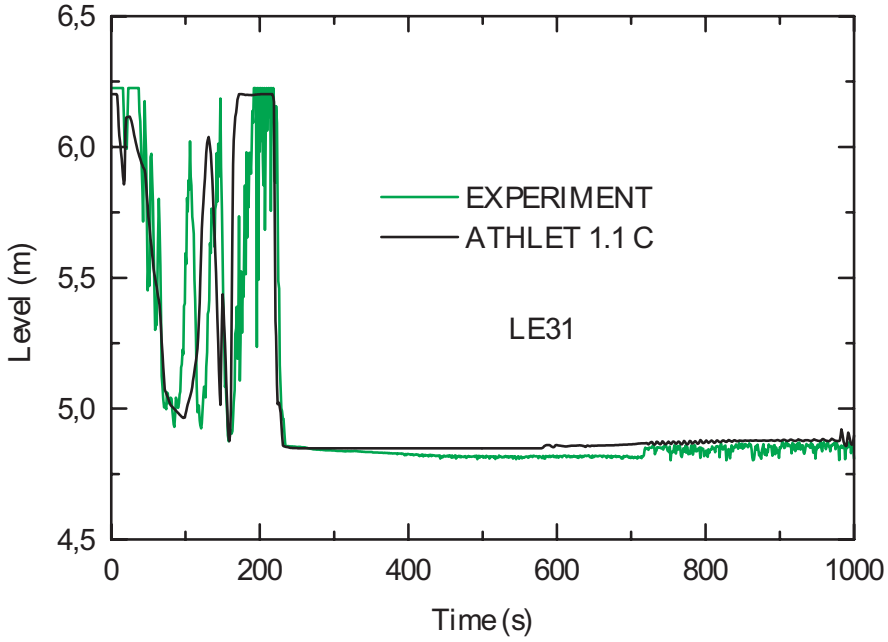

Fig. 6: Level in the hot leg loop seal (LE31)

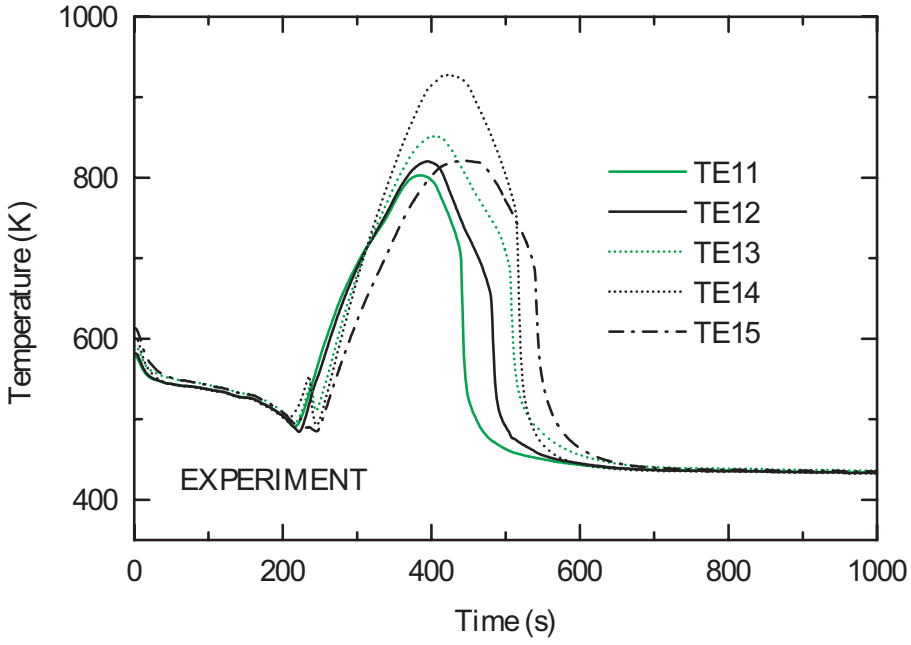

Fig. 7: Cladding temperatures in the reactor core (TE11-TE15) - experiment
(TE11: z=1.5m, ..., TE15: z=3.5m)

absolute minimum from t=255 s to 360 s in the experiment and from t=260 s to 312 s in the calculation. Due to the initiation of the low pressure injection system the coolant level in the reactor and in the downcomer rises again. The start of the low pressure injection system is initiated by the primary pressure signal at t=304 s in the experiment and at t=293 s in the calculation. In the

assumed accident scenario both experiment and calculation show, that the provided emergency core cooling systems can prevent core damage. After the initiation of the low pressure injection system the increasing reactor coolant level ensures core cooling up to the end of the experiment. After reflooding in both experiment and calculation the void fraction in the hot leg slightly decreases. The break flow changes from single to two-phase flow with a slightly increased mass flow rate from t=700 s up to the end of the transient (FL01, Fig 4). The reactor coolant level (LE11, Fig. 3) is stabilized at t=750 s in the experiment and at t=850 s in the calculation.

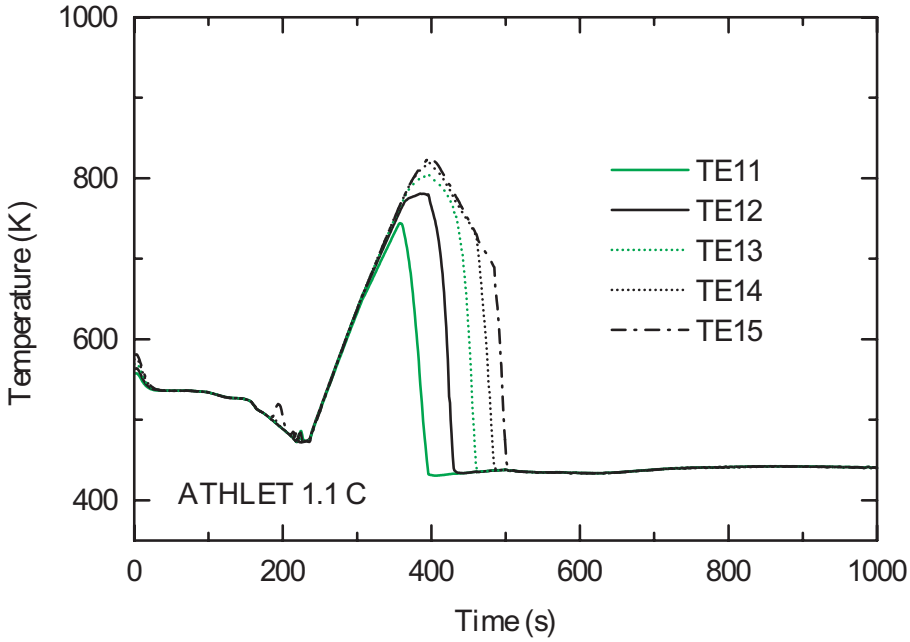

Fig. 8: Cladding temperatures in the reactor core (TE11-TE15) - calculation
(TE11: z=1.5m, ..., TE15: z=3.5m)

6. Conclusions

In the presented ATHLET calculation all main phenomena of the experiment, in particular the complex behaviour of the hot leg loop seal in connection with the hydroaccumulator injection, phase changes in the break flow, the dry-out of the core and the reflooding phase initiated by the low pressure injection system are calculated in a good agreement with the experimental results.

The experiment and the calculation showed, that the described accident scenario can be controlled by the available ECC systems. The reduced high pressure injection and the one hydroaccumulator are not sufficient to prevent core damage. Only the low pressure injection provides long term residual heat removal conditions.

References

[1] W. Horche, E. Krepper, F. Schäfer, I. Trosztel (1997), Summary Technical Report of PMK-2 Test No. 2 - Pressuriser Surge Line Break. Verification Report. Gesellschaft für Anlagen- und Reaktorsicherheit mbH, Garching.

[2] Central Research Institute for Physics (1990), Description of the PMK-NVH Facility.

ANALYSIS OF THE OECD MSLB BENCHMARK USING THE COUPLED CODE DYN3D/ATHLET

Sören Kliem, Ulrich Grundmann, Ulrich Rohde

1. Introduction

3D neutron kinetics core models have been coupled to advanced thermohydraulics system codes. These coupled codes can be used for the analysis of the whole reactor system. A benchmark task to compare different coupled codes for reactors with quadratic fuel assembly cross section geometry was defined by the Pennsylvania State University (PSU) under the auspices of the OECD/NEA [1]. The reference problem chosen for this benchmark is a main steam line break (MSLB) at end of cycle (EOC) and full power conditions. It is based on real plant design and operational data for the TMI-1 nuclear power plant. TMI-1 is a two-loop B&W designed plant with once-through-steamgenerators.

For the calculation of this benchmark, performed in the Institute of Safety Research of the Forschungszentrum Rossendorf the 3D neutron kinetics core model DYN3D [2] coupled to the thermohydraulics system code ATHLET [3] was used. The coupling was accomplished in an external way, where the core is completely modeled by DYN3D including the thermohydraulics [4].

The core was modeled with one node per assembly in radial and 28 layers in axial direction. The cross section library was provided by the PSU. This library covers only the moderator density range from 641.4 kg/m^3 up to 810.1 kg/m^3. In case of exceeding this range which occurs during the transient, the boundary values have to be taken. In spite of the calculations, submitted for code comparison within the benchmark work, where this approach was realized, in the calculations presented here an extrapolation of the cross section data beyond the highest density value is applied. It allows a more realistic comparison with the point kinetics analysis being a part of this benchmark where the feedback is described by reactivity coefficients.

For the modeling of the remaining plant components, an exisiting ATHLET input data deck for the TMI-2 plant was modified and extended. The extension concerns especially the secondary side, where the two main steam lines of the steamgenerator (SG) affected by the leak were modeled in detail.

The degree of mixing of coolant from different loops inside the reactor pressure vessel (RPV) is considered by a mixing ratio, which is based on mixing tests carried out at a similar power plant. These tests define the degree of mixing that occurs within the RPV as a ratio of the difference in hot leg temperatures to the difference in cold leg temperatures:

$$\text{Ratio} = (T_{hot}(\text{intact})-T_{hot}(\text{broken}))/(T_{cold}(\text{intact})-T_{cold}(\text{broken}))$$

The ratio was chosen to be equal to 0.5. 20 % of the heat is exchanged in the lower plenum and 80 % in the upper plenum.

The application of this mixing formula requires a full splitting of the two loops of the reactor

not only outside but also inside the RPV. In the upper head, cross connections between the two loops were introduced to keep the loop pressures in balance. The desired amount of flow mixing is obtained by energy exchange between the two control volumes in the lower and in the upper plenum, respectively. As a more detailed mixing model does not exist it is assumed, that one half of the fuel assemblies is supplied by the coolant with the lower temperature (mainly from the broken loop) and the other one by the coolant with the higher temperature.

2. Accident progression and results

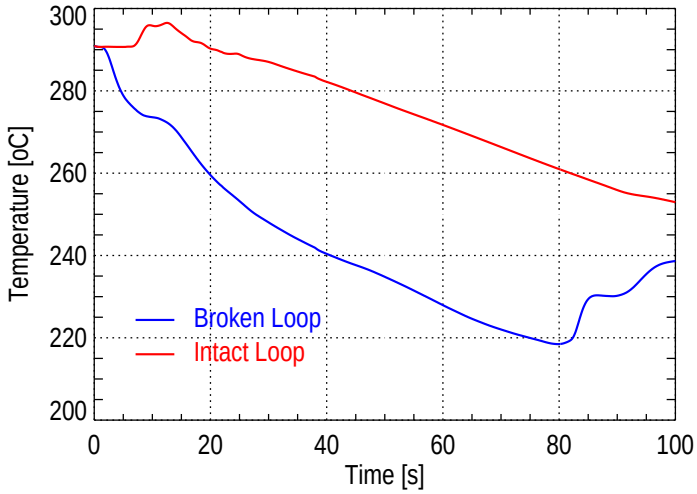

Fig. 1: Cold leg temperatures in the basic calculation

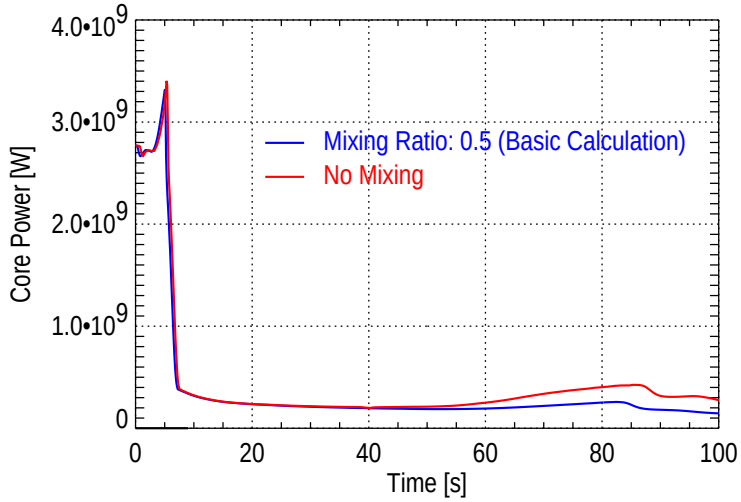

Fig. 2: Core power in the different DYN3D/ATHLET calculations

The transient is initiated by a sudden rupture of one main steam line upstream of the main steam isolation valve. Therefore, the affected SG cannot be isolated from the leak and so the rapid pressure decrease leads to an increasing heat transfer to the secondary side and to an overcooling of the corresponding part of the primary circuit. Due to the strong negative moderator temperature coefficient, the overcooling causes a core power rise. The high neutron flux scram set point of 114% is reached 4.99 s after the leak opening. An asymmetrical stuck rod is assumed for the scram. After the scram, the overcooling continues.

Fig. 1 shows the temperature in the cold leg of both loops. The temperature difference between the two cold legs rises up to 40 K. In the intact loop, a reverse heat transfer from the secondary to the primary circuit occurs. This hotter coolant is than partly mixed (according to the mixing ratio) with the coolant of the loop with the affected SG. Together with the decay heat, this leads to a rise of the temperature difference to about 18 K between cold and hot leg in this loop. The overcooling in the SG of this loop is higher than the sum of the decay heat and the reversal heat transfer. Therefore the core inlet temperature for both sectors decreases continuously. This overcooling leads to a compensation of the negative reactivity inserted by the scram. From t = 50 s on, the reactor power begins to rise

(basic calculation in fig. 2). The reactor returned to power. At about t = 80 s, the affected SG becomes emptied. The heat transfer and the corresponding overcooling are suddenly stopped. The power rise is stopped, too. The maximum power reached during this second power rise corresponds to about 9 % of the nominal power.

3. Influence of the coolant mixing on the core behaviour

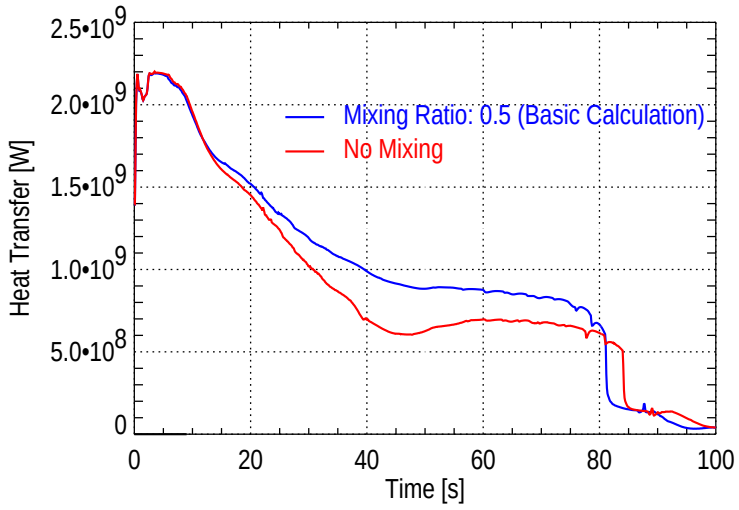

Fig. 3: Heat transfer in the affected SG in the different calculations

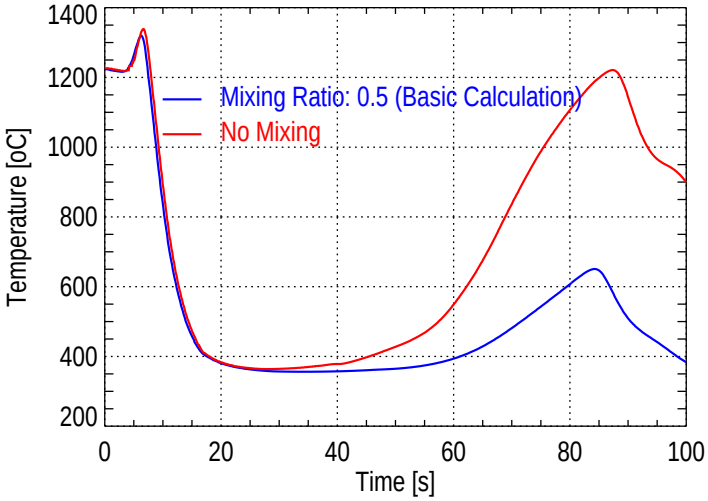

Fig. 4: Maximum fuel temperature in the different DYN3D/ATHLET calculations

To assess the influence of the mixing, sensitivity studies were carried out, where the mixing inside the RPV was inhibited at all. In the absence of mixing, the temperature difference between cold and hot leg of the affected loop is only caused by the decay heat. Therefore, the heat transfer to the secondary side in the affected loop is smaller than in the basic calculation (fig. 3). That means, that the global overcooling of the reactor is smaller, too! On the other hand, the coolant of the affected loop enters only the corresponding half of the core, where the stuck rod is located. This leads to a higher core power rise (about 15 %) than in the basic calculation (fig. 2). Although the heat transfer in the affected SG is lower than in the basic calculation, the coolant at the entry of the affected core half has a lower temperature due to the exclusion of mixing. This is the reason for the higher energy release in the core, especially in the affected region. It can be seen in the maximum fuel temperature which reached a value of about 1200 ^{o}C. This is nearly the same temperature as in the steady state (fig. 4). In the basic calculation, only a value of about 650 ^{o}C was reached.

The main goal of the OECD MSLB Benchmark is the validation of coupled 3D neutron kinetics/ thermohydraulics codes. However in the first phase of the benchmark, a point kinetics calculation had to be carried out using coefficients derived from 3D nodal core calculations with the same cross section data, provided for the calculation presented above. Special attention was

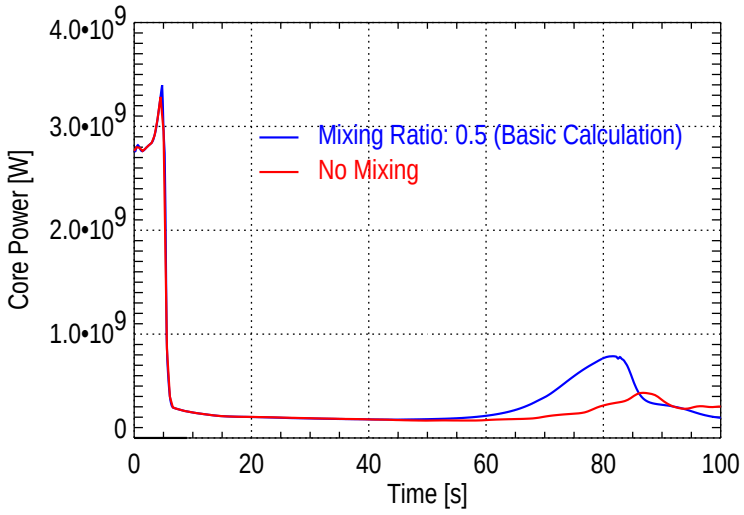

Fig. 5: Core Power in the different point kinetics calculations

paid to make both calculations comparable. The thermohydraulics parameter in the coupled and the point kinetics calculations behave very similar, but the power in the point kinetics calculation (28% of the nominal power) is about three time higher than that of the coupled calculation (fig. 5). The maximum fuel temperature reached during the point kinetics calculation is less than 400 ^{o}C. This is mainly due to the fact, that the asymmetric power distribution in the core is not considered in this calculation. The comparison of these two calculations demonstrates the superiority of the coupled 3D neutron kinetics/thermohydraulics plant model. The variation of the mixing in a sensitivity calculation with the point kinetics model shows a lower power peak (fig. 5). This is due to the fact, that the core power is calculated using only the core averaged moderator temperature value. The spatial distribution of the core inlet temperature has no influence on the feedback. Therefore, the smaller heat transfer in the calculation without mixing is responsible for the lower power peak.

As can be seen, the changes of the coolant mixing conditions inside the RPV have an opposite effect on the power behaviour in the coupled 3D neutron kinetics/thermohydraulics and the point kinetics calculations.

References

[1] K. Ivanov, T. Beam, A. Baratta, A. Irani, N. Trikouros (1999), Pressurized Water Reactor Main Steam Line Break Benchmark - Volume 1: Final Specifications, NEA/NSC/DOC (99) 8, US Nuclear Regulatory Commission, OECD/NEA

[2] U. Grundmann, U. Rohde (1996), DYN3D - A 3-Dimensional Core Model for Steady State and Transient Analysis in Thermal Reactors, Proc. of the Int. Conf. on the Physics of Reactors PHYSOR96 (pp. J-70 - J-79) Mito, Japan

[3] V. Teschendorff, H. Austregesilo, G. Lerchl (1996), Methodology, status and plans for development and assessment of the code ATHLET, Proc. OECD/CSNI Workshop on Transient Thermal-Hydraulic and Neutronic Codes Requirements, NUREG/CP-0159, NEA/CSNI/R(97)4

[4] U. Grundmann, D. Lucas, U. Rohde (1995), Coupling of the Thermohydraulic Code ATHLET with the Neutron Kinetic Core Model DYN3D", Proc. Int. Conf. on Mathematics and Computations, Reactor Physics, and Environmental Analyses (v. 1, p. 257), Portland, Oregon

CALORIMETRIC INVESTIGATION OF THE FORMATION OF GRIGNARD REAGENTS

Günther Hessel, Günther Hulzer[1], Holger Kryk, Peter Palitzsch[1], Wilfried Schmitt, Nurelegne Tefera, Frank-Peter Weiss

1. Introduction

In the fine-chemical and pharmaceutical industry, Grignard reagents are of enormous importance as an initial stage of numerous organic syntheses. Due to the spontaneous heat release during the initiation of this strongly exothermic reaction, Grignard reactions dispose of considerable harzard potentials. Therefore, the knowledge of thermodynamic and thermokinetic parameters is one of the prerequisites for safe formation of Grignard reagents in production plants. In literature, measurement values of the molar reaction enthalpy have only been known for a few Grignard compounds. Up to now the calorimetric investigation of Grignard reactions has been carried out at reflux conditions to control the spontaneous heat release by means of hot cooling (cooling by evaporation). However, calorimetric measurements under reflux conditions are connected with a higher error (about ± 30%) than in closed systems (about ± 10%) due to additional heat losses and the evaluation of the heat of reflux. To obtain more accurate results, these studies on the formation of Grignard reagents were carried out in a closed reaction calorimeter for the first time.

2. Preparation of Grignard reagents

Reactions between organic halides and solid magnesium are the most common method to prepare Grignard reagents. As a model reaction, the direct reaction between the bromobenzene derivative and solid magnesium was studied. The brutto reaction equation can be written as follows

$$\underset{\text{bromobenzene derivative}}{R-Br} \quad + \quad \underset{\text{magnesium}}{Mg(s)} \xrightarrow{THF} \underset{\text{organomagnesium bromide}}{R-Mg-Br} \tag{1}$$

To initiate the formation of Grignard reagents, the organometallic compound (R-Br) has to be solvated by the tetrahydrofurane solvent (THF). Additionally, active centres (radicals) have to be formed on the magnesium surface. When forming the Grignard reagent (R-Mg-Br), the magnesium radical is inserted between the rest of the organic molecule (R) and the bromine (Br). After an induction time, the Grignard reaction seems to go autocatalytically. That means when a critical amount of the Grignard reagent was formed, new active centres are exposed and subsequently the rate of reaction increases exponentially. The runaway reaction is only stopped when one reactant is consumed. Since Grignard reactions are highly exothermic, a thermal explosion could occur if a large amount of organic halides was added during a long induction time. The reasons for non-reproducible and long induction times or even uninitiated Grignard reactions could be:

[1] Arzneimittelwerk Dresden GmbH (AWD)

- trace amounts from water, oxygen or alcohol which immediately react with the Grignard reagent or with magnesium to form insoluble hydroxide or alkoxide salts that coat the surface of the metal
- magnesium with an oxide film which must be penetrated for reaction with the organic halide.

For safety reasons an experiment should be terminated if the maximum permitted amount from the organic halide did not initiate the Grignard reaction.

3. Performance of calorimetric measurements

The studies were carried out in the RC1 reaction calorimeter equipped with the pressure vessel HP60 and an anchor stirrer. For on-line concentration measurements the Fourier-Transform-Infrared (FTIR)-spectrometer ReactIR 1000 was used (Fig.1). To improve the accuracy of the calorimetric measurements, the experiment was divided into two stages:

- initiation reaction at the boiling point of the THF solvent
- main reaction at the isothermic reaction temperature

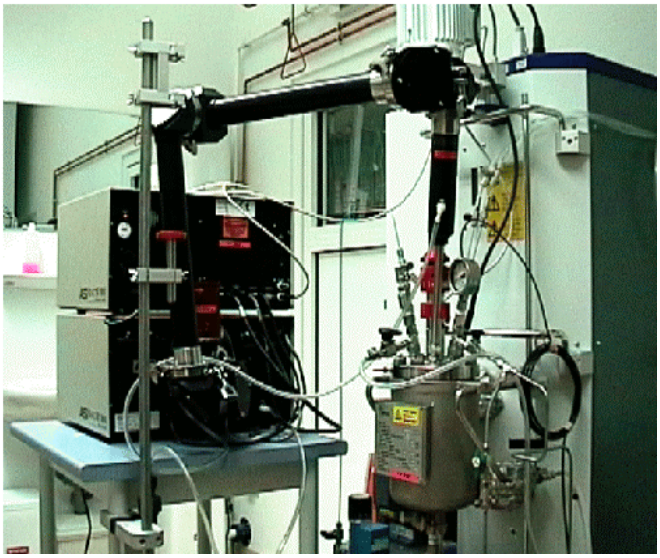

Fig. 1: RC1 reaction calorimeter with FTIR-spectrometer

First, the total amounts of magnesium shavings and anhydrous THF solvent were added into the reactor under agitation (1000 rpm) and degassed with nitrogen. To initiate the Grignard reaction, the mixture has to be heated up to 70°C. When this temperature was kept constant, part of bromobenzene derivate was added gradually up to initiating the formation of the Grignard reagents (see Fig. 2). After this initiation process the reaction mixture was cooled down to the desired temperature of the main reaction. To determine the heat of reaction and kinetic parameters, the stage of the main reaction was performed under isothermal conditions (see Fig. 3).

4. Results and discussion

The formation of the Grignard reagent was studied with respect to the initiation behaviour, the heat of reaction and kinetic parameters. In Fig. 2, the initiation is depicted for the used semi-batch process. This initiation process can be characterised by the so-called induction time (t_{ind}), the period of initiation (t_{ini}) and the released heat of reaction (Q_r). The induction time is defined by the duration of dosing up to initiating the Grignard formation, while the period of initiation corresponds to the duration of heat production. Well-reproducible induction times were obtained when the pure bromobenzene derivative was added with a constant rate of dosing into the reactor containing the total amount of magnesium and tetrafurane at 70°C and

a stirrer speed of 1000 rpm. The initiation of the Grignard reaction can be recognised both by the decreasing concentration of the bromobenzene derivative and by the increasing concentration of the Grignard reagent shown in Fig. 2.

Some seconds later the heat release rate also increases gradually and then after about 4 minutes it rises steeply. The rapid rise in the heat release rate and in the concentration of the Grignard reagent can also be detected by a steep increase in pressure because a closed reactor vessel was used for the calorimetric measurements. Depending on the accumulated amount of bromobenzene derivative and on the power of the jacket cooling, the period of initiation will last over about 10 minutes.

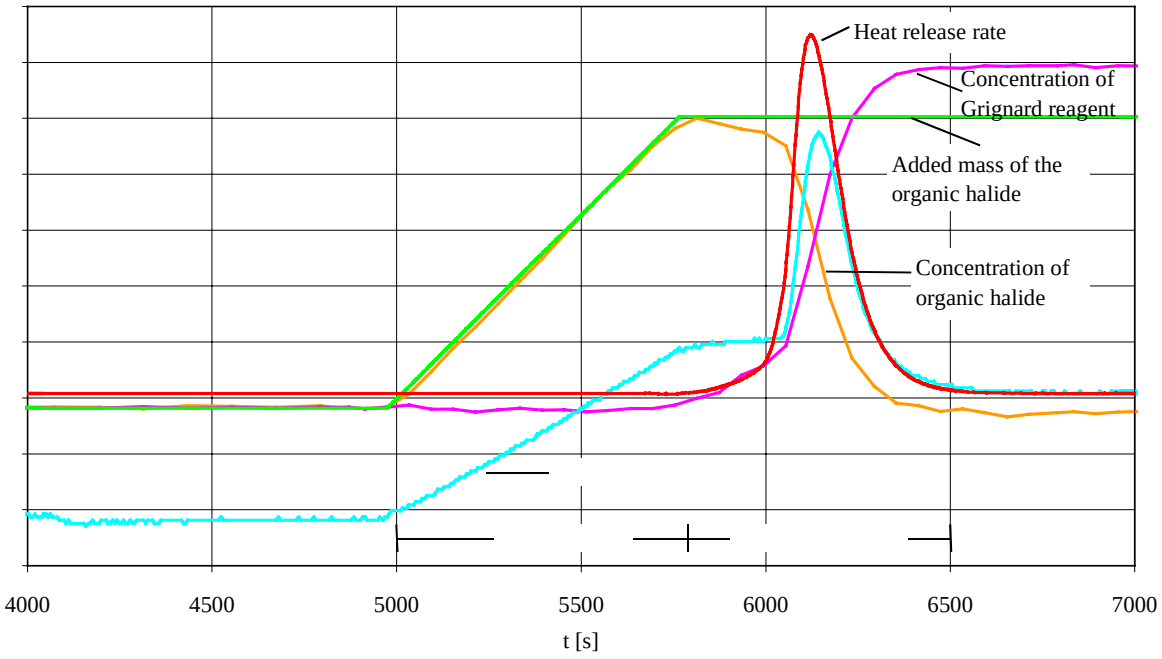

Fig. 2: Profiles of process variables during the initiation of the Grignard reaction at 70°C.

To determine the molar reaction enthalpy and kinetic parameters, the stage of the main Grignard reaction was carried out in semibatch operation under isothermal conditions. Figures 3 shows profiles of several selected process variables during the isothermal period. By gradually adding the bromobenzene derivative, the heat release rate could almost be kept constant. As shown by the profile of concentration of the bromobenzene derivative, an accumulation of the reactant was prevented. The increase in pressure mainly resulted from the increasing filling volume. The measured heat of reaction Q_r and the molar reaction enthalpy ΔH_r are listed in Tab. 1 at different isothermal reaction temperatures. An influence of the reactor temperature on the heat release rate was not stated in the range from 40 °C to 70 °C as shown in Fig. 4.

As a result of the calorimetric measurements, a mean molar reaction enthalpy per mole bromobenzene derivative was determined:

$$\Delta H_r = (270 \pm 6)\, kJ / mol \quad .$$

To model the Grignard reaction kinetics of the main reaction stage, the above experiments were adopted. This shows that the main reaction stage is only controlled by the dosing rate of the bromobenzene derivative.

Table 1: Heat of reaction and molar reaction enthalpy of the Grignard reaction for different reactor temperatures

Experiment	Tr [°C]	N_{BBD} [1)] [mol]	Qr [kJ]	ΔHr [kJ/mol]	$\overline{\Delta H_r}$ [kJ/mol]
BA14	40	0,4332	117,9	272,2	
BA15	40	0,4332	115,8	267,3	
BA16	40	0,4332	118,0	272,5	270,7
BA17	50	0,4332	115,1	265,6	265,6
BA11	60	0,4332	120,0	277,1	
BA12	60	0,2513	68,6	272,9	
BA13	60	0,4332	118,7	274,0	274,7
BA7	70	0,4813	128,4	266,9	
BA9	70	0,4332	115,5	266,5	
BA10	70	0,4332	117,9	272,2	268,5

1) Mole of bromobenzene derivative

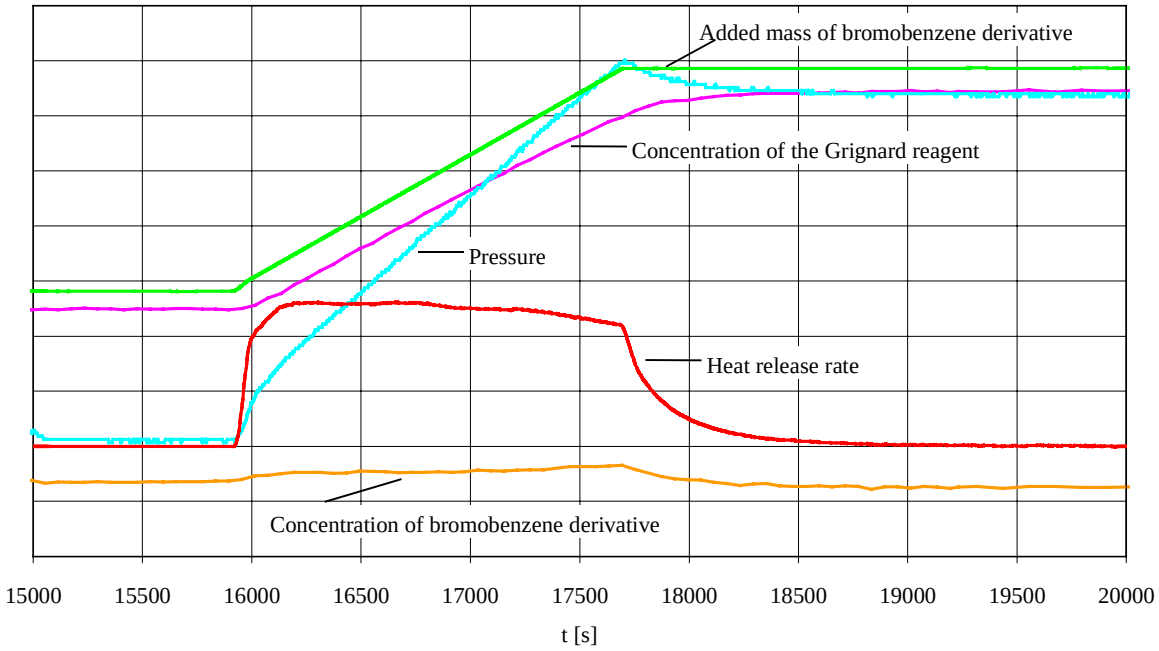

Fig. 3: Profiles of process variables during the main Grignard reaction under isothermal conditions

Therefore, the following rate equation for this type of reaction can be assumed:

$$r = k\,[R-Br]^{\alpha}\;[Mg]^{\beta}$$

For modelling this process, the experiment was conducted in a quasi batch mode (Fig. 5). From these experiments the following model parameters were determined using the Batch-CAD program RATE (Tab. 2).

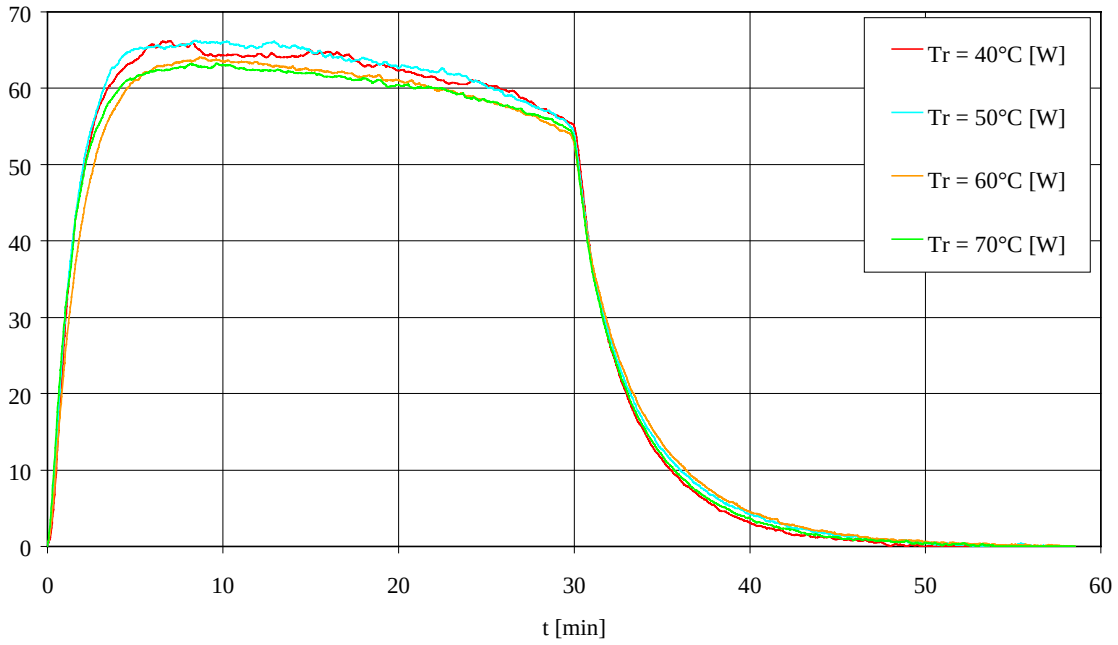

Fig. 4: Influence of the reactor temperature on the heat release rate during the main reaction.

Table 2: Grignard reaction of the bromobenzene derivative with Mg at 40°C.

Reaction stage	k [l/mol s]	k / [Mg]
2	$1.5720 \cdot 10^{-2}$	$1.5542 \cdot 10^{-2}$
3	$1.2557 \cdot 10^{-2}$	$1.9348 \cdot 10^{-2}$
4	$0.9092 \cdot 10^{-2}$	$2.1678 \cdot 10^{-2}$
5	$0.6472 \cdot 10^{-2}$	$2.3670 \cdot 10^{-2}$

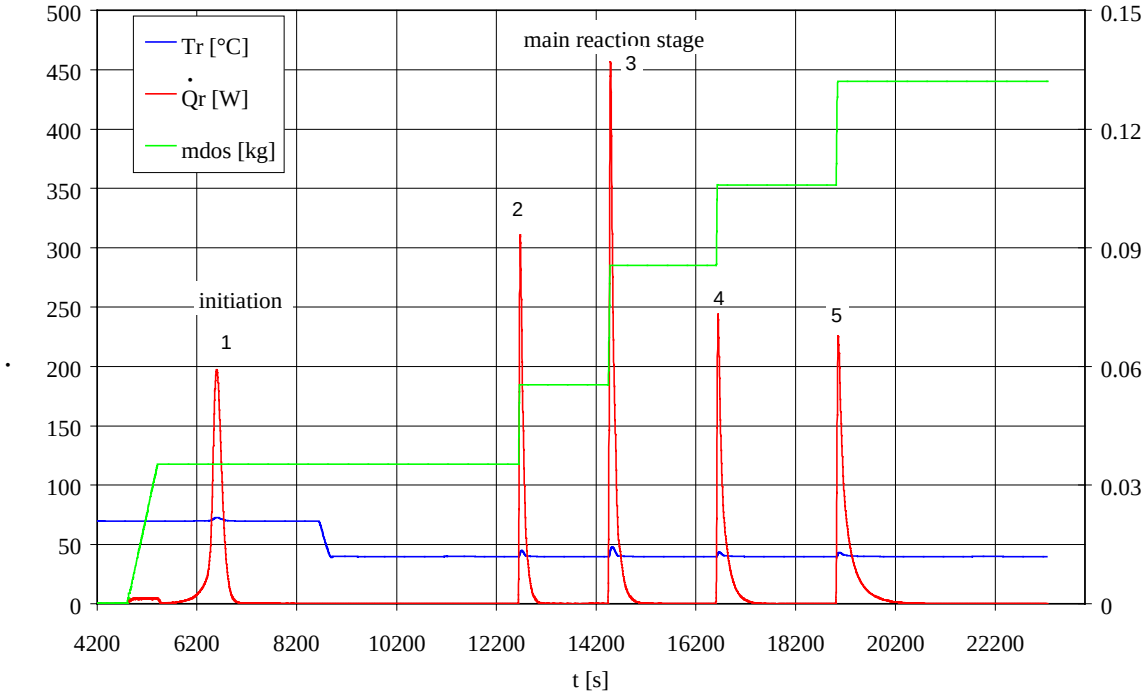

Fig. 5: Grignard reaction in the quasi batch mode

Figure 6 compares the model and experimental results for the second reaction stage. There is a good agreement between model and experiment for the first three main reaction stages. So, the reaction is of the first order $\alpha = 1$ in the concentration of the bromobenzene derivative and of zero order $\beta = 0$ in the concentration of Mg. When the concentration of Mg decreases (stage 5), the rate of reaction depends on the concentration of Mg. The reaction order is then found to be $\beta = 0.5$. Further investigation is necessary to study the influence of temperature on the rate of reaction during the quasi batch regime.

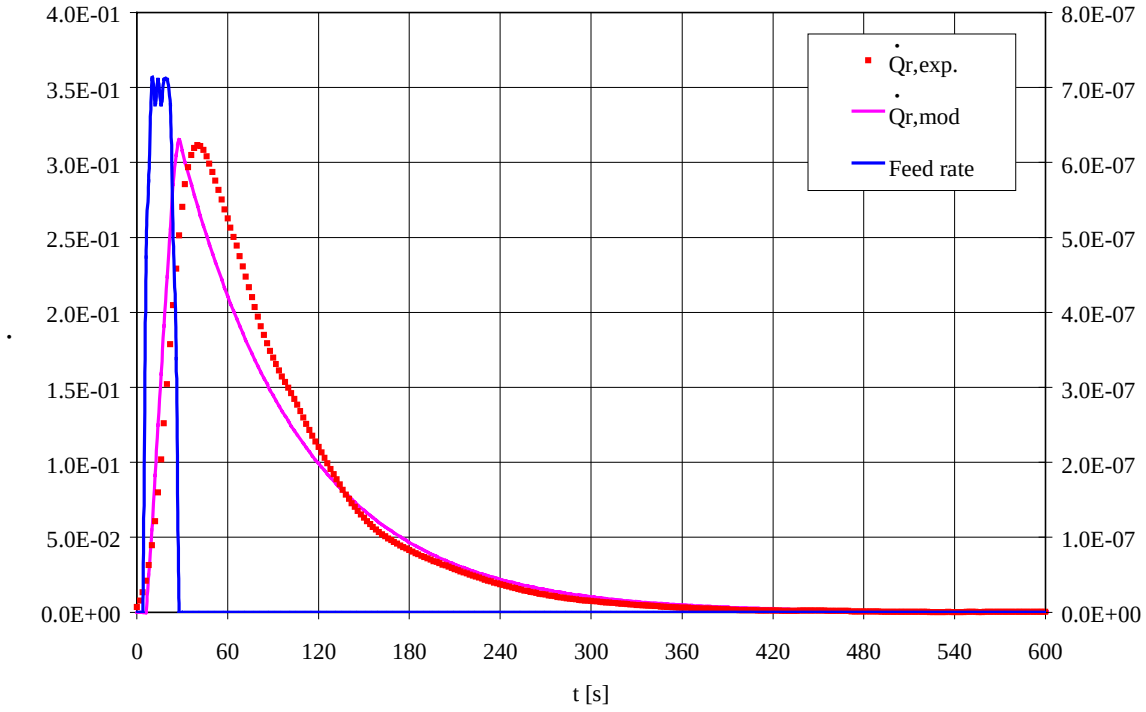

Fig. 6: Comparison between model and experiment results (stage 2).

5. Conclusions

A novel technique was applied to determine of the thermodynamic and kinetic parameters of Grignard reactions. Instead of operating under reflux conditions which are commonly used to control the spontaneous strongly exothermic initiation of Grignard reactions, the calorimetric measurement was carried out in a closed reactor pressure vessel. In that way the increase of the reactor temperature and the pressure can be used for detecting the initiation of the Grignard formation as shown by the comparison with the on-line profiles of the concentration of the Grignard reagent measured simultaneously by FTIR-spectroscopy. Results showed that the molar reaction enthalpy of a Grignard reagent could be determinated by a closed reactor vessel more accurately than under reflex conditions.

VALIDATION OF THE BRICK CODE WITH DATA FROM PRESSURE RELIEF EXPERIMENTS IN CASE OF RUNAWAY REACTIONS

Dirk Lucas

1. Introduction

Usually batch or semi-batch reactors are used for exothermic reactions. Often the reaction systems and the process control change. For this reason they imply a high risc potential. The reliable design of the emergency pressure relief system is very important to guarantee the safe operation of such reactors.

For the one-dimensional transient simulation of pressure relief processes the new BRICK code was developed [1,2]. The code was verified by many test cases including comparisons with analytical solutions for special cases. Examples for the validation of the code by depressurization experiments with water/steam are given in [1,2]. But to apply the code to the design of pressure relief systems of batch reactors it has to be validated for realistic reaction systems. Up to now 3 different systems were used for the validation, which represent 3 different situations. The first reaction is the esterification of methanol and acetic anhydride. In this case the pressure is caused by the evaporation of the components. The second is the decomposition of ammonium peroxydisulphate, where the pressure mainly builds up from the release of oxygen and the third is the thermal decomposition of hydrogen peroxide. This is a so called hybrid system, what means, that the increase of pressure results from the production of gas as well as from the evaporation.

2. Experiments

Data of pressure relief experiments for the esterification of methanol and acetic anhydride as well as for the decomposition of ammonium peroxydisulphate were available by courtesy of Wilhelm-Jost-Institut Hamm. The reactor has a height 1 meter and a diameter of 0.6 meter. This corresponds to a volume of 280 litres. For both reaction systems the kinetics of the reactions were investigated by calorimeter experiments at the Inburex GmbH Hamm. The data are also kindly placed at our disposal.

The most important parameter for these experiments are listed in the tables 1 and 2. For the esterification an initial composition of 38,6 wt-% methanol and 61,4 wt-% acetic anhydride was used. The initial concentration of ammonium peroxydisulphate was 35 wt-%.

Table 1: Calorimeter experiments - Inburex GmbH Hamm

Parameter	Esterification	Decomposition
Volume of the test cell	110 ml	120 ml
Mass of reaction mixture	73 g	75 g
Filling	70 %	70 %

Table 2: Pressure relief experiments - Wilhelm-Jost-Institut Hamm

Parameter	Esterification	Decomposition
Diameter of the orifice	13 cm	10 cm
Filling	90 %	80%

Small scale experiments with the thermal decomposition of hydrogen peroxide were done at our institute [3]. A 1.95 litre vessel was filled with 1 litre of 5, 10, 15, 17.5 and 20 wt-% H_2O_2 solution. Discharge orifices of 0.7 mm, 1 mm and 2 mm were used. The decomposition was initiated by an external heating. Experiments were carried out with a complete decomposition before starting the relief as well as with a relief during the runaway.

3. Esterification of methanol and acetic anhydride

In a first step, calculations for the calorimeter experiment were done. In this experiment the reaction is completed without pressure relief. After the completed reaction there is a slight decrease of temperature and pressure because of the loss of heat. Using a heat-transfer coefficient of 6 W/(m^2 K), the temperature decrease of the calculation agrees with the experiment. This is the only parameter adapted for the calculation. A very good agreement of the time dependent temperature and pressure curves was achieved. This means the modules for chemical

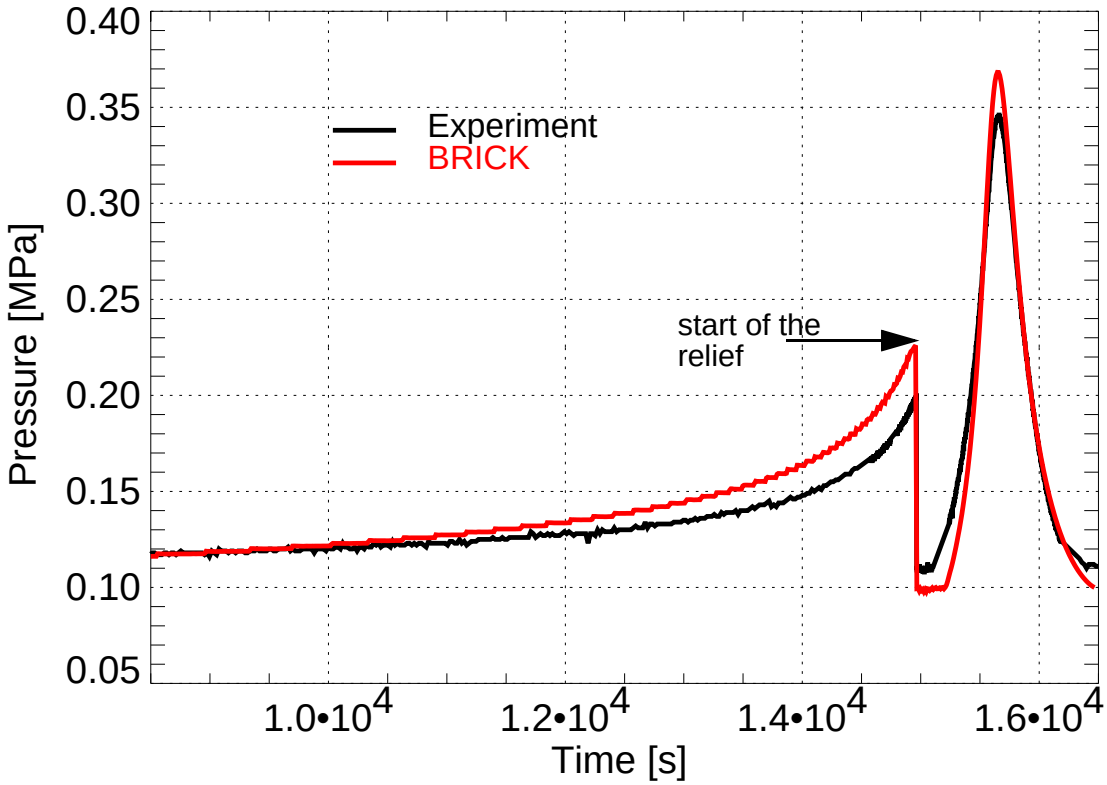

Fig. 1: Comparison of measured and calculated pressure in case of the 280 litre pressure relief experiment with the runaway esterification of methanol and acetic anhydride

reaction, phase transfer as well as for the calculation of material properties work well for this case.

Fig. 1 shows a comparison of the experimental and calculated pressure for the 280 litre pressure relief experiments. The pressure relief was started in the calculation, when the experimental starting temperature of the experiment was achieved. After starting the relief the pressure decreases rapidly to ambient pressure. However the cooling caused by evaporation is not sufficient to stop the reaction. For this reason the temperature even increases after the relief. The pressure peak caused by the runaway reaction is higher than the opening pressure. This is reflected very well by the calculation. The increase of pressure before starting the relief was mainly caused by the expansion of the liquid phase and the corresponding compression of the non-condensible gas. Since here the pressure is only a function of the temperature, material properties and the amount of the non-condensible gas (assumption of an ideal gas), it can be calculated analytically. Also other parameters like the location of the top level of the liquid phase were compared with analytical calculations. The agreement of all these analytically calculated values and the values obtained by the BRICK code confirm the right implementation of the model in the code. Differences between experiment and calculation may be caused by non-ideal behaviour of the fluid.

The most important element of uncertainty in the calculation is the modelling of heat transfer to the outside of the vessel. The influence of the heat transfer is shown in fig. 2. Here only the pressure peak after starting the relief is shown (compare time scales of fig 1 and 2). The red curve shows the pressure without any heat removal from the liquid. In case of the green curve,

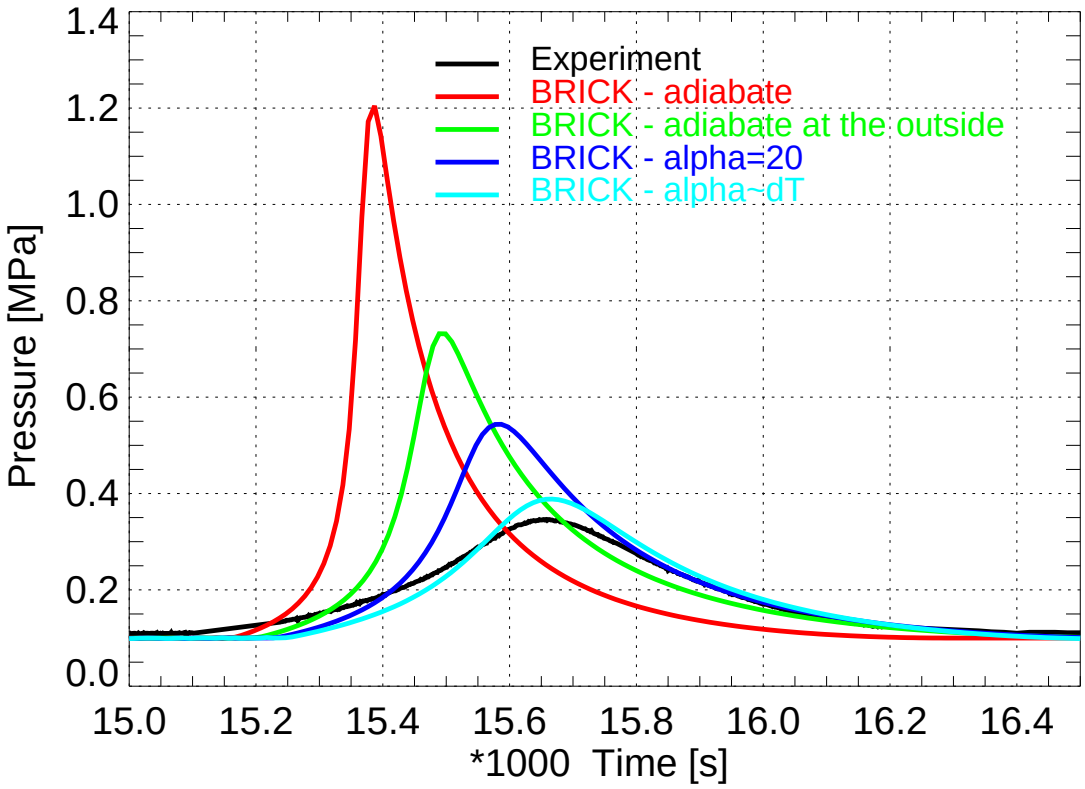

Fig. 2: Case studies for the influence of the heat transfer for the 280 litre pressure relief experiment with the runaway esterification of methanol and acetic anhydride

the vessel wall is considered, but no heat transfer to the outside of the vessel is assumed. The assumption of a constant heat transfer coefficient to the outside is more realistic. The best agreement between experimental and calculational results was achieved with a heat transfer coefficient, which is proportional to the difference of the temperatures of the outside vessel wall and the environment. That indicates a non-linear behaviour of the heat transfer. However a physically based modelling was not possible, because the conditions of the outside cooling of the vessel are not well known. For the calculations only one node was considered. That means, a point model is used for the balance of energy, but the phase distribution is considered in the calculation over the vessel height.

4. Decomposition of ammonium peroxydisulphate

Due to the lack of material data for ammonium peroxydisulphate the calculations were done using data for hydrogen peroxide. According to the calorimeter experiments, an initial mass fraction of 7% hydrogen peroxide was used in the calculation, what means approximately the same mole fraction as in the case of a 35 wt-% ammonium peroxydisulphate solution. With this assumption an ideal agreement of the experimental and calculated time dependent pressure and temperature curves was achieved for the calorimeter experiments.

Fig. 3 shows a comparison of the measured and calculated pressure curve for the 280 litre pressure relief experiment. The pressure peak caused by the runaway does not reach the opening pressure in this case. There is a significant difference in the pressure increase before the relief.

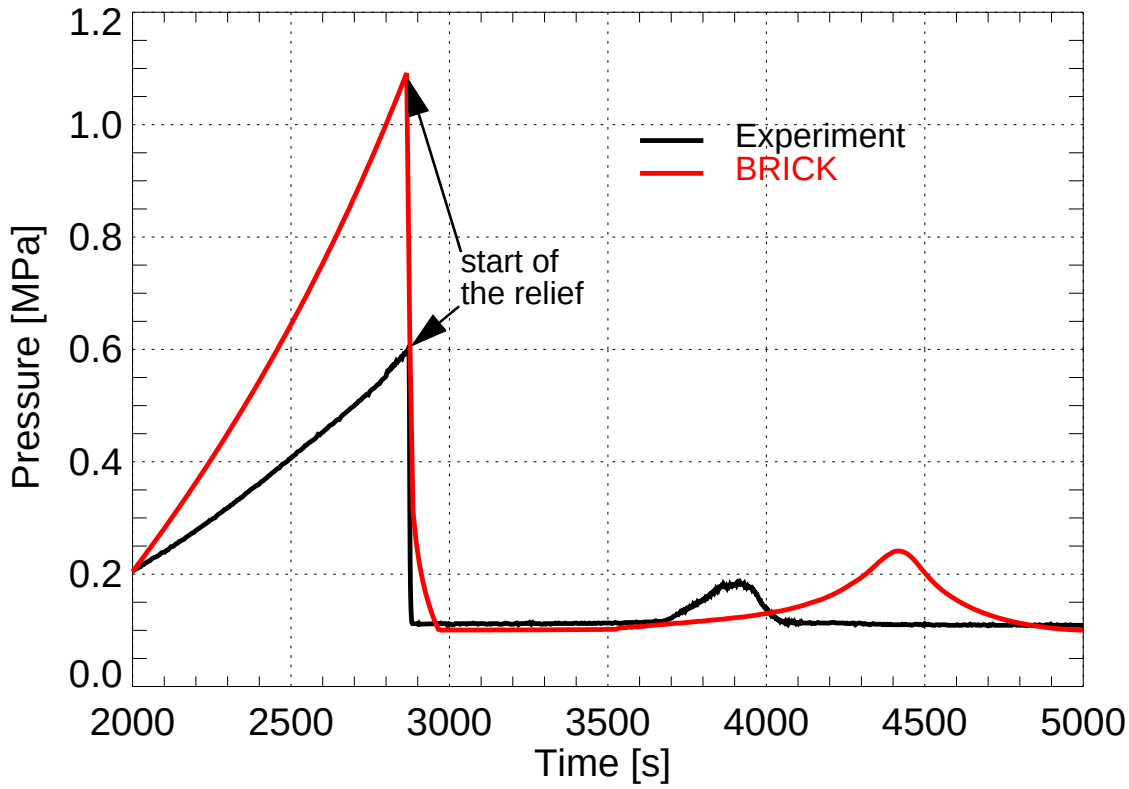

Fig. 3: Comparison of measured and calculated pressure in case of the 280 litre pressure relief experiment with the runaway decomposition of ammonium peroxydisulphate

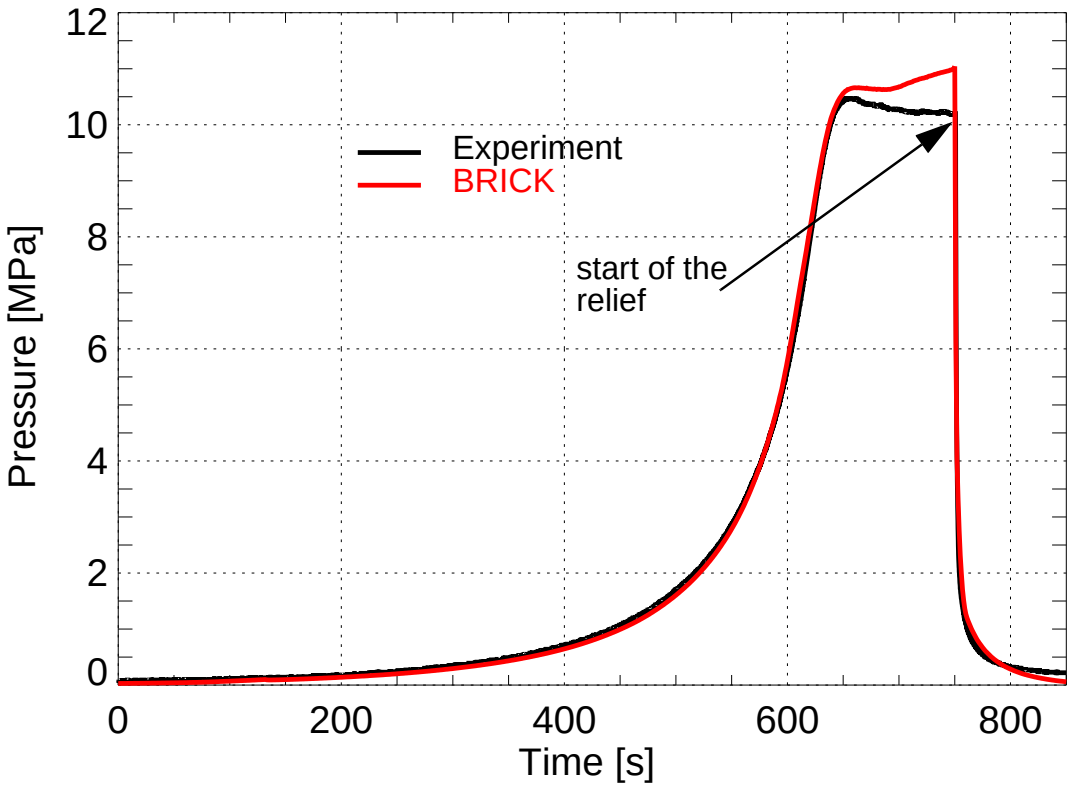

Fig. 4: Comparison of measured and calculated pressure in case of the 1.95 litre pressure relief experiment with the runaway decompostion of hydrogen peroxide (complete reaction)

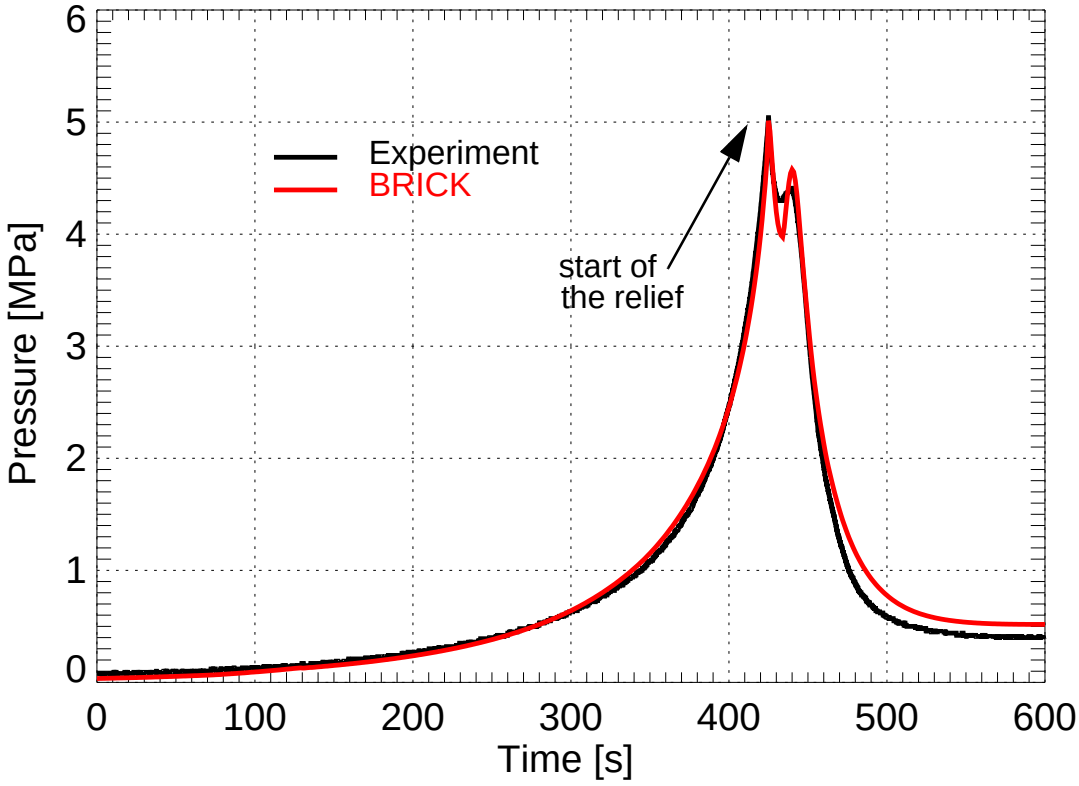

Fig. 5: Comparison of measured and calculated pressure in case of the 1.95 litre pressure relief experiment with the runaway decompostion of hydrogen peroxide (Relief at 5 MPa)

The reason for this difference is not clear. Analytical estimations confirmed the calculated increase of pressure. The runaway happens a little bit later in the calculation than in the experiment. Again the uncertainty of the heat transfer may be a reason for that.

5. Decomposition of hydrogen peroxide

Fig. 4 and 5 show the pressure as a function of time for an experiment with a complete reaction before starting the relief and an experiment with a pressure relief, which was started at a pressure of 5 MPa. In the first case a 2 mm orifice and in the second case a 0.7 mm orifice was used. In both cases a good agreement was achieved. The pressure recovery after starting the relief was obtained in the experiment and also in the simulation with the BRICK code. The heating of the vessel was an additional element of uncertainty. The heating power of the vessel wall was adapted in the calculation.

6. Conclusions

Comparisons of the parameters calculated by the BRICK code with analytical solutions, which may be obtained for some simple cases, showed, that the code works correct. The agreement of the calculated and measured parameters as a function of time is satisfactory in most cases. The main uncertainty in the calculation is the modelling of the heat transfer from the vessel to the environment. Improvements are necessary. In addition, models for the axial heat transfer both in the fluid and in the wall should be implemented.

References

[1] D. Lucas (1999a), BRICK - A1-D Tool for transient Multiphase Vessel Flow Simulations based on a new Particle Method, 2nd International Symposium on Two-Phase Flow Modelling and Experimentation, Pisa, Italy, May 23-26, 1999, Proceedings, Volume 3, pp. 1657-1664

[2] D. Lucas (1999b), BRICK - ein 1-D-Simulationstool für Mehrphasenströmungen in Behältern, Chemie-Ingenieur-Technik 71, Heft 7

[3] D. Lucas, H.-M. Prasser, T. Kern (1998), Die thermische Zersetzung von Wasserstoffperoxid als Modellreaktion für die Druckentlastung, 4. Fachtagung Anlagen-, Arbeits- und Umweltsicherheit, Köthen, 5./6. November 1998, Preprints P9

This work was supported by the Volkswagen-Stiftung.

GAS FRACTION, VELOCITY AND BUBBLE SIZE DISTRIBUTIONS IN A MODEL OF ALKALINE CHLORINE ELECTROLYSIS CELLS

Carola Schneider

1. Introduction

Chlorine is the raw material for many products in chemical and pharmaceutical industries as well as a reactive agent for numerous syntheses. Technologically, chlorine is mainly produced by alkaline chloride electrolysis. Since 1975 the older principles of the alkaline chloride electrolysis, diaphragm and amalgam, are increasingly replaced by membrane cells [1]. A simplified scheme of such a cell is illustrated in Fig. 1. Due to the lateral gas supply from the electrode the superficial gas velocity and as a consequence the gas fraction are increasing from the bottom to the top. Bergner [2] has found that the gas fraction at the top of the anode chamber of a 2.7 m² cell reaches 43 % at a current density of 3 kA/m². During the last years the performance of the cells was continuously increased. Now, typical values are about 5-6 kA/m². As a result the gas fraction was increased significantly reaching values typical for foam. The results concerning the characterisation of the axial gas fraction profile in the cell and the development of methods to remove or destroy the foam in the anode chamber were reported in the annual report 1997 [3].

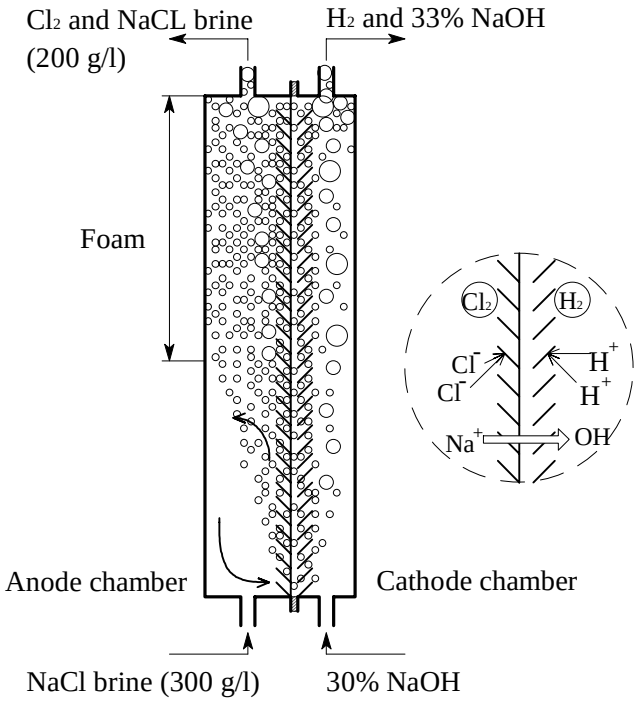

Fig. 1: Scheme of a membrane cell for alkaline chloride electrolysis

For the experimental investigation, hydrogen peroxide decomposition at a platinum surface was found to be a good model reaction. Gas fraction profiles and the efficiency of different foam-destroying measures were tested in two experimental mock-ups: a circular cell of 50 mm diameter and a 0.16 m² cell with rectangular cross section [3, 4]. This paper presents gas fraction and velocity profiles perpendicular to the catalyst, as well as bubble size distributions measured in the mentioned 0.16 m² H_2O_2 cell (Fig. 2). The aim of the measurements was to study the boundary layer at the gas evolving surface and to analyse the contribution of the natural circulation caused by the lateral gas supply to the efficiency of the gas removal from the anolyte. In order to create boundary conditions, which are as simple as possible, the ribbed catalyst used for the modelling of the original electrode was replaced by a flat catalyst plate. The titanium plate was cooled from the back side to remove the reaction heat. It was covered by a 2 µm thick platinum layer.

2. Gas fraction distribution

As reported in [3], the axial gas fraction profiles measured in the H_2O_2 cells are divided into three characteristic areas, Fig. 3:

(I) the region of bubble flow, which is more and more displaced by foam with increasing current density. Finally it occurs only at the bottom. In this region the gas fraction is less than 60 %,

(II) the region of spherical foam with gas fractions of 60 % to 70 %, remaining nearly constant with increasing superficial gas velocity and

(III) the region of transition from spherical to cell foam with a gas fraction higher than 70% forming at the top.

The gas fraction profile perpendicular to the catalyst was measured by gamma densitometry in several vertical positions of the 0.16 m² H_2O_2 cell with the plate catalyst. At first, the results were checked against the gas fractions measured by the differential pressure method. After averaging the gas fraction profile in the horizontal direction, the results of both methods are in good agreement (see Fig. 3).

In Fig. 4 the results of a test run at a gas production rate corresponding to a current density in the original cell of 4.7 kA/m² are shown. A 6 mm thick boundary layer of the gas fraction was found. At a small distance from the catalyst the gas fraction profile takes a maximum which moves away from the catalyst as the gas fraction in the bulk increases. In the bulk, the gas fraction is surprisingly uniform. The difference between the gas fraction at the maximum and in the bulk is 6-8 % in the region of bubble flow and about 12 % in the spherical foam region. This difference is acting as a driving force for liquid circulation due to hydrostatic pressure gradients.

The measuring results support the theoretical gas fraction profiles of Matsuura [5] qualitatively, while the theory is not capable of providing the increase of the gas fraction in the

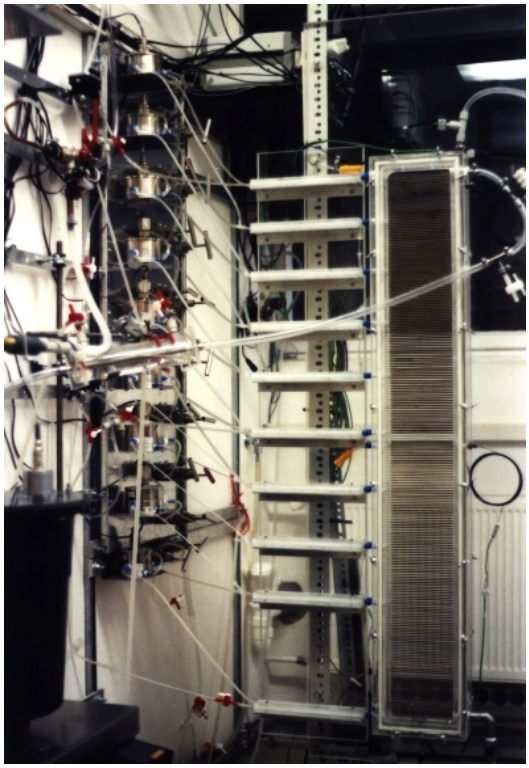

Fig. 2: 0.16 m² H_2O_2 cell

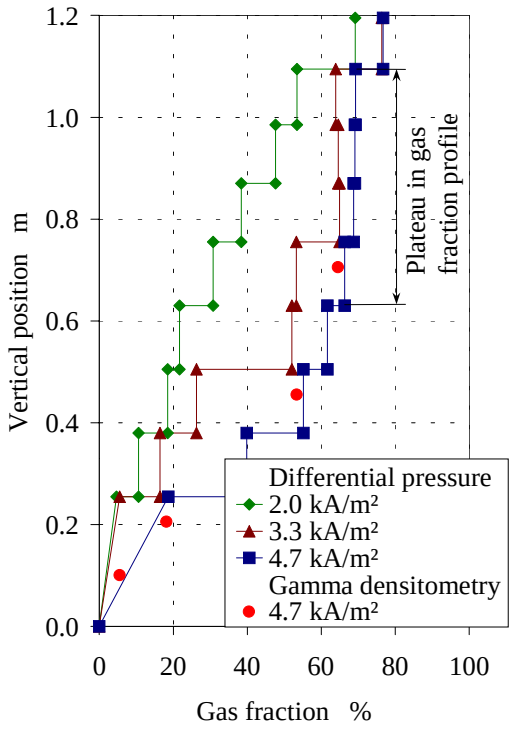

Fig. 3: Axial gas fraction profiles in the 0.16 m² H_2O_2 cell with plate catalyst

bulk due to the assumed infinite electrolyte extension perpendicular to the electrode. The assumption of a maximum gas fraction at the electrode surface, proposed by Dahlkild [6] was not confirmed.

3. Profiles of gas phase velocity

Profiles of the gas phase velocity were measured by LDA technique at the bottom of the 0.16 m² H_2O_2 cell, Fig 5. Similar to the gas fraction, the gas velocity profiles show a maximum at a distance of a few millimetres from the catalyst. Furthermore, distinct riser and downcomer zones exist. However, the thickness of the boundary layer is different for gas fraction and velocity: The gas fraction layer (app. 6 mm) is narrower than the velocity layer (app. 10 mm). Looking to the evolution of the velocity profiles with increasing height, the riser zone has to be divided in two regions: The peak region, where the velocity decreases with growing height, and the slope region between the peak and the downflow area, where the gas fraction increases. In total, the riser zone is widening in the upward direction. In the theoretical models of Matsuura [5] and Dahlkild [6] the gas velocity always increases with growing height, what is in contradiction to the experimental observations in the peak region.

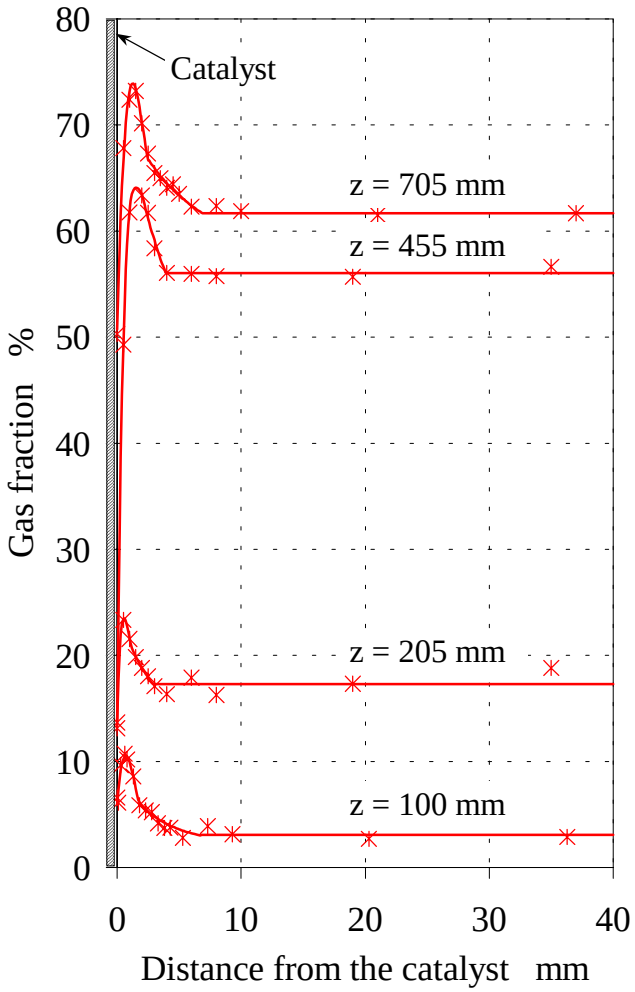

Fig. 4: Gas fraction profiles perpendicular to the plate catalyst at 4.7 kA/m²

An attempt to explanation can be made as follows: In analogy to the free thermal convection at a heated vertical plate the transition from the laminar to a turbulent boundary layer occurs at a Gr·Pr ≈ 10^8 – 10^9. Here, $Gr = g \cdot z^3 \cdot (\Delta\rho / \rho) \cdot (1/\nu^2)$, where the relative density decrease can be approximated as $\Delta\rho/\rho \cong \varepsilon_{max} - \varepsilon_{bulk}$. The Prandtl number must be modified to put into relation the viscosity to the diffusion of gas bubbles. For a first estimate, it was assumed that Pr ≅ 1, i.e. that bubble diffusion and momentum transport have the same order of magnitude. Recalculating the critical height, we get that the transition between laminar and turbulent boundary layers take place at a height of about 0.1 m. In this transition region, the turbulent viscosity increases significantly with growing height. At the same time, the shear stress, which is in equilibrium with the buoyancy of the bubbles, remains almost at the same level. This explains the decrease of the peak velocity with growing height in Fig. 5. The thickness of the boundary layer tends to grow, which is caused by the intensification of the momentum transport in the transition region. Neither the model of Matsuura [5] nor that of Dahlkild [6] consider a transition. The model of Matsuura is based on the Prandtl mixing length theory for a

turbulent flow, while Dahlkild solved the laminar case. In these both cases the velocity must always increase with growing height.

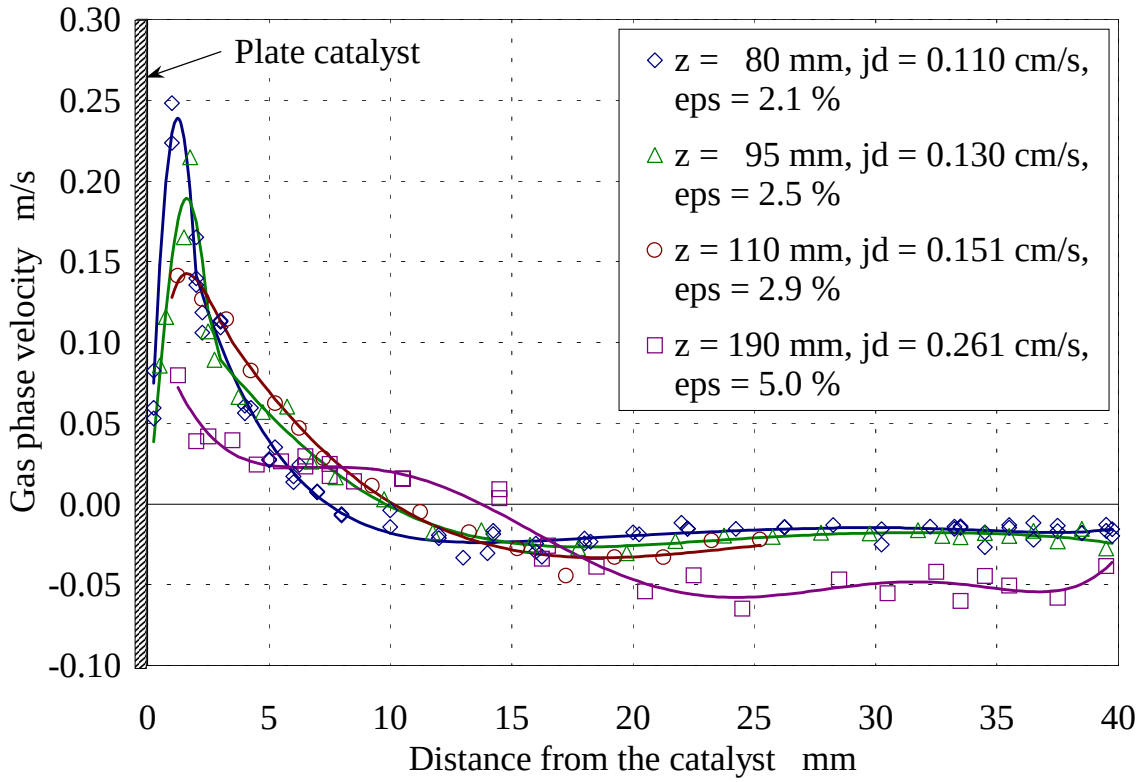

Fig. 5: Gas velocity profiles in the 0.16 m² H_2O_2 cell with plate catalyst at 2 kA/m²

In the downcomer, the gas phase velocity remains nearly constant. Since the gas fraction is also constant in this part of the cell, one can deduce that the bubble size distribution must be the same over the depth of the downcomer zone at a given vertical position.

4. Bubble size distributions

Bubble size distributions were measured at an elevation of 80 mm above the bottom of the cell. Unfortunately, the PDPA did not work at any higher position, because there the fluid is not transparent enough. The results are shown in Fig. 6 and 7. The measurements inside the riser region were carried out at four distances from the catalyst (1 – 3.5 mm) and have delivered almost the same bubble size distributions, while between riser and downcomer region significant differences were found. In comparison to the riser, the bubbles in the downcomer are larger approximately by a factor of two.

For the measured bubble size distributions, the bubble rise velocity is in the range of 2.6 mm/s in the riser and 5.3 mm/s in the downcomer. In comparison to the gas velocities given in Fig. 5 the bubble rise is only a minor contribution to the gas transport, i.e. the gas transport is dominated by the liquid circulation at the bottom of the cell.

5. Conclusions

The experiments at a model of the alkali chloride electrolysis cell have shown that the appearance of foam is an important factor in the hydrodynamic cell behaviour. Axial gas fraction distributions measured by the differential pressure method were completed by gamma-densitometry, which allowed to characterise the gas fraction profiles perpendicular to the catalyst (model electrode). These two measuring techniques are applicable over the entire cell height. To study the bubble velocity and the bubble size distributions, LDA/PDPA was used. Results could only be obtained near the cell bottom.

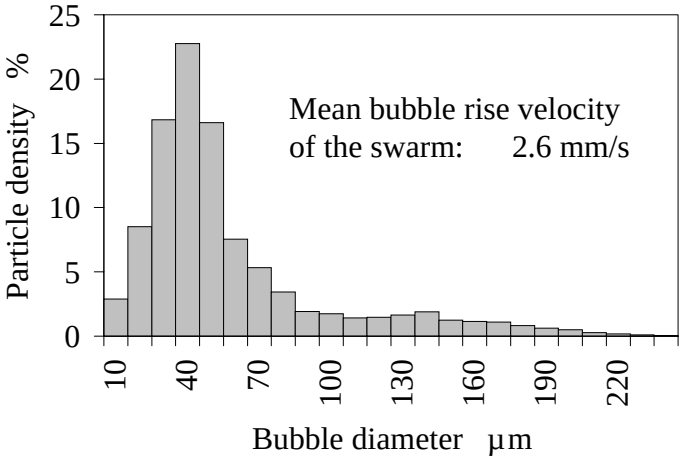

Fig. 6: Bubble size distribution at 80 mm above the cell bottom and 1-3.5 mm from the plate catalyst (riser)

It was found that an increase of the cell performance leads to a growing layer of spherical foam with an almost constant gas fraction of about 60 %-70 %. At the top of the spherical foam a region of transition to cell foam was observed. The maximum gas fraction was 84 %. A gas fraction boundary layer was found both in the bubble flow and in the region of spherical foam.

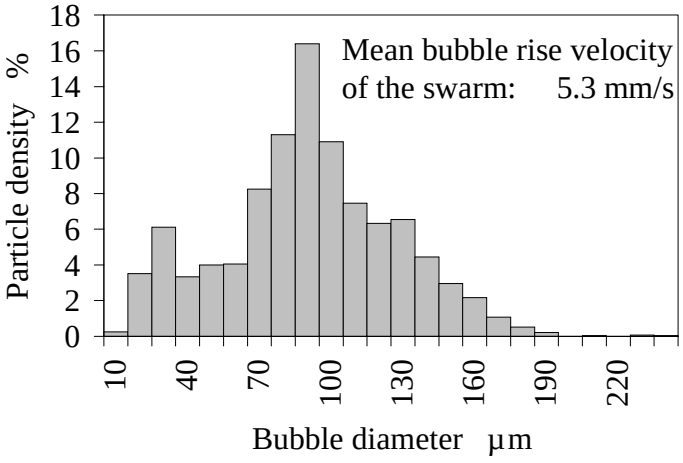

Fig. 7: Bubble size distribution at 80 mm above the cell bottom and 25 mm from the plate catalyst (downcomer)

The LDA measurements have shown the circulation of the fluid and the boundary layer near the catalyst (model electrode), which is the dominating factor of the gas transport at the bottom of cell. The velocity profiles indicate that the measurements were performed in the transition region between laminar and turbulent boundary layer. Future theoretical models must include this transition region. In the region of spherical foam, the bubble coalescence leads to the increase of the bubble rise velocity compensating the growing superficial gas velocity what keeps the gas fraction at a constant level.

Nomenclature

d_B	[m]	mean bubble diameter
eps	[%]	gas fraction
g	[m/s²]	gravity constant
Gr	[-]	GRASHOF number
j_d	[m/s]	superficial gas velocity
Pr	[-]	PRANDTL number
z	[m]	z-direction referring to cell height
ε_{max}	[%]	maximum gas fraction
ε_{bulk}	[%]	gas fraction in the bulk
ν	[m²/s]	cinematic viscosity
ρ	[kg/m²]	density

LDA	Laser Doppler Anemometer
PDPA	Phase Doppler Particle Analyser

References

[1] D. Bergner, Entwicklungsstand der Alkalichlorid-Elektrolyse, Teil 2: Elektrochemische Größen, wirtschaftliche Fragen, Chem.-Ing.-Tech. 66 (1994) Nr. 8, S. 1026-1033

[2] D. Bergner, Gasblasengehalt in Alkalichlorid-Membranzellen, Chem.-Ing.-Tech. 62 (1990). Nr. 5, S. 409-411

[3] C. Schneider: Fluid mechanics of electrolytic cells, Forschungszentrum Rossendorf, Institute for Safety Research, Annual Report 1997, FZR-238, October 1998, pp. 42-47.

[4] C. Schneider: Fluid mechanics of electrolytic cells, 2nd intern. symposium „Two-Phase Flow Modelling and Experimentation“, Pisa, 23-26 May 1999, proceedings vol. 2, pp. 1085-1992.

[5] A. Matsuura, H. Nakamura, S. Hiraoka, Y. Tada, Y. Kato and K.S. Tae: Gas-liquid turbulent two phase flow along vertical flat plate with gas evolution, J. Chem. Eng. of Japan, 28 (1995) 3, pp. 250-256

[6] A. Dahlkild, Hydrodynamic diffusion models of small bubbles produced at a vertical electrode under laminar flow conditions, 3rd Int. Conf. On Transfer Phenomena in MHD and Electroconducting Flows, Aussois, France, Sept. 1997, S 22-26.

MEASUREMENT TECHNIQUES TO DETERMINE LOCAL QUANTITIES IN LIQUID METAL FLOWS

Sven Eckert, Willy Witke, Gunter Gerbeth

1. Introduction

In the last few decades magnetohydrodynamic (MHD) effects have attracted growing interest because of its potential impact on numerous industrial technologies such as metallurgy, crystal growth, electron or laser beam melting/evaporation of surfaces, etc.. In processes involving electrically conducting liquids, the application of an external magnetic field offers efficient opportunities for a contactless flow control and fluid handling.

However, for a well-aimed optimisation of the flow structure local information about flow quantities like velocity, pressure, temperature, concentration or void fraction are necessary. The techniques of local and instantaneous measurements in liquid metals are known to be much more difficult than in classical fluids like water or air. Whatever diagnostic method is used, two categories of problems have to be solved: those due to the nature of the fluid (opaque, hot, chemical aggressive) and, in addition, due to the presence of electromagnetic fields. Almost all conventional measuring techniques used for ordinary flows, for instance LDA or hot-wire anemometry, totally fail in liquid metal MHD flows or their applicability is strongly limited. As a consequence, no commercial measuring systems are available.

During the last years activities of the MHD department are focussed to develop and to qualify techniques to measure the velocity of the liquid metal and two-phase flow characteristics such as void fraction, bubble velocity and bubble size, respectively. In liquid metal model experiments local sensors as well as integral methods have been tested and applied.

2. Measurements of the liquid metal velocity

2.1 Potential-difference Probe

The potential-difference probe (sometimes also called conductance anemometer) can already be considered as standard technique in MHD experiments (see Branover [1]). The problem to be solved here was the development of special sensors being capable of working reliably in liquid sodium.

If a flow is exposed to a sufficiently strong magnetic field the measured electric potential drop $\Delta\varphi$ between the electrodes is essentially determined by the $\vec{u}\times\vec{B}$ term [2] (see figure 1), resulting in a linear dependance on the flow velocity. The following advantages promote the use of such kind of probes:

- The geometry of the probe is very simple (two isolated electrodes). Therefore, a good minimisation of the sensor size is possible to reduce the flow disturbances caused by the probe itself.

- The sensor is reliable and robust in liquid sodium at temperatures up to 320°C.
- The relation between the voltage signal and the fluid velocity is linear for a wide parameter range.
- The sensor responds promptly and guarantees the suitability to measure the turbulent velocity fluctuations.

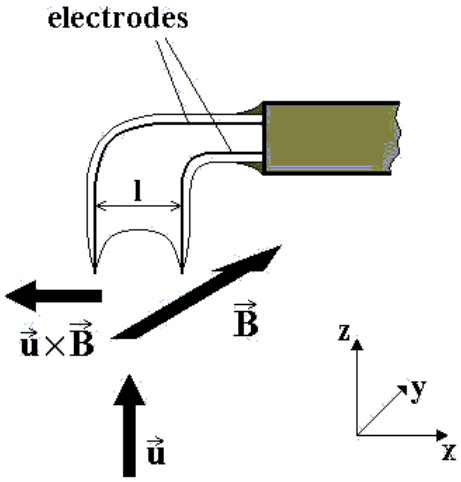

Fig. 1: Principle of the potential probe

However, the use of the potential probe is combined with some serious limitations and difficulties. The measuring principle requires the application of a steady magnetic field, whereas the velocity component parallel to magnetic field lines cannot be determined. To measure the velocity fluctuations one has to deal with very small signals (some μV), which can be disturbed by a significant level of electric noise arising from components of the experimental facility (electromagnetic pump, heating elements). Moreover, the linear relation between output signal and velocity is not valid if the flows is bounded by highly conducting walls or influenced by changes of the magnetic field, the cross sectional area or the wall conductance [2].

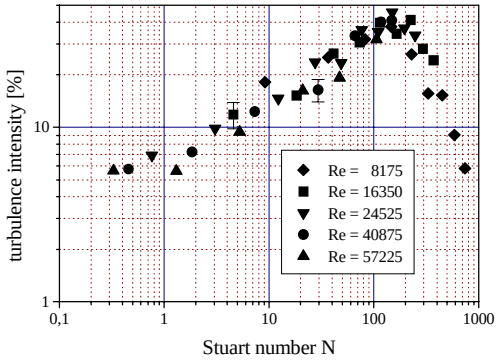

Fig. 2: Turbulence intensity as a function of Stuart number N

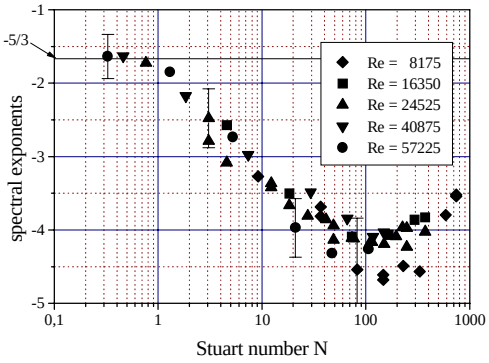

Fig. 3: Slope of the spectral energy versus Stuart number N

Potential probes have been employed to characterise the local, turbulent properties of liquid sodium channel flows by the determination of the turbulence intensities and the power spectra [2]. Some interesting effects have been revealed, for instance, the increase of the turbulence intensity with increasing Stuart number $N=\frac{\sigma B^2 L}{\rho u}$ (see Figure 2) or the steeper slope of the spectral energy in the inertial range with increasing Stuart number starting from a $k^{-5/3}$-behaviour for $N \leq 1$ and reaching a k^{-4} -scaling at $N \approx 100$, which becomes obvious in Fig. 3.

2.2 Mechano-optical probe

A new measuring system based on a mechano-optical principle has been developed to determine local flow velocities. Our intention was to meet the following requirements:

- The sensor should be able to work in opaque fluids at high temperatures.
- The resolution should be sufficient to measure also velocities below 0.1 m/s.
- The system should be characterised by good spatial resolution.
- Flow disturbances caused by the sensor should be negligible.
- An influence of external electromagnetic fields or electric noise on the signal should be avoided.

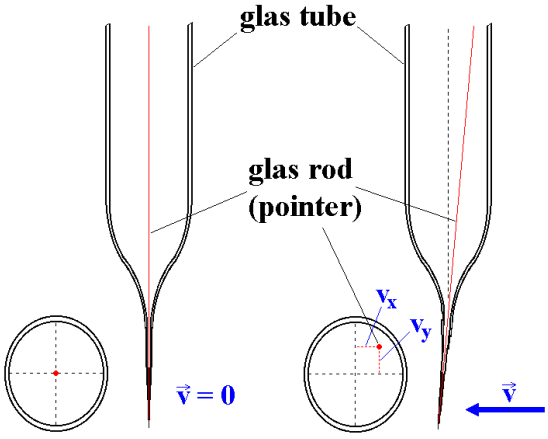

Fig. 4: Measuring principle of the mechano-optical sensor

The sensitive part of the probe is a glass tube formed to a thin conical tip which is in direct contact to the fluid (see figure 4). A small glass rod, the so-called pointer, is positioned inside this glass tube and connected with the sensor tip only at the front point. The interaction with the flow causes a deformation of the sensor tip resulting in a displacement of the pointer. The flow velocity can be derived from this observed displacement. A detailed description of the measuring principle and the equipment is given by Eckert et al. [3]. The authors also modelled the drag force acting on the sensor in the fluid. From those estimates the rod displacement shows a parabolic dependence on the flow velocity. Such a qualitative behaviour has been confirmed by first experimental investigations, where the sensors have been calibrated in a circular rotating channel.
The sensors have been tested in water and InGaSn at room temperature as well as in SnPb and PbBi at temperatures up to 300 °C. The suitability of the sensor in this temperature range was

demonstrated. A further increase of the temperature can be questionable, because the elastic module of the borosilicate glass becomes then a function of the temperature. The transformation temperature of this type of glass is approximately 650 °C. To use the measuring system at higher temperatures, for instance in aluminium at about 700 °C, the probe tip has to be manufactured from different material. A possible alternative is quartz glass with a transformation temperature above 1200 °C. The adaptation of the existing technology for the sensor production to quartz glass is the present subject of investigation.

The measuring system has already been used to determine the local flow structures in real experimental flows. In our lab swirling flows of InGaSn alloy in a circular box created by the application of time-variable (travelling and/or rotating) magnetic fields have been investigated. The interest is focussed on geometry and parameters relevant for crystal growth technologies. Measured profiles of the azimuthal velocity obtained at different frequencies and field amplitudes are displayed in Figure 5. In case of low frequency the increase of the velocity starting from the centre to the boundary seems to be linear. This indicates that the flow structure of the melt can be associated with a solid body rotation. The application of a magnetic field rotating with a significantly higher frequency results in an evident variation of the profiles. The enhancement of the velocity maximum near the boundary corresponds to the above-mentioned skin effect of the concentration of the field action in the boundary region.

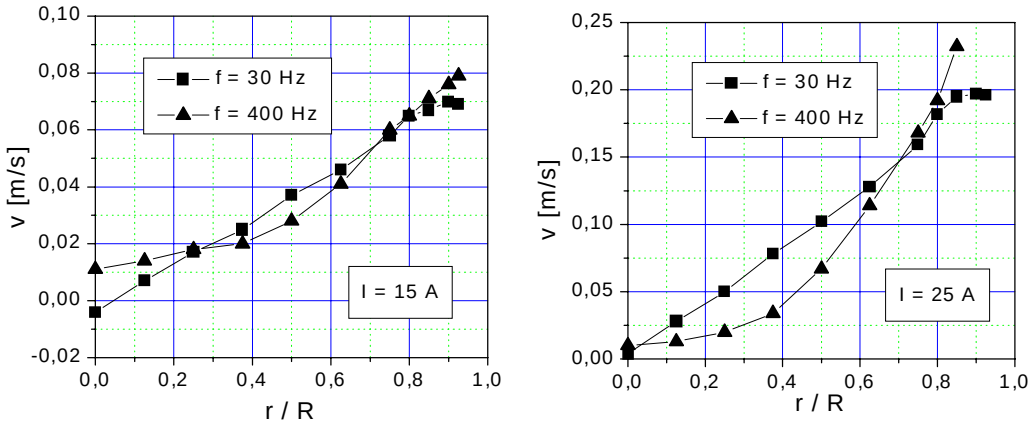

Fig. 5: Radial profiles of the azimuthal velocity in a cylindrical flow driven by a rotating magnetic field

Another application will be the channel flow of liquid sodium at the experimental sodium loop of FZR. It is planned to measure the velocity profiles in the channel cross section with and without transverse magnetic field. The obtained results shall be compared with the existing data of the potential probe. Moreover, first measurements have been confirmed in co-operation with industrial partners.

2.3 Ultrasound-Doppler method

The instantaneous velocity profile which is one of the most fundamental quantities in fluid flow phenomena can be obtained by the Ultrasound-Doppler technique [4]. Main advantages are the ability to investigate flows of opaque liquids in a non-intrusive way and to deliver complete velocity profiles in real-time. The principle of this method is to utilise the pulsed

echo technique of ultrasound and to detect the Doppler shift of the ultrasound wave reflected from moving particles suspended in the fluid.

The general feasibility of velocity profile measurements has already be shown in low temperature liquid metals like mercury [5] and gallium [6]. However, the technology reveals severe limitations regarding the practicability of measurements at high temperatures and the useable velocity range. Therefore, activities have been started to develop this technique for high temperature liquid metal applications. First tests have already been performed at the sodium facility of FZR. At the present status the following main problems have been identified:

- Limitation of the temperature range of the ultrasonic transducer: The transducer can be used up to a maximum working temperature of 150°C. Moreover, the efficiency at temperatures close to this maximum is low.
- Coupling of the ultrasound into the fluid: Due to the high temperatures and the chemical properties of liquid sodium the transducer was installed at the outer channel wall. Therefore, an excellent wetting of the liquid metal at the inner surface of the wall is required to get a small acoustic impedance at the interface steel - liquid metal.
- Availability of tracers in the flow: The sensitivity and accuracy of the method depends on the occurrence of flow tracers reflecting the ultrasonic beam. If the amount of naturally existing impurities is not high enough, additional scattering particles have to be added to the flow.

3. Measurements of two-phase flow parameters

3.1 Resistance probes

The single-wire resistance probes are local sensors to measure the local void fraction well-known from the applications in ordinary two-phase flows (see Jones & Delhaye [7], Prasser [8]). There is an electrically conducting tip (Cr/Ni wire, ∅ 0.1 mm) in direct contact with the liquid metal. The probe is supplied with an alternating current (1-10 kHz), which results in an electric current flowing from the probe tip to the cladding pipe acting as the other electrode. The gas contact at the sensitive wire is detected by an interruption of the current. Due to the huge differences in the electrical conductivity between the gas and the liquid metal we obtain very sharp signals easy to evaluate by a threshold method.

An extensive survey about a number of two-phase flow measurements carried out by several kinds of local sensors characterised by different tip sizes and probe shapes is provided by Cartellier & Achard [9]. As a rough estimation it may be generalised, that bubbles with a minimal size being about 10 times higher as compared to the probe wire can be detected by the sensor. In our experiments single-wire conductance probes with wire diameters of 25 μm and 100 μm have been used.

Double-wire resistance probes have been used to measure gas velocity and bubble size by detecting the time delay of the bubble contact between two wires arranged closely together in flow direction. But, such a sensor configuration enhances seriously the tip size of the probe. In fact, reliable measurements of bubble diameters less than 1 mm by means of local conductance probes have to be considered as doubtful. Despite of measuring errors of bubble

velocities and chord lengths up to about 20 % for bubble diameters of a few mm also measurements by means of double-wire probes provide useful information about the structure of the two-phase flow.

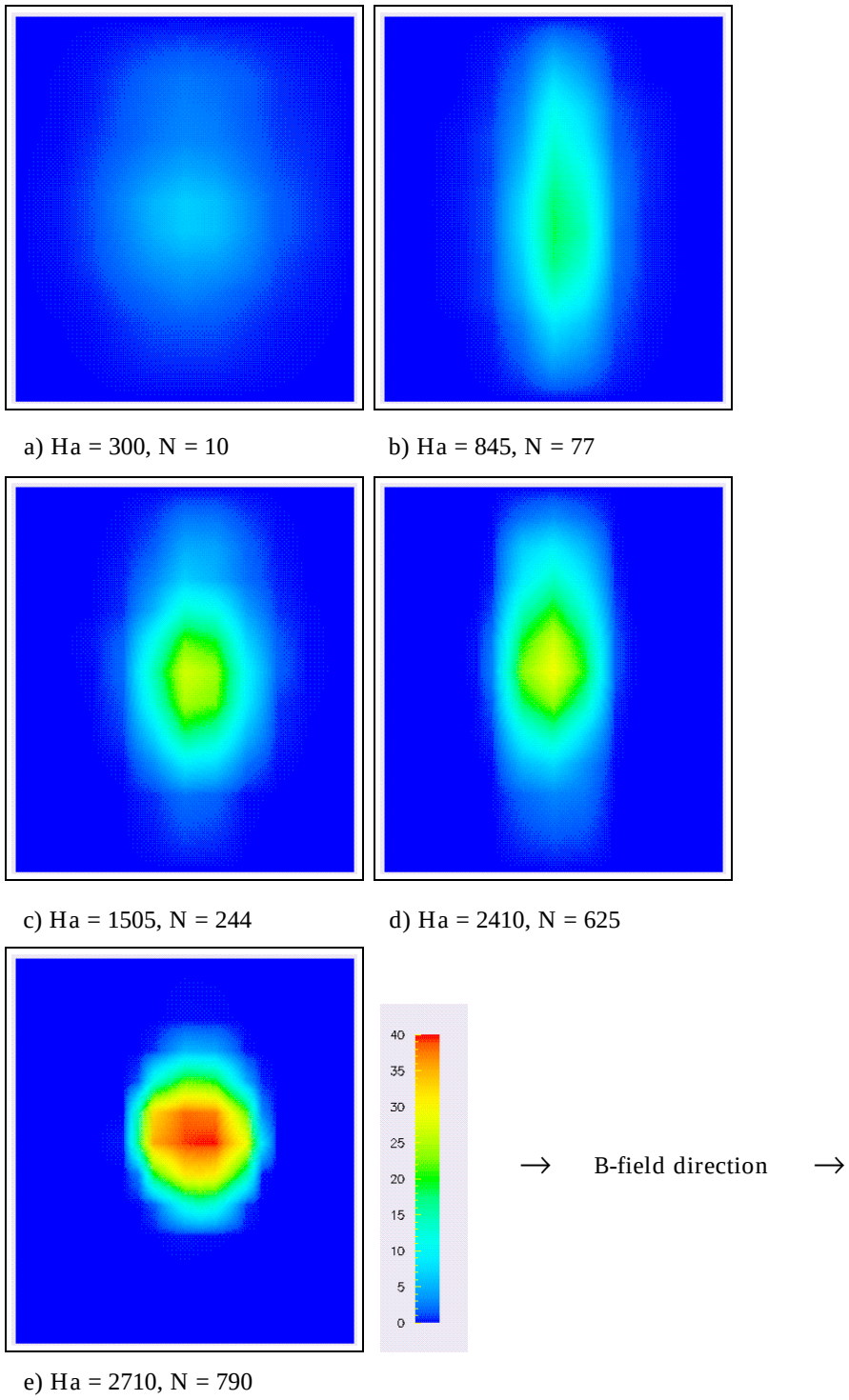

Fig. 6: Local distributions of the void fraction α [%] in a turbulent sodium channel flow exposed to a transverse magnetic field (Re = 9300)

Figure 6 shows some representative isoplots of the void fraction distribution in the cross sectional area of a MHD channel flow obtained at different Reynolds numbers and different

values of the magnetic field by Eckert et al. [10]. In the case of a transverse field direction an anisotropic distribution is observed indicating the existence of quasi-two-dimensional vortices as typical for turbulent MHD flows.

3.2 X-ray measurements

A direct observation of gas bubbles in non-transparent liquid metals is impossible by optical means. Despite of the substantial technical effort, the use of high energy radiation allows also investigations of liquid metal two-phase flows. X-ray measurements can be used to directly observe gas bubbles rising in liquid metals. However, due to the high attenuation in the liquid the experiment is restricted to narrow flow domains. The thickness of the fluid, which can be screened by X-ray, depends of the atomic number of the liquid metal.

Experiments with mercury and InGaSn, respectively, have been performed at the X-ray facility of the FZ Jülich. A 450kV industrial X-ray tube was employed for the inspection of liquid metal contained in rectangular cell made from Perspex. A sketch of the experimental configuration is depicted in Figure 7. For a detailed description of the experimental technique the reader is referred to Stechemesser et al. [11]. Flow sequences were recorded in mercury layers with a depth of 6 mm at 450 kV and 10 mm for InGaSn at 147 kV. Experiments with InGaSn would allow an enlargement of the fluid domain, whereas for mercury the limit has been reached. The resolution of the X-ray screening technique is restricted to a bubble diameter of about 1 mm. The decrease of the X-ray absorption inside the liquid volume due to smaller gas bubbles is not sufficient to produce a corresponding image with a reliable contrast.

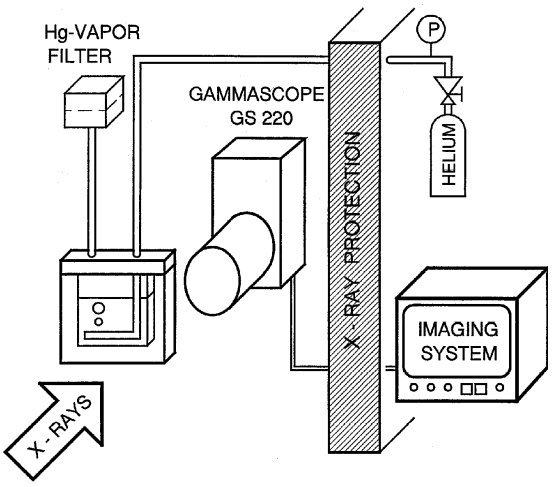

Fig. 7: Experimental configuration of the X-ray screening technique

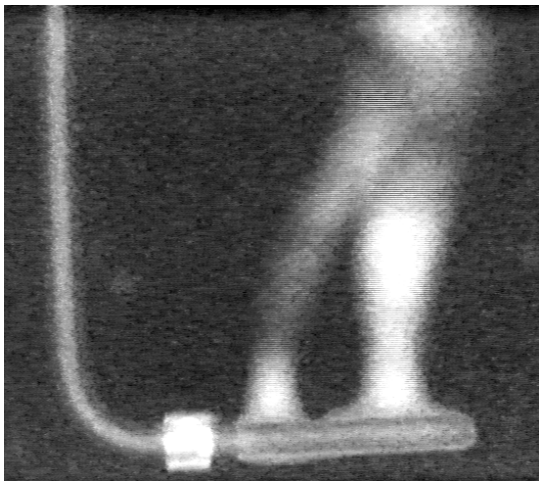

Fig. 8: Gas injection through a nonwetted sintered metal tube into mercury (observed by X-ray technique)

The features of a gas injection into mercury by means of miscellaneous gas injectors for the case, if the surface of the injector is not wetted by the liquid metal, has been demonstrated [12]. Among other types of gas injectors a bent stainless steel tube has been used completed with a sintered metal body at the end having a mean pore diameter of 4 μm. The gas flow can escape from the injector only at the upper surface. Nevertheless, it becomes obvious in Figure

8 that instead of a bubble formation directly at the end of the pores, a gas layer is growing around the injector until the buoyancy force will be high enough to promote the release of particular, large bubbles. However, in this situation the size of the generated bubbles does not depend on the typical diameter of the injection pores.

References

[1] H. Branover (1978), Magnetohydrodynamic Flow in Ducts, New York, Toronto, John Wiley & Sons

[2] S. Eckert (1998), Experimentelle Untersuchung turbulenter Flüssigmetall- und Flüssigmetall-Gas-Strömungen in einem äußeren Magnetfeld, Rossendorf, Report FZR-219

[3] S. Eckert, W. Witke and G. Gerbeth (1999), A new mechano-optical technique to measure local velocities in opaque fluids, submitted to: Flow Measurement and Instrumentation

[4] Y. Takeda (1991), Development of an ultrasound velocity profile monitor, Nuclear Engineering and Design, 126, 277

[5] Y. Takeda, H. Kikura and G. Bauer (1998), Flow Measurement in a SINQ Mockup Target using Mercury, Proc. of ASME FED Summer Meeting, Washington D.C.

[6] P. Cardin, H.-C. Nataf, B. Pascal and J. C. Attiach (1996), Velocity measurements in a vortex of liquid Gallium, 1st Int. Symposium on Ultrasound Doppler Methods for Fluid Mechanics and Fluid Engineering, Villigen PSI

[7] O. C. Jones and J.-M. Delhaye (1976), Transient and statistical measurement techniques for two-phase flows: A critical review, J. Fluid Mech.,147, 89

[8] H. M. Prasser (1997), Leitfähigkeitssensoren für die Bestimmung von Parametern in einer Zweiphasenströmung, Workshop "Meßtechnik für stationäre und transiente Mehrphasenströmungen", Rossendorf

[9] A. Cartellier and J. L. Achard (1991), Local phase detection probes in fluid/fluid two-phase flows, Rev. Sci. Instrum., 62, 279

[10] S. Eckert, G. Gerbeth and O. Lielausis (1998), The behaviour of gas bubbles in a turbulent liquid metal MHD flow - Part I: Dispersion in quasi-two-dimensional MHD turbulence, submitted to: Int. J. Multiphase Flow

[11] H. Stechemesser, G. Schröder, Ch. Sauerwein and W. Nuding (1998), Gas injection experiments in static Hg: Real-time observations with X-rays, ESS report 98-68-T

[12] S. Eckert, G. Gerbeth, B. Guttek and H. Stechemesser (1998), Bubble formation in heavy liquid metals: Evaluation of conventional gas injection methods with respect to a suitability under ESS relevant conditions, ESS Report 98-72-T

The projects summarised in this report are funded by Deutsche Forschungsgemeinschaft under grant No. Ge 682/3-4 and in frame of the DFG-Innovationskolleg Magnetofluiddynamik.

RESULTS OF THE FIRST RIGA DYNAMO EXPERIMENT

Frank Stefani, Gunter Gerbeth and Thomas Gundrum

1. Introduction

The investigation of homogeneous fluid dynamos where a magnetic field $\vec{B}$ is created solely out of the kinetic energy of some fluid flow $\vec{v}$ is crucial for the understanding of cosmic magnetic fields. During the last decades, enormous progress has been made concerning the analytical and numerical treatment of the induction equation (which directly results from Maxwell's equations and Ohm's law)

$$\frac{\partial \vec{B}}{\partial t} = curl\left(\vec{v} \times \vec{B}\right) + \frac{1}{\mu_0 \sigma} \Delta \vec{B} \qquad (1)$$

for kinematic dynamo models (with conductivity σ and a pre-given flow velocity $\vec{v}$) and, partly, of the coupled system of induction equation and Navier-Stokes equations including the back-reaction of the Lorentz forces on the flow velocity.

Only recently, expensive numerical simulations of the earth dynamo [1] have attracted much attention as they showed some realistic features of the earth magnetic field, e.g., a reasonable relation of magnetic and kinetic energy, a quite realistic spectrum of the mean-square field intensity and, most spectacular, the possibility of magnetic field polarity transitions. It should be noticed, however, that in those numerical simulation some numerical trickery (use of hyperdiffusivity etc.) was necessary and that the incorporation of more realistic parameters (especially, of a much smaller magnetic Prandtl number) would even increase the numerical costs dramatically.

As for experiments on dynamo action, at present there are activities at several places in the world (for an overview, see [2], and for a recent additional approach [3]). These experimental approaches differ widely in the vessel geometry, the flow topology and the technical realization of the forcing. All experimental settings are rooted in some well-studied theoretical dynamo models, and the main purpose of those experiments is to show magnetic field self-excitation at all rather than to establish a realistic experimental modelling of, say, the earth dynamo (whatever some public statements on the „ultimate" goals of those dynamo experiments are suggesting). Apart from the experimental verification of self-excitation, present dynamo experiments will at best provide some insight into the non-linear regime and in MHD-turbulence. Only future work can show whether such interesting effects like mode-switching or polarity reversals of the magnetic field can be studied in liquid metal experiments.

This report is intended to give a short overview about the results of the first experiment which was carried out at the Riga dynamo facility during November 6-11, 1999. Concerning the long history of planning and optimizing this experiment we refer to [4,5] and for some additional numerical predictions to the report [6] in order to avoid any undue redundancy.

2. The Riga dynamo facility

Tracing back in its main idea to a paper of Ponomarenko [7], the Riga dynamo experiment strives to show magnetic field self-excitation in a very simple flow topology. In a central spiral flow (with a velocity up to 15 m/s) the magnetic field is amplified by stretching field lines. A coaxial back-flow is responsible for positive feed-back. A surrounding region with sodium at rest decreases the Ohmic losses and thus yields to a lower critical value of the magnetic Reynolds number $Rm = \mu_0 \sigma L v$, where L and v are typical length and velocity scales of the flow. The whole facility with the motors, the propeller, the storage tanks and the positions of the magnetic field sensors is depicted schematically in Figure 1.

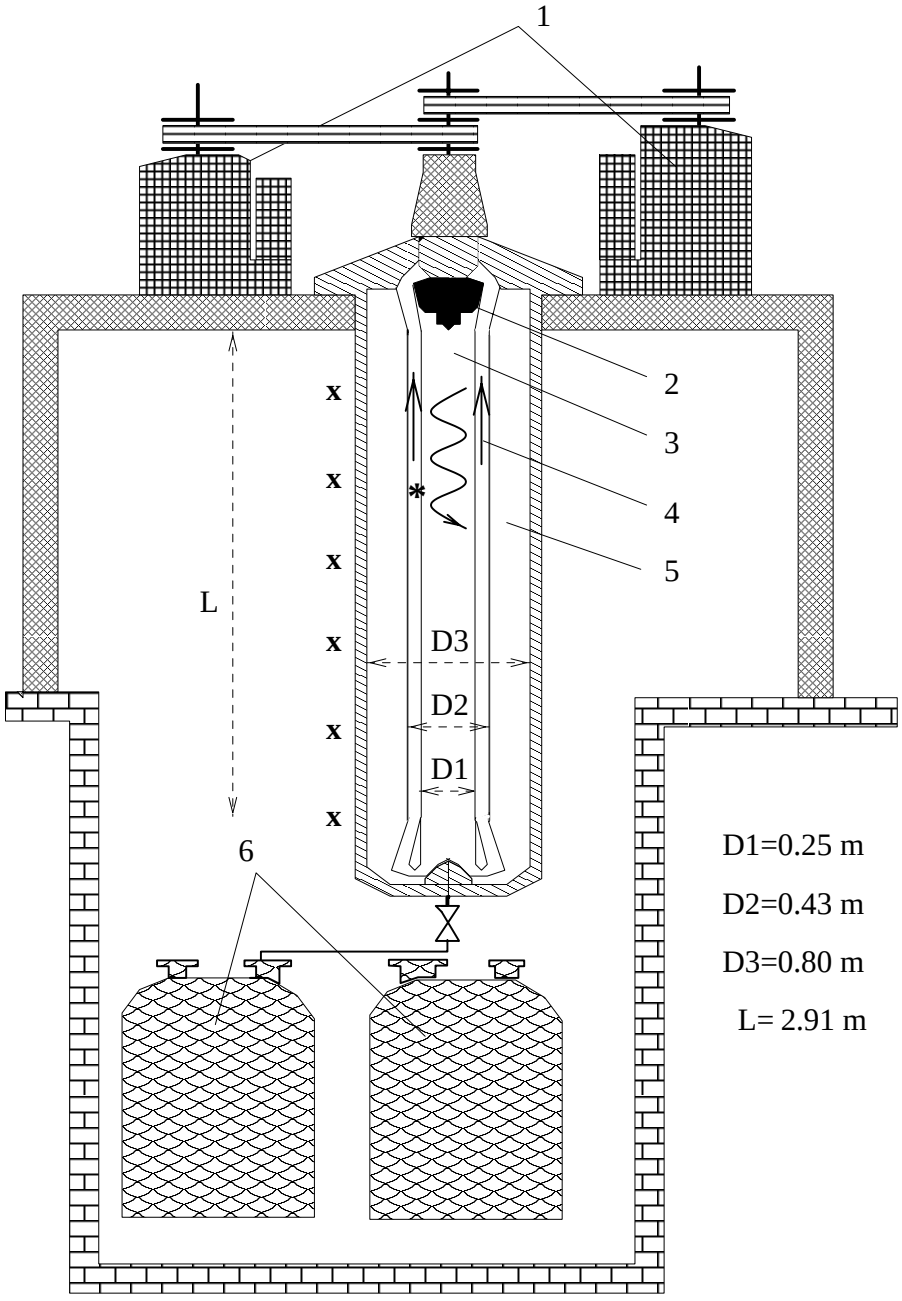

Fig. 1: The experiment: 1-Two motors (55 kW), 2-Propeller, 3-Spiral flow, 4-Back-flow, 5-Sodium at rest, 6-Sodium storage tanks, *-Flux-gate sensor, x-Six Hall sensors

Given the limited power resources, the main problem of the described experimental dynamo approach lies in the sensible dependence of the critical magnetic Reynolds number on the shape of the axial and the azimuthal velocity components. In a long iterative process of analytical and numerical velocity profile optimization, pump design (including the installation of guiding vanes in front and behind the propeller, which are not shown in Figure 1) and flow measurements the whole device had been tailored up to a point that self-excitation seemed to be reachable in a sodium experiment [5,6].

3. Results of the experiment

The experiment started with filling sodium from the tanks into the facility, heating it up to 300°C and letting it circulate slowly for more than a day in order to assure good electrical contact with the steel walls. In order to provide optimal conditions to reach the magnetic field self-excitation it was obvious that any Ohmic resistance between the stainless steel walls and the sodium should be avoided, and that a maximal electrical conductivity of the sodium is desirable. Since the electrical conductivity of sodium decreases with increasing temperature the main experiment was planned at the lower temperature limit of about 150°C where the electrical conductivity approaches $9.0 \cdot 10^6$ S/m. In the meantime, experiments at 250°C and 200°C (with lower conductivities) were carried out in order to collect data on the response of the dynamo on an applied magnetic field in the sub-critical (or close to the critical) regime. Unfortunately, during the experiment at about 205°C some technical problems with the seal of the rotating propeller shaft occurred resulting in the flow-out of a minor amount of sodium. The safety rules required to stop the experiment at this moment, and the most effective range of temperature around 150°C could not be reached.

Therefore, the following considerations will be restricted to the measurements at a sodium temperature around 205°C (depending slightly on the measurement position and the time). For this temperature (and the corresponding conductivity of $7.5 \cdot 10^6$ S/m) it was a priori not clear whether self-excitation could be achieved or not. Therefore, the main purpose of the measurements was to determine the response of the dynamo on an externally applied magnetic field which was produced by a 3-phase current with variable frequency in a specially designed helical coil wound around the dynamo module. For the magnetic field measurements two different concepts were followed. Close to the innermost wall where the magnetic field generation of the dynamo was expected to be strongest a high temperature flux-gate sensor was positioned. Outside the dynamo module, at a distance of 10 cm from the thermal isolation, 8 Hall sensors were located, 6 of them parallel to the dynamo axis at relative distances of 50 cm and two of them at additional angles. These Hall sensors were mainly devoted to determine the spatial structure of a possible self-generated field. For the sub-critical regime it was clear in advance that the information of those sensors could be only of limited use due to the dominance of the applied field over the amplified field outside the module.

For an excitation frequency of 1 Hz, Figure 2 shows the dependence of the inverse relation of the magnetic field measured at the inner flux-gate sensor to the current which was applied in the kick-field coils in dependence of the rotation rate of the propeller.

Between 500 and 1500 rpm a clear increase of the amplification can be observed. This part of the curve points to a crossing point with the abscissa at about 1700 rpm. Of course, a real crossing with the abscissa, e.g., an infinite amplification is impossible due to the expected

back-reaction of the magnetic field on the flow. Nevertheless it is interesting to note that the curve seems to be expelled from the abscissa above a rotation rate 1800 rpm. Later on, when comparing the results with the numerical predictions, we will see that this behaviour may have to do with passing the resonance point of the applied frequency with the eigenfrequency of the dynamo.

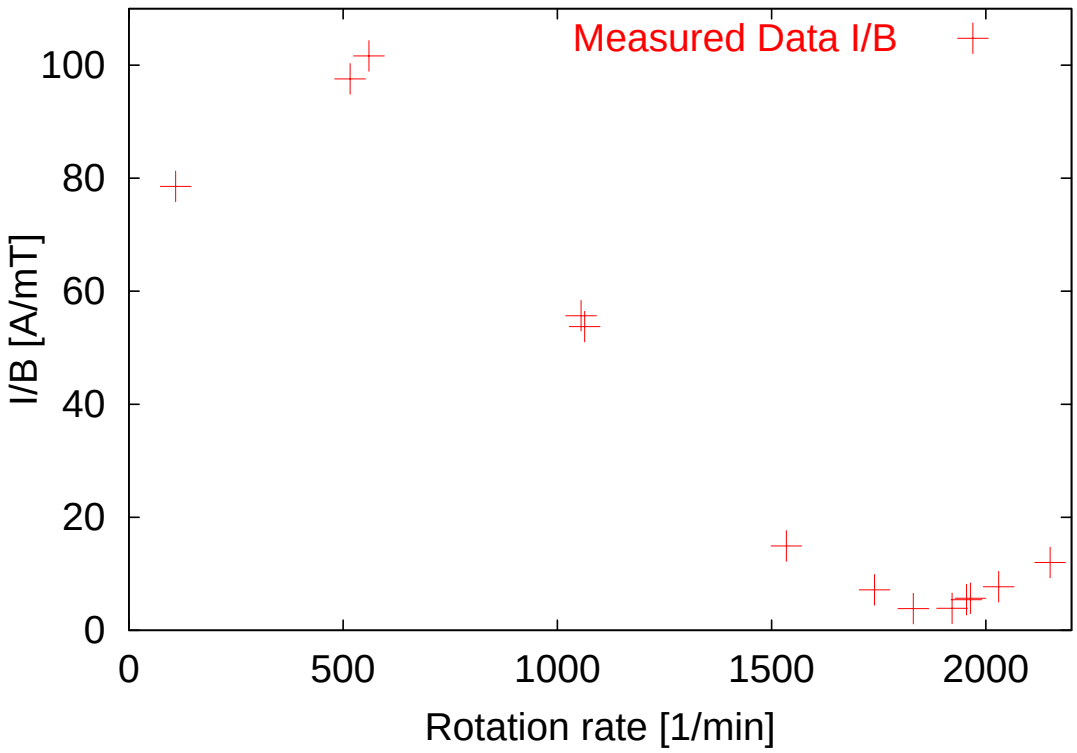

Fig. 2: Dependence of the magnetic field amplification on the propeller rotation rate for T=205°C and f= 1Hz.

It should be pointed out that all but the rightmost points in Figure 2 are calculated from nearly undisturbed sinusoidal magnetic field signals with the same 1 Hz frequency as the kick-field. The point at 2150 is, however, exceptional as it represents a clear superposition of two signals with different frequencies. At the inner sensor, this signal was recorded for a period of 15 seconds (starting 12 seconds after the rotation rate had achieved the maximum value). During this period, 1500 field measurements were carried out. These data are depicted with crosses in Figure 3a.

After a Fourier analysis of these data which showed two clear peaks around 1 Hz and 1.3 Hz, an additional non-linear fit was made using the ansatz

$$B(t) = A_1 \exp(p_1 t)\sin(2\pi\ f_1 + \phi_1) + A_2 \exp(p_2 t)\sin(2\pi\ f_2 + \phi_{21}) \qquad (2)$$

providing the following results for the unknown parameters (the errors are with respect to a 68.3 per cent confidence interval):

$A_1 = (0.476 \pm 0.004)$ mT	$A_2 = (0.133 \pm 0.001)$ mT
$p_1 = (-0.0012 \pm 0.0003)\,\mathrm{s}^{-1}$	$p_2 = (0.0315 \pm 0.0009)\ \mathrm{s}^{-1}$
$f_1 = (0.995 \pm 0.00005)\ \mathrm{s}^{-1}$	$f_2 = (1.326 \pm 0.00015)\ \mathrm{s}^{-1}$
$\phi_1 = -0.879 \pm 0.012$	$\phi_2 = 0.479 \pm 0.009$

Most remarkable is the slightly positive value of p_2 indicating an additional mode with an exponential increase in time. The curve (2) is also depicted in Figure 3a and evidently it fits extremely well into the data. Figure 3b shows the decomposition of (2) into the two signals with different frequencies.

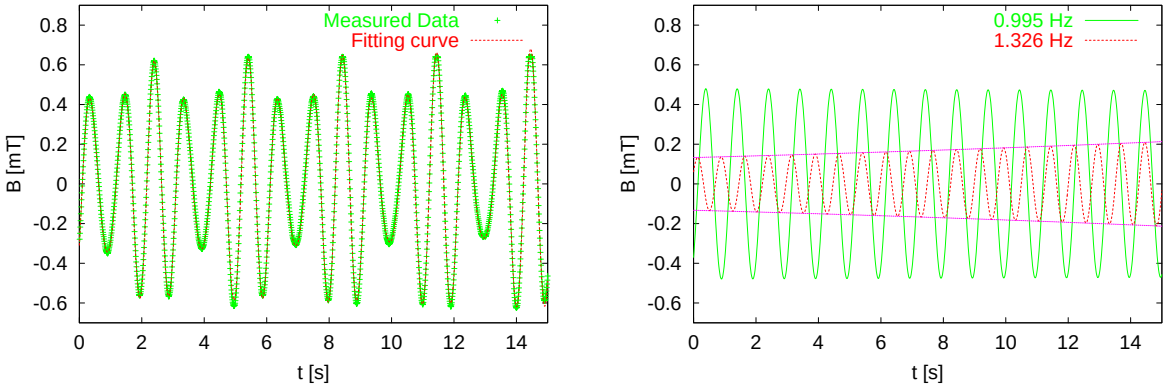

(a) (b)

Fig. 3: Measured magnetic field at the highest rotation rate of 2150 rpm. Data and fitting curve (a). Decomposition of the fitting curve into two signals with different frequencies.

Unfortunately, during the experiment an on-line visualization of the magnetic field signal was only possible for two of the eight Hall sensors outside but not for the inner sensor. For that reason the signal in Figure 3a was identified only in the post-processing of the data. Of course, the identification of the self-exciting magnetic field mode with 1.3 Hz *without* any additional kick-field would have been more convincing. But at the highest rotation rate of 2150 rpm the kick-field current was not switched off.

This was only done when the rotation rate had decreased again to 1980 rpm. After switching off the current the magnetic field decayed slowly. Figure 4 shows the corresponding signals for the six outer Hall sensors (the signal at the inner sensor was very similar). The signals have a frequency of $f = 1.1\,\mathrm{Hz}$ and a decay rate (negative growth rate) of $p = -0.3\,\mathrm{s}^{-1}$. It should be noticed that the observed decay time is much longer as for the case when sodium is at rest or slowly moving. For that case, the magnetic field signals disappeared after a few hundred milliseconds after switching off the applied current.

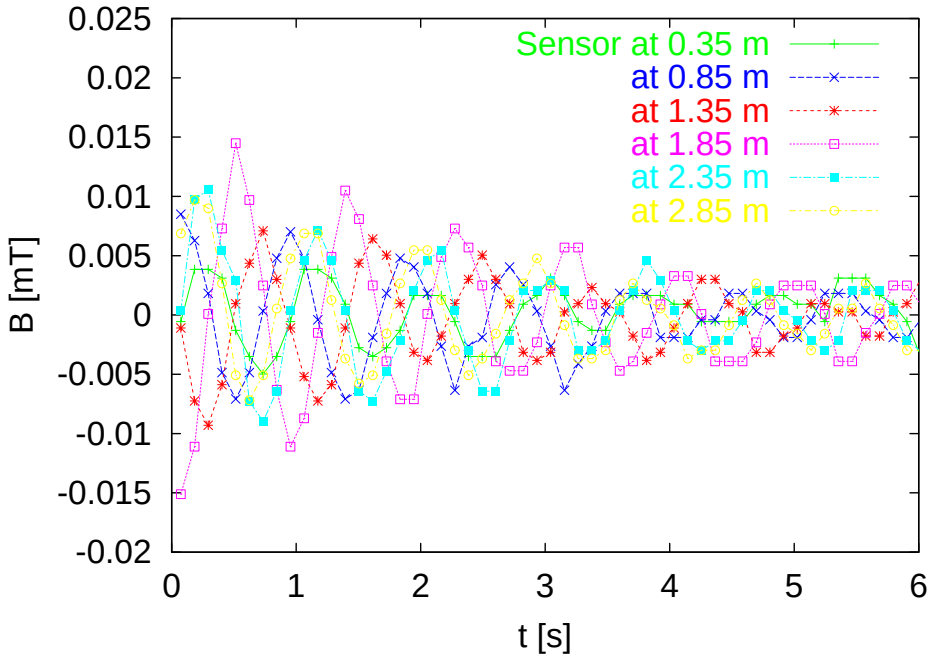

Fig. 4: Magnetic field signal at six Hall sensors located outside the dynamo after having switched off the kick-field current at 1980 rpm.

4. Comparison with numerical predictions

As the numerical work in connection with the Riga dynamo experiment was rather devoted to the optimization of the velocity profiles (in the sense of achieving a critical magnetic Reynolds number as low as possible) and to the computation of the eigenmodes and their growth rates and frequencies than to computation of the response of the dynamo on an applied magnetic field a comparison of the measured amplification factors (figure 2) with numerical results must be postponed to the future. However, as we have the measured frequencies and the growth rates of the eigenmode of the dynamos for two rotation rates we can compare them with numerical predictions.

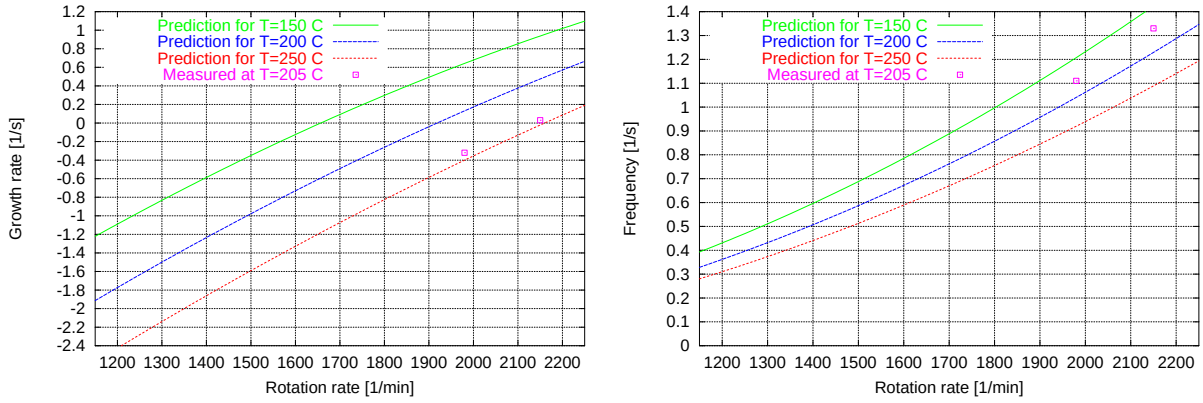

(a) (b)

Fig. 5: Comparison of measured values with numerical predictions for three different temperatures. Growth rates (a) and frequencies (b).

Figures 5a and 5b show the numerical prognoses for the growth rates and the frequencies, respectively, as well as the corresponding measured values for three different temperatures and the corresponding conductivities. Reminding the simplifications and approximations used in the numerical calculations which are based on a 2D-code [5] the agreement of the measured data with the numerical predictions is quite good. In this respect it should be noted that in the 2D-computations the effect of the finite thickness of the stainless walls was not taken into account. From 1D-calculations it is known that the main effect of these walls is to increase the critical magnetic Reynolds number by about 7 per cent. This would result in a parallel shift of the prediction curves in figure 5a and therefore to an even better correspondence with the measured values.

4. Discussion

Despite a technical problem with the seal, the first Riga dynamo experiment was successful in that it resulted in the first detection of a slowly growing magnetic field eigenmode. This eigenmode was detected on the background of an (amplified) kick-field. Thus, there might remain some doubts on whether self-excitation would have been observed also without an applied field. In this respect, one should notice the linear character of the induction equation as well as the fact that any non-linear effects due to the back-reaction of the magnetic field were likely much too small in order to „trigger“ the second mode. Additionally, the convincing correspondence of two measured eigenmode growth rates and frequencies with the numerical predictions supports the claim that a real self-excitation was observed.

The general concept of the experiment together with the fine-tuning of the velocity profile [5,6] has proved as feasible and correct. This aspect might be important for the preparation of other dynamo experiments, too, where a similar sensible dependence of the critical magnetic Reynolds number on the velocity field can be expected.

For future experiments at a lower temperature it is expected that the critical magnetic Reynolds number can be exceeded by some 20 per cent.

References

[1] A. Glatzmaier and P. H. Roberts (1995), A three-dimensional self-consistent computer simulation of a geomagnetic field reversal, Nature, 377, 203

[2] Gerbeth, F. Stefani, A. Gailitis, O. Lielausis (Eds.) (1998), Laboratory experiments on dynamo action, Workshop Proceedings, Riga, June 1998

[3] A. Denisov, W. I. Noskov, D. D. Sokolov, P. G. Frick and C. Yu. Khriptschenko (1999), O vosmoshnosti labarotornoi realizacii nestacionarnogo MHD-dinamo, Dokl. Akad. Nauk, 365, 478

[4] A. Gailitis (1993), Experimental aspects of a laboratory scale liquid sodium dynamo model, in M. R. E. Proctor, P. C. Matthews and A. M. Rucklidge (Eds.), Theory of Solar and Planetary Dynamos (pp. 91-98), Cambridge, CUP

[5] Stefani, G. Gerbeth and A. Gailitis (1999), Velocity profile optimization for the Riga dynamo experiment, in A. Alemany, Ph. Marty and J. P. Thibault (Eds.), Transfer phenomena in magnetohydrodynamic and electroconducting flows (pp. 31-44), Dordrecht, Kluwer

[6] Stefani and G. Gerbeth (1998), Contributions to the Riga dynamo experiment, in F.-P. Weiß, U. Rindelhardt, Institute of Safety Research, Annual Report 1998 (pp. 164-167)

[7] Yu. B. Ponomarenko (1973), On the theory of hydrodynamic dynamo, Zh. Prikl. Mekh. Tekhn. Fiz., 6, 47

MAGNETIC FIELD CONTROL OF THE MELT EXTRACTION PROCESS

Andreas Cramer and Gunter Gerbeth

1. Introduction

Direct extraction out of a crucible is a rapid solidification process for the production of advanced materials such as intermetallic compound fibres. The main industrial applications require these fibres to have a maximum diameter significantly below 100 μm. Today the melt extraction technology does not fulfil this requirement without additional control mechanisms. The main limitations of the process are due to turbulence within the melt and a wavy motion on the surface. In the patent literature many examples can be found which try to overcome these problems by applying mechanical parts, usually made of heat resistant ceramics. But none of them works reliably.

The present work describes a non invasive control mechanism by means of a magnetic field. Model experiments were carried out to study the calm down of the turbulent surface of an inductively stirred melt. The stabilisation of the melt surface has been demonstrated in practice by the installation of a solenoid at a working extraction facility under rough industrial conditions like a powerful induction heating and vacuum.

2. Principle of the direct melt extraction

A quickly rotating water-cooled wheel touches the surface of a continuosly lifted molten metal pool from above with the edge of one or more blades located on its circumference (Fig. 1). Due to adhesion and partial wetting liquid metal is drawn out of the melt surface, solidifies at the cold blade, shrinks and is flinged away by centrifugal forces. The length of the fibres is determined by the distance of the grooves in the blade, the kidney-shaped cross-section by the angle of the edge of the blade and the surface tension of the liquid metal.

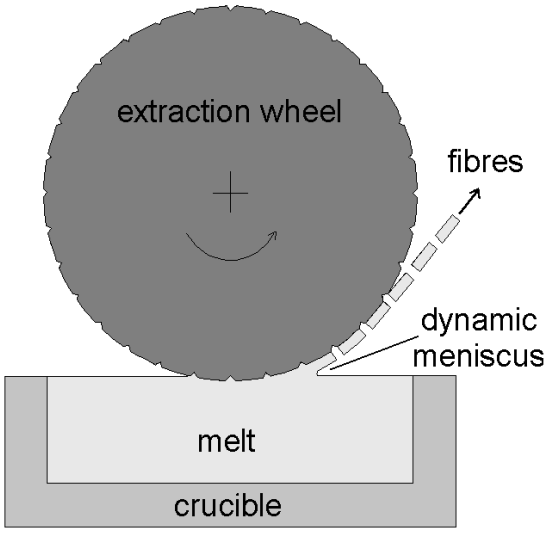

Fig. 1: Sketch of the extraction process

3. Process parameters and control

There is a clear tendency that the fibre diameter decreases slightly with increasing velocity of the wheel. Similarly, by lowering the crucible lift, smaller diameter fibres can be produced. But there are two main constraints which prohibit the extraction of fibres with well defined diameters below 100 μm.

- The process is lacking an effective control mechanism for the material flow from the melt onto the wheel, which is a complicated function of, again, wheel velocity, crucible lift and viscosity.
- There is no defined contact condition between melt and wheel due to the hydrodynamic perturbations.

Neither by lowering the crucible lift nor by increasing the velocity of the wheel it can be avoided that the extraction process is interrupted by the loss of contact between melt and wheel, far below the range where the fibre diameter decreases to the size of industrial interest. In the patent literature [1,2] no clear distinction between stabilisation of the melt surface, damping of turbulence and mass transport onto the chill wheel is made. The influence of this effects on the fibre diameter is not discussed. Only proposals are given for the application of mechanical parts which should stabilise the process by damping the flow. Many installations showed that they do not work at all due to the hazardous ambient conditions of molten metal.

To overcome all these problems a contact-less method of process control is desired. From the literature and our own work [3,4,5,6,7] it is well known that steady magnetic fields have a damping influence on convection in electrically conducting fluids. Particularly from [6,7] it is known that a transverse magnetic field is best suited to damp the hydrodynamic oscillations. Because the magnetic field is supplied over the whole volume of the fluid we will subsequently refer to this method as global stabilisation. We performed model experiments on global stabilisation and installed a similar magnetic system that creates a field perpendicular to the metal surface at a facility working under industrial conditions. The main result was that the global stabilisation is indispensable and serves as a basis for electromagnetic process control, but the field strengths within reach are not sufficient to show a significant influence on the fibre diameter. To achieve the desired small diameter much stronger magnetic fields are needed, it is sufficient to apply them in the contact region between chill wheel and metal surface. The orientation can either be the same or parallel to the axis of the extraction wheel. We decided to increase the global field near to the blade using an extraction wheel the outer part of which, including the edge, is made from iron.

4. Theoretical background

In the patent literature [1,2] the rotation of the wheel is made responsible for the turbulence, but there are 3 additional sources. The extraction process is coupled with strong temperature differences, causing natural or buoyancy convection in the bulk and thermocapillary or Marangoni convection which acts as a shear stress along the surface. The commonly used induction heating devices are based on strong alternating magnetic fields, which drive the third kind of flow. Subsequently we derive the respective velocity scales represented by the Reynolds number *Re* from the governing dimensionless numbers. Aluminium serves as an example, the physical properties are listed in the appendix. Surface tension driven flows are characterised by the Marangoni number *Ma* and with the Prandtl number $Pr = \nu/\chi$ we get:

$$Re = \frac{Ma}{Pr} = -\frac{\partial\gamma}{\partial T}\frac{\Delta T \cdot L}{\eta \cdot \nu} \tag{1}$$

where $\partial\gamma/\partial T$ is the temperature coefficient of surface tension, η the dynamic and ν the kinematic viscosity, χ the thermal diffusivity, L the typical length scale of the system, and ΔT

the temperature difference. Here ΔT is the difference between melting point and the temperature at the cooled chill wheel. Care should be taken when choosing L from the geometry of the system. Most of the volume is nearly isotherm, the steepest gradients appear in the vicinity of the wheel. Taking L of the order of mm (L=O(mm)) we get Re=O(10^4). The strength of the buoyancy convection is given by the Grashof number:

$$Gr = \frac{\alpha \cdot \mathrm{g} \cdot \Delta T \cdot L^3}{\nu^2} \tag{2}$$

with the acceleration of the free fall g and the volume expansion coefficient α. With a typical value of $\alpha \approx 1.5*10^{-4}$ for metallic melts and a crucible depth of 5cm we get the numerical value $Gr \approx 5*10^8$. With Re being proportional to the square root of Gr in the turbulent regime the Reynolds number becomes $Re \approx 2.2*10^4$.

A typical circumferential speed of the chill wheel is v=10m/s. Again we cannot exactly specify a proper typical lengthscale. Choosing 1cm is a good approximation for the contact length between wheel and melt surface as well as for the capillary dimension of the dynamic meniscus developing between the melt and the wheel (Fig. 1). With the definition of the Reynolds number:

$$Re = \frac{\mathrm{v} \cdot L}{\nu} \tag{3}$$

we get $Re \approx 8*10^4$ for the flow driven by the wheel roatation. To estimate Re for the inductively stirred melt we use again (3) and substitute v by Alfven's velocity u_A.With the magnetic field B^* of the induction heating and susceptibility μ we get:

$$u_A = \frac{B^*}{\sqrt{\mu\rho}} \qquad Re = \frac{B^* \cdot L}{\sqrt{\mu\nu\eta}} \tag{4), (5}$$

A detailed evaluation of the field amplitude created by the inductor of the heating device is beyond the scope of this report. We give the result that the analytically derived value as well as that from a numerical simulation agree well with the measured ones around 30 to 50 mT in the model experiment and at the extraction facility. With L now chosen as the crucible size we yield $Re \approx 10^5$. In conclusion one can neglect the contribution of thermocapillarity and buoyancy to the melt flow. The two other driving forces, induction heating and the forced convection by the wheel, determine the flow and are of comparable strengths.

The governing parameter which describes the damping influence of a steady magnetic field is the Hartmann number, defined as the square root of the ratio between the densities of electromagnetic energy $w_{em}=\sigma v B^2 L$ and friction energy $w_{fr}=\eta v/L$:

$$Ha = \sqrt{\frac{w_{em}}{w_{fr}}} = B \cdot L \cdot \sqrt{\frac{\sigma}{\eta}} \tag{6}$$

with the electrical conductivity σ. As a characteristic number to describe the ratio between electromagnetic forces and the fluid inertia we also use the dimensionless number:

$$N = \frac{Ha^2}{Re} = \frac{\sigma \cdot L \cdot B^2}{\rho \mathrm{v}} \tag{7}$$

N is known as the magneto-hydrodynamic (MHD) interaction parameter.

5. Description of the experiments

With the availability of an existing extraction facility at the IFAM (Institut für angewandte Materialforschung, Fraunhofer Gesellschaft, Dresden) we had the possibility to study the magnetic damping of all types of fluid motion involved in the industrial process. To investigate the separated effects we set up two model experiments. With the first one it is not possible to extract fibres, but it allows for an examination of the induction heating alone. The second uses low melting point metals which can be heated with resistance wires, thus omitting the stirring by induction heating. An effective damping of the turbulence in the melt can be expected for $N>>1$. With the above derived Reynolds numbers, given material properties and the geometry, the requirements to the magnetic field are already predetermined.

5.1. Extraction apparatus at IFAM

For the crucible size of 13cm x 8cm x 5cm and the demand of $N \geq 10$ we require $Ha>1150$, respectively B>0.13T, based upon the properties of aluminium. We produced fibres from Ni3Al and X5CrAl23.10-steel, too. For these lower conducting metals the damping is weaker, but due to the higher viscosities *Re* decreases for both, the induction heating and the flow driven by the wheel. As a net effect the damping efficiency is not worse for the latter metals. Nevertheless we constructed a solenoid that creates 0.4T at the bottom of the crucible and 0.25T at the metal surface to investigate a larger range of N even higher than 10. The technical problems to be solved were related to the vacuum conditions in the whole apparatus to avoid fibre corrosion and to the close vicinity to the strong induction heating device. We decided for a compact design of 19 windings, carrying a current of 3200 A. The heat release of 25kW requires a water cooling of the solenoid. Thus, the housing of the magnet must provide high pressure resistance and efficient shielding of the windings of the solenoid against the two turns of the inductor to prevent the power supply from high voltage. All this could be reached by using a circular geometry with 1cm thick profiled copper-sheet housing. To increase the field strength a ferromagnetic core has to be used, which must be protected against the induction heating, too.

5.2. Quasi-isothermal model of an inductively stirred melt

The experimental model consisted of a rectangular stainless steel crucible which was placed in a rectangular AC field inductor and filled with the eutectic melt In-Ga-Sn being liquid at room temperature. In order to control the temperature of the pool the thickness of the stainless steel walls was 0.5mm only and the crucible was surrounded by a water cooled jacket. The AC field inductor consisted of 3 water cooled copper pipe windings with 2.4kHz current up to 1.2kA. With the measured field strengths, the properties of In-Ga-Sn and the crucible geometry (15.2cm x 9cm x 7cm) according to (5) *Re* ranged up to $12*10^4$. The maximum value of the steady magnetic field of 0.4T made it possible to reach Hartmann numbers up to 1850. In the liquid metal volume, local velocity measurements were carried out with conventional potential difference probes. This method works reliably for $Ha>100$. The upper surface of the liquid metal was free in the sense that it was deformable, but was covered by a thin metal oxide film. These surface deformations were visualised and recorded by video.

5.3. Resistance wire heated extraction facility

The second branch of simplifying the full problem can be studied when omitting the induction heating. Eutectic Sn-Pb was used (205°C to 350°C) to overcome the limitations of the significant lower temperatures which can be reached with resistance wire heating. With the crucible dimension of 10cm x 6cm x 3 cm we were limited to a maximum induction of 0.3T and $Ha \leq 700$. Unfortunately the viscosity of Sn-Pb is small. As a result the interaction parameter N is smaller than 2. Nevertheless, this model with it's low melting point metal permits much better access to any kind of measurement than the real facility.

6. Results

The crucible at the IFAM apparatus was filled to the upper rim. While running the induction heating alone we observed very large deformations of the liquid metal surface. At the side walls the level of liquid metal was 3cm below the rim and in the centre it rose more than 1cm. The main mode of instability was a sloshy motion with a wavelength in the order of the crucible dimension and an amplitude of 1cm. With a solenoid current of 2.9kA (Ha=2000) the metal surface became completely planar and calm.

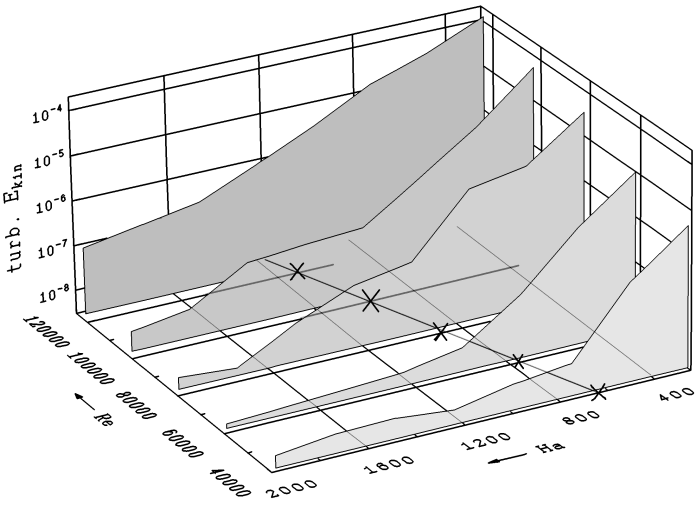

Fig. 2: Stability diagram for the damping of an inductively stirred melt by a DC magnetic field

The complete damping of the turbulence generated by the induction heating was confirmed in the model experiment in more detail by measuring the two horizontal velocity components in a wide (Re,Ha) parameter space. We calculated the turbulent kinetic energy from the velocity pulsation. It can be seen from Fig. 2, that for Ha=1850 a damping of the turbulent energy of nearly 3 orders of magnitude is possible. To get the relation to the dimensionless parameter N we depicted the curve N=10 on the bottom of the diagram.

When starting the fibre extraction at the IFAM facility small ripples appeared in front of the chill wheel. Both, the wavelength and the amplitude were below 1mm. Without magnetic damping this comparable weak wavy motion could so far not be resolved within the turbulence generated by the induction heating. We found this small surface waves at the model extraction apparatus, too.

The real process does not allow in-situ measurements of velocity or temperature, only the final cross-section of the fibres can be measured quantitatively. Although the Reynolds numbers for the flow driven by the wheel (3) and that driven by the induction heating (5) are in the same order of magnitude no significant influence on the fibre diameter was found by damping the turbulence with the global field strength up to 0.25T. But the global field allows for a nearly

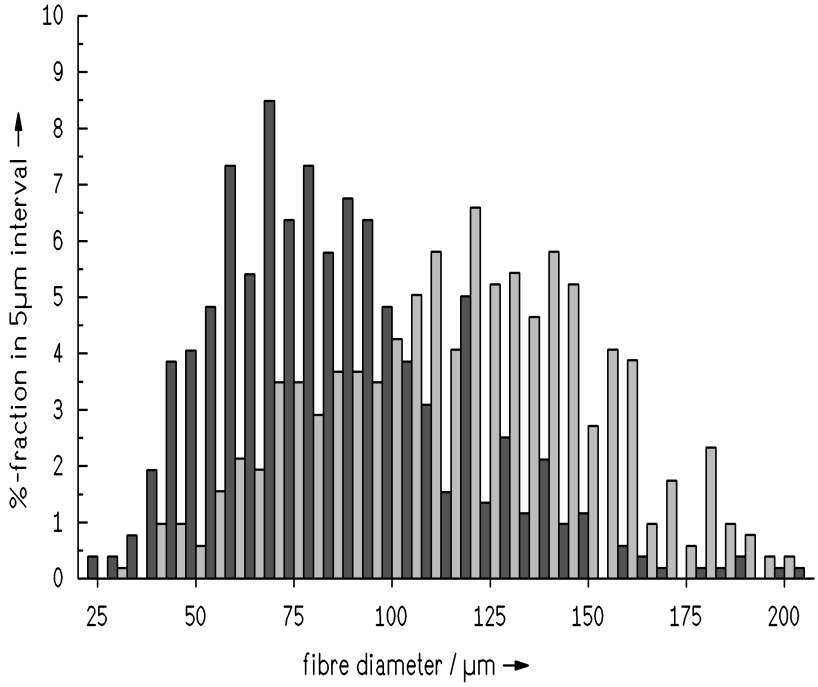

Fig. 3: Fibre distribution of an extraction run at the resistively heated model facility at T=245°C, v_{wheel}=7m/s, lift=6.5µm/s with (dark, B=0.71T locally at the edge) and without (bright) magnetic field.

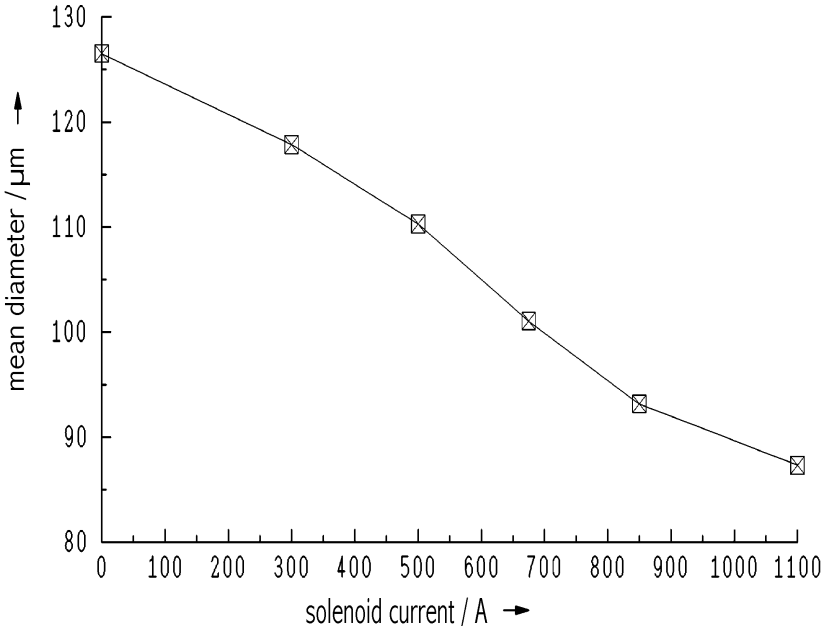

Fig. 4: Dependence of the fibre diameter on the strength of the local magnetic field for the extraction parameters T=245°C, v_{wheel}=6m/s, lift=6.5µm/s

two times higher rotation rate. With the net decrease of the diameter of about 10-20% at the highest possible wheel speed the main goal cannot be reached by the global stabilisation alone. Nevertheless, the process runs much more stable and the productivity can be improved by the higher rotation rates.

Qualitatively we observed an average elongation of the meniscus of about 50% for an induction of 0.2 T of the global field. This elongation can be attributed to the increase of the virtual viscosity produced by the magnetic field. This effect approximately compensates the advantage of the higher rotation rate of the extraction wheel with respect to the fibre diameter. The iron-ring-equipped wheel used in the model extraction facility to increase the magnetic field in the meniscus region does not have this disadvantage. With an induction of 0.1T at the crucible bottom and even less at the melt surface we measured 0.71T at the edge of the blade, as close as it is possible due to the finite size of the sensor. We even expect values near the saturation of the iron directly at that edge. This configuration for the local stabilisation allows to extract thinner fibres as can be seen in figures 3 and 4. The induction of 0.71T at the edge corresponds to the maximum solenoid current of 1100A.

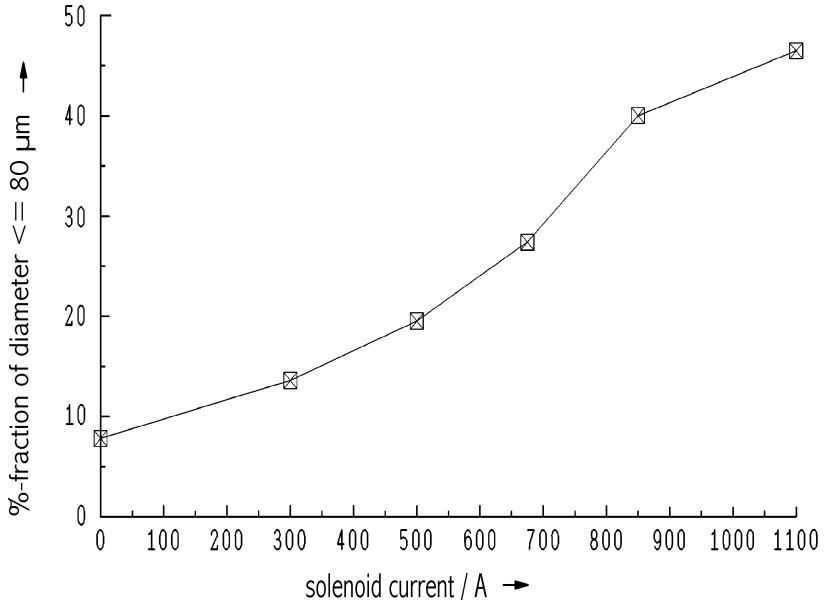

Fig. 5: Percentage fraction of diameter of fibres below 80 µm for the same series as used in Fig. 4

Another practical aspect is the percentage fraction of fibres below a certain diameter. As an example Fig. 5 shows such a diagram for the value of 80 µm. Whereas the mean diameter in Fig. 4 decreases only by 30%, the fraction of fibres of interest increases by a factor of 6.

The size of the dynamic meniscus becomes smaller if a local field alone or an additional local field of a strength that is large compared to the global one is applied. This is in contradiction to the case where a global field leads to a growth of the meniscus. To get some insight into the mechanisms we performed several high speed video recordings. First, they revealed that the meniscus oscillations neither correspond to the rotation rate of the wheel nor to the distance of the grooves in the blade to determine the length of the fibres. The detailed investigations of one period of the meniscus oscillations recorded during an extraction with a 170mm diameter wheel running at circumferential speed of 6.9m/s without magnetic field showed the following. While the wheel rotates at 12.9Hz (the number of grooves was 32 giving a frequency of 413.4Hz) the inverse of the period of the meniscus oscillation was 27.8Hz.

Further, the melt is not in contact with the extraction wheel all the time. Due to the crucible lift this contact is established. The meniscus is formed, develops, and during this growth the fibres are extracted. After the meniscus reaches it's full size the contact is lost. This scenario repeats for the next period of the meniscus oscillation.

The second clearly observable influence of the magnetic field, besides the increase of meniscus size in the case of the global field, is the change in the ratio of contact to contact-less time under the influence of the local field. For both cases the time-averaged material flux is the same. As the fibre diameter is merely influenced by the global field it is obvious, that the ratio of contact to contact-less time is not influenced here, too. The observation that the contact time is increased is in agreement with the result that the fibre diameter becomes smaller with the local field. Whereas the elongated meniscus can be attributed to the increase of virtual viscosity created by the global field the smaller meniscus size with the local field is not understood for the moment.

7. Summary

The global stabilisation is necessary as a basis for inductively heated extraction facilities and already shows an influence on the local behaviour of the meniscus. A significant reduction of

the fibre diameter cannot be reached by the globally applied field alone, a local magnetic control directly in the meniscus region is required to achieve this. In the present work an amplification of the global field with a ferromagnetic material was used. Future investigations will be directed to the influence of a separate local field applied in the horizontal direction parallel to the wheel axis. Further we intend to do a more detailed study of the meniscus behaviour using high speed video recordings.

From the technical point of view it is worth to note that a DC magnetic field has been installed under hazardous industrial conditions. Different types of lower melting point model experiments have been performed to separate the different physical mechanisms involved in the complex technical process.

References

[1] Bedell et. al. (1975) United States Patent No. 3.863.700

[2] Pond, et. al. (1979) United States Patent No. 4.170.257

[3] Y. Gelfgat (1993) Influence of the magnetic field on the oscillatory instability and supercritical regimes of buoyancy convection, Proc. VI. Int. Symp. on transport phenomena in thermal engineering, Seoul

[4] H.B. Hadid, D. Henry, S. Kaddeche (1997) Numerical study of convection in the horizontal Bridgman configuration under the action of a constant magnetic field. Part 1. Two-dimensional flow, J. Fluid Mech., 333, pp. 23-56

[5] H.B. Hadid, D. Henry (1997) Numerical study of convection in the horizontal Bridgman configuration under the action of a constant magnetic field. Part 2. Three-dimensional flow, J. Fluid Mech., 333, pp. 57-83

[6] J. Priede, G. Gerbeth (1997) Hydrothermal wave instability of thermocapillary-driven convection in a coplanar magnetic field, J. Fluid Mech., 347, pp. 141-169

[7] J. Priede, G. Gerbeth, (2000) Hydrothermal wave instability of thermocapillary-driven convection in a transverse magnetic field, J. Fluid Mech., 404, pp. 211-250

[8] A.Cramer, A. Bojarevics, G.Gerbeth, Y. Gelfgat (1999) Stabilisation of the melt extraction process with a magnetic field, Proc. 128th TMS-Meeting, San Diego

Appendix – physical properties

Substance	σ $(\Omega*m)^{-1}$	η (Pa*s)	ν (m^2/s)	χ (m^2/s)	$d\gamma/dT$ (N/m*K)
Aluminium	$4.85*10^6$	$1.1*10^{-3}$	$0.474*10^{-6}$	$7.74*10^{-5}$	$1.55*10^{-4}$
In-Ga-Sn	$3.3*10^6$	$2.16*10^{-3}$	$0.34*10^{-6}$	$1.87*10^{-5}$	n.a.
Ni3Al	$2.11*10^6$	$3.9*10^{-3}$	$0.6*10^{-6}$	n.a.	n.a.
Sn-Pb	$1.52*10^6$	$2.8*10^{-3}$	$0.34*10^{-6}$	n.a.	$0.5*10^{-4}$
X5CrAl23.10	$1.49*10^6$	n.a.	n.a.	$1.37*10^{-5}$	n.a.

IRRADIATION RESPONSE OF VVER PRESSURE VESSEL STEELS: FIRST RESULTS OF THE RHEINSBERG IRRADIATION PROGRAMME

Jürgen Böhmert, Hans-Werner Viehrig, Holger Richter

1. Introduction

An extensive irradiation programme was performed at the VVER 2 of the Rheinsberg nuclear power plant between 1983 and 1990. Almost 2000 specimens made from 37 various heats of preferentially VVER pressure vessel steels were irradiated in different irradiation rigs during one reactor cycle each.

The programme should considerably enhance the data base for irradiated materials. Mainly, the influence of detrimental elements, such like phosphorus or copper, and the metallurgical treatment should be analyzed. The final goal was to contribute to the validation of the predictive formula describing the neutron embrittlement as they are formulated in the Russian guides.

The prototype reactor VVER 2 is especially suitable as irradiation facility because the neutron fields and the temperature condition are comparable with the VVER 440. Moreover, the large cross section of the high flux channels allows to irradiate large and numerous specimens.

The programme comprises two parts. A first part is a German-Russian cooperation project. In this part Materialprüfanstalt Stuttgart and Forschungszentrum KFA Jülich were also involved. A second part was designed and prepared by Zentralinstitut für Kernforschung Rossendorf which was the predecessor for Forschungszentrum Rossendorf (FZR).

Testing of the specimens was delayed as the FZR´s hot cell laboratories had been reconstructed. Since 1998 the FZR has had new hot cell laboratories with facilities for preparation and testing of irradiated specimens. In these laboratories the specimens of the first part of the irradiation programme were tested. Some results of the tests are presented in the following.

2. Experimental

The material tested by FZR [1] consists of

- 4 heats from VVER 440-type base metal 15Kh2MFA (15CrMoV 2) (code: R1, R2, R3, D25)
- 2 heats from VVER 1000-type base metal 15Kh2NMFAA (15CrNiMoV2) (code: R16, R17) and
- 1 heat from VVER1000-type weld metal 10KhGNMAA) (10CrMnNiMo 1) (code: R19) [1].

Most of the heats have a rather low content of the harmful elements copper and phosphorus (Tab. 1). Hence the irradiation sensitivity should be low. From each heat, Charpy V-notch standard and precracked specimens were available in the unirradiated, the irradiated and partly the post-irradiation annealed state.

The specimens were taken from the 1/4 to 3/4 thickness position and in L-S, T-S, L-T and T-S orientation. The specimens were placed in open irradiation rigs in the high flux irradiation positions (target channels) with direct contact to the coolant (255 °C inlet temperature). The mean neutron flux rate was 2.6 10^{12} $cm^2 \cdot s$ [E>1MeV]. The fluences of different specimens of one set vary up to a factor of 2. Therefore, the results of the tests were corrected to the same mean fluences. Both the details of the irradiation and the correction procedure are given in [2].

The Charpy impact tests were performed with an instrumented impact pendulum in the temperature range of -150 °C to +300 °C. Testing of the precracked specimens is based on the master curve concept according to ASTM E 1921-97 using the multiple temperature method [3]. The specimens were loaded by three-point bending with a servo-hydraulic test system „MTS 810-Test Star" in a nitrogen cooled environmental chamber.

3. Results

The two VVER 440 base metal heats (R1 and R3) excepted, in general all investigated materials exhibit a high toughness in the unirradiated state. Particularly the Charpy toughness parameters of the VVER 1000 base metal are excellent. As usual the toughness of the weld metal is lower but sufficient according to the Russian specification. Definitely, irradiation within the investigated fluence range from 23.2 to 138 $\cdot 10^{18}$ /cm^2 [E > 0.5 MeV] affects a clear degradation of the toughness. Irradiation shifts the ductile-brittle transition temperature to higher temperatures, lowers the upper shelf energy and extends the transition range. Figs. 1 and 2 illustrate this phenomenon for heats of VVER 440 base metal and of VVER 1000 weld metal. Using the Russian procedure [1] for the evaluation of the irradiation sensitivity

$$\Delta TT = A_F \cdot \sqrt[3]{F} \qquad (1)$$

an irradiation embrittlement coefficient A_F can be estimated from the fluence F (in 10^{18}/cm^2 [E > 0.5 MeV) and the measured transition temperature shift $\Delta TT = TT_F - TT_o$. Tab. 1 summarizes the calculated values for A_F. The values range from 3.4 for a 15Kh2MFA heat (R1) to 47.5 for the weld metal (R19). This means that for typical end of life fluences $\geq 10^{20}$ /cm^2 [E>0.5 MeV] the transition temperature shifts range between 20 and ≥220 °C. Whereas a shift of 20 °C proves an excellent irradiation resistance, a shift of more than 250 °C is not acceptable even if the transition temperature is very low in the initial state.

Table 1: Irradiation embrittlement coefficients A_F

material	code	Cu / weight-%	P / weight-%	Φ_{mean} [x 10^{18} ncm^{-2}]	ΔTT_{48J} [°C]	A_F
15Kh2MFA	R1	0.10	0.011	43.6	12	3.4
	R2	0.12	0.014	80.7	32	7.4
	D25	0.11	0.017	127.6	99	19.7
	R3	0.12	0.024	47.5	47	13.1
15Kh2NMFAA	R16	0.07	0.012	46.0	65	18.1
	R17	0.13	0.013	72.7	119	28.5
10KhNGMAA	R19	0.05	0.008	65.1	191	47.5

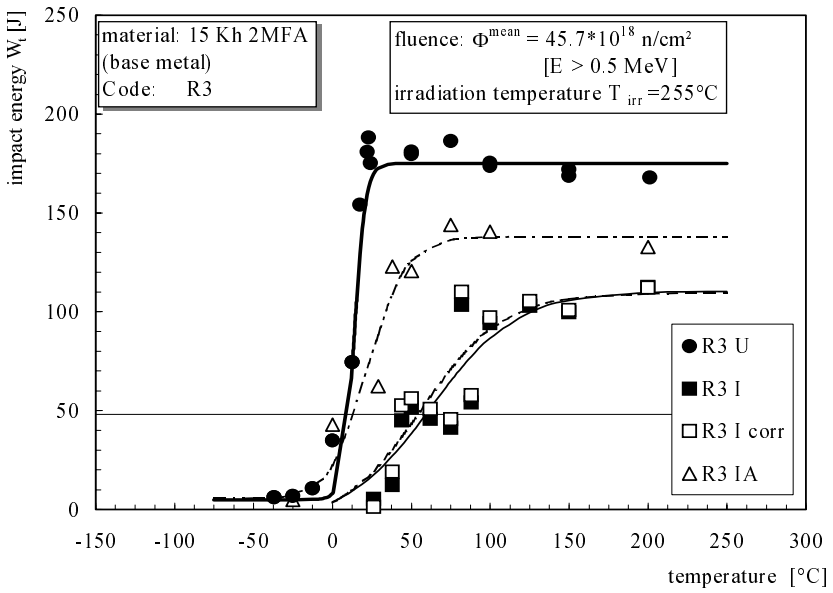

Fig. 1: Charpy V impact energy temperature curves of VVER-440 base metal (R3) in the as-received (U), irradiated (I) and annealed (IA) state

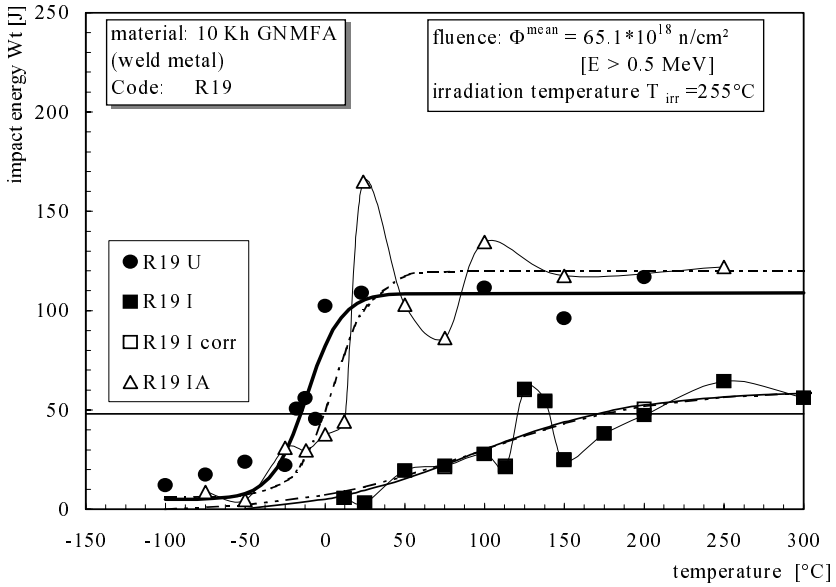

Fig. 2: Charpy V impact energy temperature curves of VVER-1000 weld metal (R19) in the as-received (U), irradiated (I) and annealed (IA) state

The irradiation embrittlement coefficient A_F depends on the material composition and the irradiation temperature. The Russian guide is based on the following rules [2]:

$$A_F = 800\ (\%\ P + 0.07\ \%\ Cu) \qquad (2a)$$

for weld metal, WWER-440, $T_{irr} = 270$ °C

$$A_{F\,T} = A_{F\,270} + K\ (T_{270} - T_{irr}) \qquad (2b)$$

with K = 0.2 for base metal and K = 0.4 for weld metal

maximum values for VVER 440, T_{irr}=270 °C maximum values for VVER 1000, T_{irr}=290

$A_F \leq 15$ weld metal $A_F \leq 20$ weld metal

≤ 18 base metal ≤ 23 base metal (2c)

For the different materials the transition temperature shifts are calculated using equations (1) to (2a-c) and compared with the measurements. The comparison is shown in Fig. 3. On the base of the Russian guidelines always conservative predictions are obtained apart from the weld metal (R19). The very high irradiation embrittlement sensitivity of material R 19 is not correctly predicted. As the material meets the Russian specification regarding both the chemical composition and the heat treatment, this irradiation response is unexpected. Also the microstructure does not give a clue for the irregularity. R19 is a weld material. Weld metal is considered to have the highest susceptibility to embrittlement. Nevertheless, the finding cannot be explained consistently what is a proof for our lack of adequate knowledge on the phenomenon.

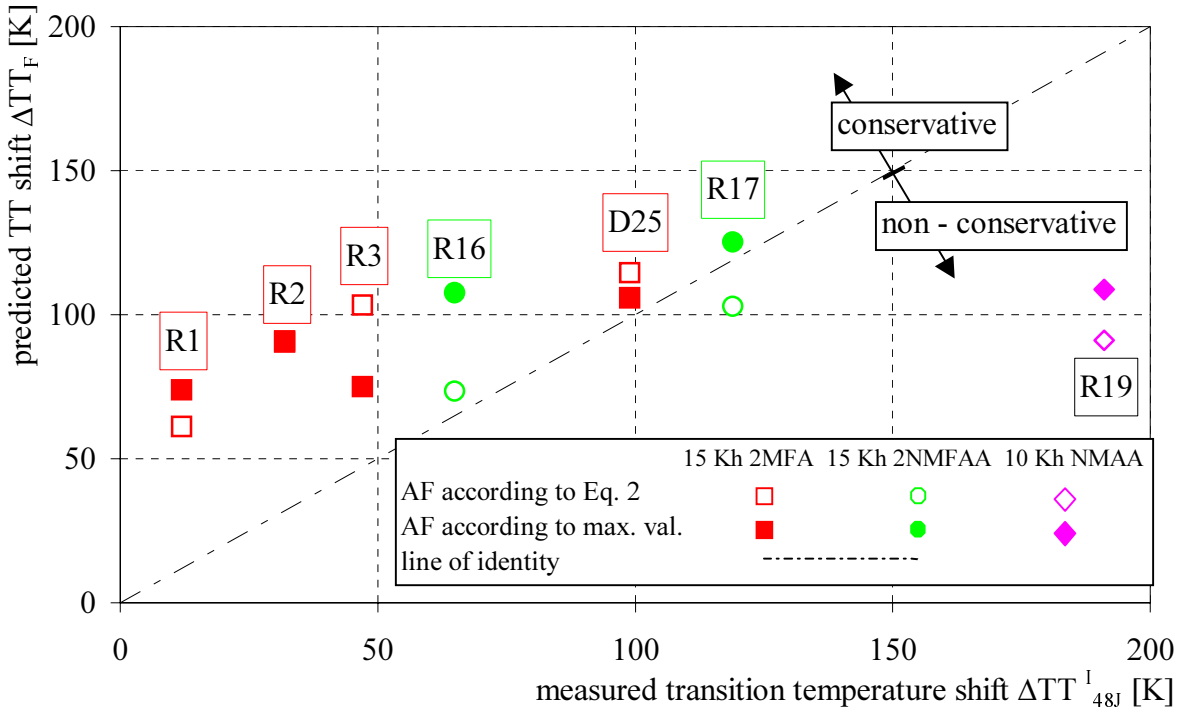

Fig. 3: Transition temperature shift due to irradiation related to a Charpy V-impact energy of 48 J - comparison between predicted and measured values

An annealing treatment to recover the thoughness has become a must for the old VVER-440 s. There are well-tried annealing technologies but, unfortunately, their efficiency has not yet been sufficiently validated. The effect of annealing can be described by a recovery parameter R defined as relative change of the transition temperature TT or the upper shelf energy USE

$$R = \frac{P_{irr} - P_{ann}}{P_{irr} - P_{unirr}} \; 100 \; [\%] \qquad (3)$$

where P_{irr}, P_{ann}, P_{unirr} are the concerning Charpy impact test parameters (TT, USV) in the unirradiated, the irradiated or the annealed state.

After 100 h annealing at 475° C the recovery parameter R is shown in Fig. 4. Both "over-recovery" and incomplete recovery can be observed. From the safety point of view the results are favourable: the heats with the highest irradiation sensitivity reveal complete recovery. One

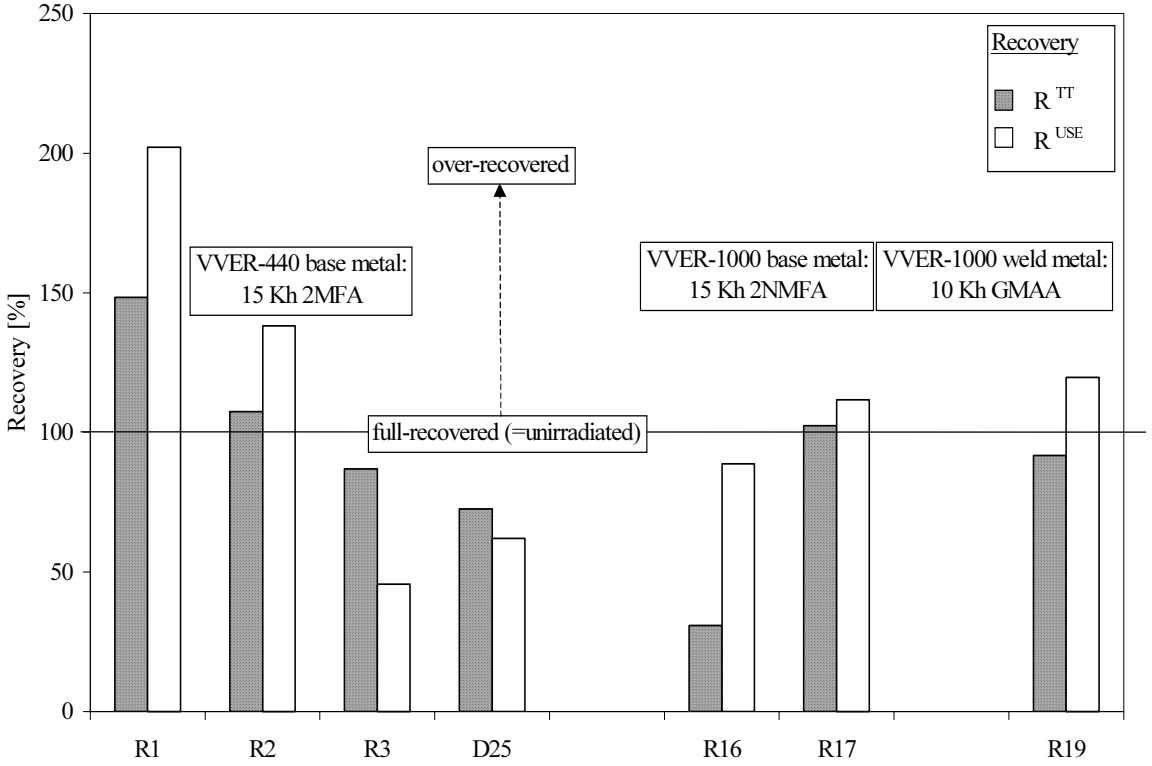

Fig.4: Recovery of Charpy V parameters

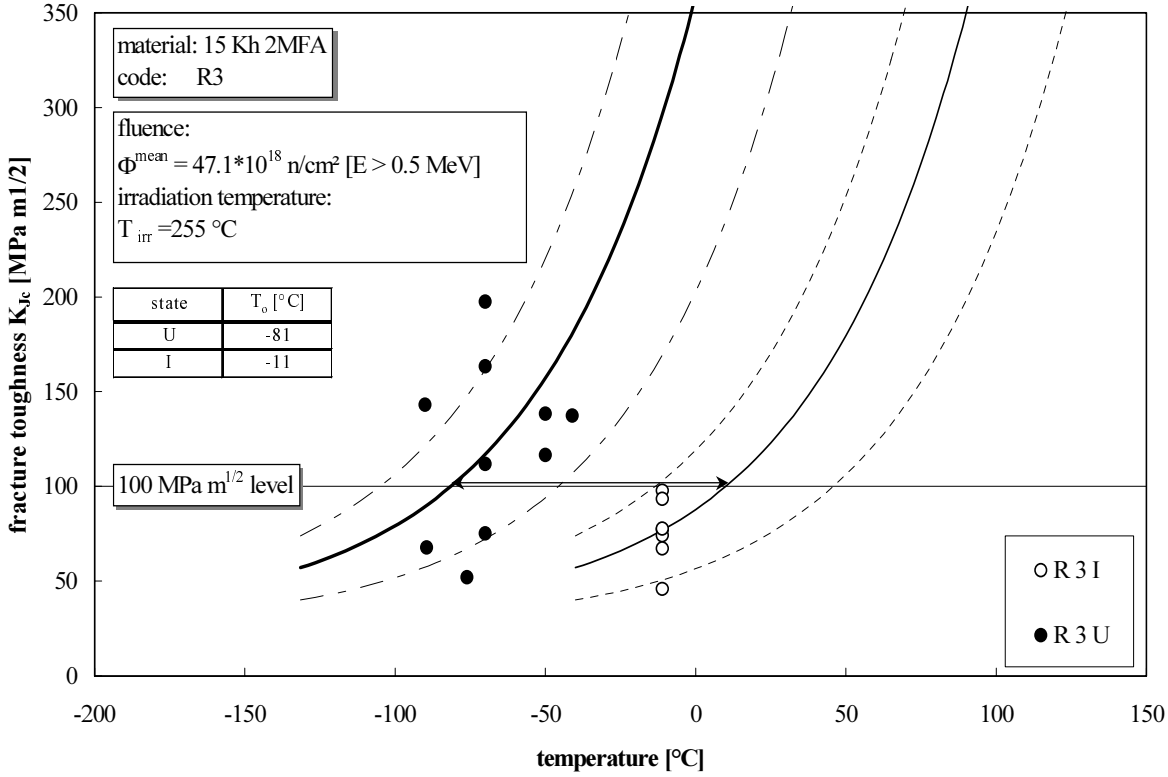

Fig. 5: Fracture toughness, K_{Jc}, - temperature curve for heat R3 from VVER-440 steel in the unirradiated (U) and irradiated (I) state

should notice that the transition temperature shift of heat 16 is hardly recovered by annealing. Heat 16 only differs from the other heats in the small grain size and the shorter tempering at lower temperature.

Fracture mechanics parameters were determined using the master curve concept [4]. The master curve is a commonly valid fracture toughness-temperature curve. The position on the temperature axis is defined by a material-dependent reference temperature T_o. Fig. 5 presents the fracture toughness - temperature curve (mean curve with 5 and 95 % probability boundaries) for heat R3 in the unirradiated and irradiated state. Irradiation shifts the curve to higher temperature. The shift is larger than the transition temperature shift measured by Charpy impact tests. In other cases both characteristic temperature shifts are approximately comparable with each other. Predictive formula which describe the influence of the irradiation on fracture mechanics parameters for VVER steels have not yet been available. Nevertheless, the Charpy transition temperature shift seems to provide a useful estimation for the irradiation-induced changes of the fracture mechanics response, too.

4. Conclusion

For 7 heats from VVER 440 and 1000 reactor pressure vessel steels, the change of the Charpy impact parameters and the master curve reference temperature T_o due to irradiation and annealing could be determined.

As a rule, the irradiation behaviour meets the prediction of the Russian guides in a conservative manner and is not critical from the safety point of view. However, there are surprising non-conservative results after both irradiation and annealing. Such outliers are suspect and we have not yet been able to explain the effect. Microstructural investigations are planned to clarify the abnormal behaviour.

References

[1] H.-W. Viehrig, J. Böhmert, H. Richter (1999), Common German/Russia Irradiation Experiment at Rheinsberg NPP - Results of the Mechanical Testing, Proc. of a IAEA Specialist‘s Meeting on Irradiation Embrittlement and Mitigation, IAEA, Madrid

[2] H.-W. Viehrig, Barz, H.-U. Barz, J. Boehmert, B. Boehmer (1997), Consideration of neutron flux gradients for sophisticated evaluation of irradiation experiment, Proc. of the IAEA Specialists Meeting, Vladimir, Russia,, Sept. 1997, IWG-LMNPP-97/2, Vienna, pp. 230

[3] H.-W. Viehrig, J. Boehmert (1999), Some Issues by Using the Master Curve Concept, 15th International Conference on Structural Mechanics in Reactor Technology, SMiRT-15, August 15-20, Seoul, Korea

[4] K. Wallin (1997), Small Specimen Fracture Research Characterisation-State of the Art and Beyound, Proc. of the Advances in Fracture Research, ICF 9, B.L. Karihaloo, Y.M. Mai, M.I. Ripley, R.O. Ritchie (Eds.), pp. 2333-2344, Amsterdam

SOME ISSUES USING THE MASTER CURVE CONCEPT

Hans-Werner Viehrig and Jürgen Böhmert

1. Introduction

The state-of-the-art structural integrity assessment of reactor pressure vessels (RPV) is based on the Reference Temperature Concept, initially proposed by the American Society of Mechanical Engineers (ASME) [1,2]. An experimentally ensured fracture toughness curve was constructed as the lower boundary of the available fracture toughness, K_{IC}, of RPV steels. This conservative curve describing K_{IC} as a function of temperature is used as an universal curve. For different RPV steels the curve is placed on the temperature axis over a reference temperature. In the initial state the nil-ductility-transition temperature (RT_{NDT}) is applied as reference temperature. The ductile to brittle transition temperature (DBTT) shift caused by the neutron irradiation is determined by Charpy V impact tests. The Charpy V DBTT shift is one of the results of the RPV surveillance programmes. The concept based on the ASME curve has the following disadvantages:

- it is not consistent since it links fracture mechanical and technological parameters and
- margins of safety and uncertainties cannot be quantified.

Moreover, a consistent evaluation after the plane-strain, linear-elastic concept is not really practicable because of specimen size requirements. Recently, Wallin [3,4] has developed a new methodology to characterize the fracture toughness in the lower transition region. J-integral-based cleavage fracture toughness, K_{JC} values were analysed using the statistical Weibull model. This methodology has demonstrated that the estimates of the median fracture toughness of ferritic steels tend to form transition curves of the same shape. It is called the „master curve". From the mathematical point of view ASME and master curve are identical in the shape. In case of the master curve, the reference temperature, T_o, is, however, defined as the temperature at which the fracture toughness for a fracture probability of 50 % is equal to 100 $MPam^{1/2}$. Although the master curve concept is already adopted by the American Society for Testing and Materials (ASTM) as standard [5], the methodology has not yet become a generally accepted part of the RPV safety assessment. More experience in the application of the concept to different materials is necessary. The results presented below contribute to this task. A thick-wall section of a RPV steel plate with strong segregation structures was carefully tested by Charpy V impact and fracture mechanical testing. Particularly, the study aims at

- proving that valid master curves can be determined with small Charpy size specimens,
- characterizing the toughness over the thickness of the plate and the scattering in terms of the temperatures T_o, and at
- comparing the T_o temperatures with Charpy V transition temperatures for a strongly segregated material.

2. Material and Specimens

The material investigated is a rolled plate of ASTM type A533B Class 1 RPV steel which is used as IAEA reference material (code JRQ). Table 1 contains the chemical composition and the

mechanical properties.

Table 1: Chemical composition (wt.%) and mechanical properties of IAEA JRQ RPV steel

C	Si	Mn	Cr	Mo	Ni	P	Cu	V	S	Al
0.18	0.24	1.42	0.12	0.51	0.84	0.017	0.14	0.01	0.002	0.021

tensile yield strength: 477 ± 10 MPa
ultimate tensile strength: 630 ± 3 MPa

The microstructure at various locations through the thickness was characterized by optical microscopy of etched metallographic sections. The basic microstructure is bainitic. The bainite is preferentially lower bainite and martensite at the surface layer and a heterogeneously composed upper bainite within the middle section. Within the bainitic basic structure reticular arrangements of martensitic structure occur. The reticularly arranged martensitic structure becomes more and more pronounced in the thickness direction and must be explained by segregation. The following types of specimens were tested:

- standard Charpy V-notched specimen (T-L orientation) and
- precracked and side grooved (20 %) Charpy size specimens (T-L orientation).

3. Test Methods

The instrumented Charpy V impact tests were carried out with an instrumented 300 J impact-pendulum and a test velocity of 5.5 m/s. The fracture mechanical tests were performed according to ASTM E 1921-97 standard [5]. The specimens were loaded with a servohydraulic test system „MTS 810 -Test Star" using the unloading compliance technique. The measured J-integral values at brittle failure were transformed into elastic plastic fracture toughness, $K_{JC,}$ values.

4. Results

A Weibull distribution with a fixed slope of 4 is used to construct a master transition curve in dependence on the temperature by the following equation for specimens with a thickness of 25.4 mm (1T size) [3,5]:

$$K_{JC(med)} = 30 + 70 \exp [0.019 [T - T_0)] \quad (1)$$

where $K_{JC(med)}$ is the fracture toughness for a fracture probability of 50 %,
T is the temperature and
T_0 is the reference temperature at which $K_{JC(med)}$ equals 100 $MPam^{1/2}$.

The temperature T_0 can be calculated using Eq. 1 or it can be obtained by the multi-temperature (m-t) method [3]. The m-t method offers the possibility to include specimens in the T_0 temperature evaluation which were tested at different test temperatures. All elastic plastic fracture toughness, K_{JC}, data sets of the different thickness layers of the RPV steel plate determined by the master curve concept according to the m-t evaluation are shown in Fig. 1.

The K_{JC} values are adjusted to a specimen thickness of 1 T size [3,5] and plotted against the temperature difference T - T_0. It is shown that most of the K_{JC} values are within the tolerance bounds (5 and 95 %). K_{JC} values of specimens from the 1/4 to 3/4 through-the-thickness position of the plate (filled circles and squares in Fig. 1) strongly scatter at the same test temperature. The results show the problems of the fracture mechanical testing of small specimens. On the one hand, the fracture toughness measuring capacity given by the maximum validity limit according to the ASTM E1921-97 standard [5] is rather low for the small Charpy size specimens. On the other hand, the inhomogeneously segregated structure of the material within the inner range of the plate causes a strong scatter of the measured K_{JC} values. There are K_{JC} values above the maximum validity limit and below 50 $MPam^{1/2}$. Under these circumstances the selection of the test temperature is difficult and the aid given in the ASTM standard [5] is applicable only as a rough estimation. The variation of the test temperature and the application of the m-t method facilitate the determination of the temperature T_0. However, it was impossible to fulfill the requirements in the ASTM standard with only 6 tests performed with specimens of the inhomogeneous materials from the inner thickness positions.

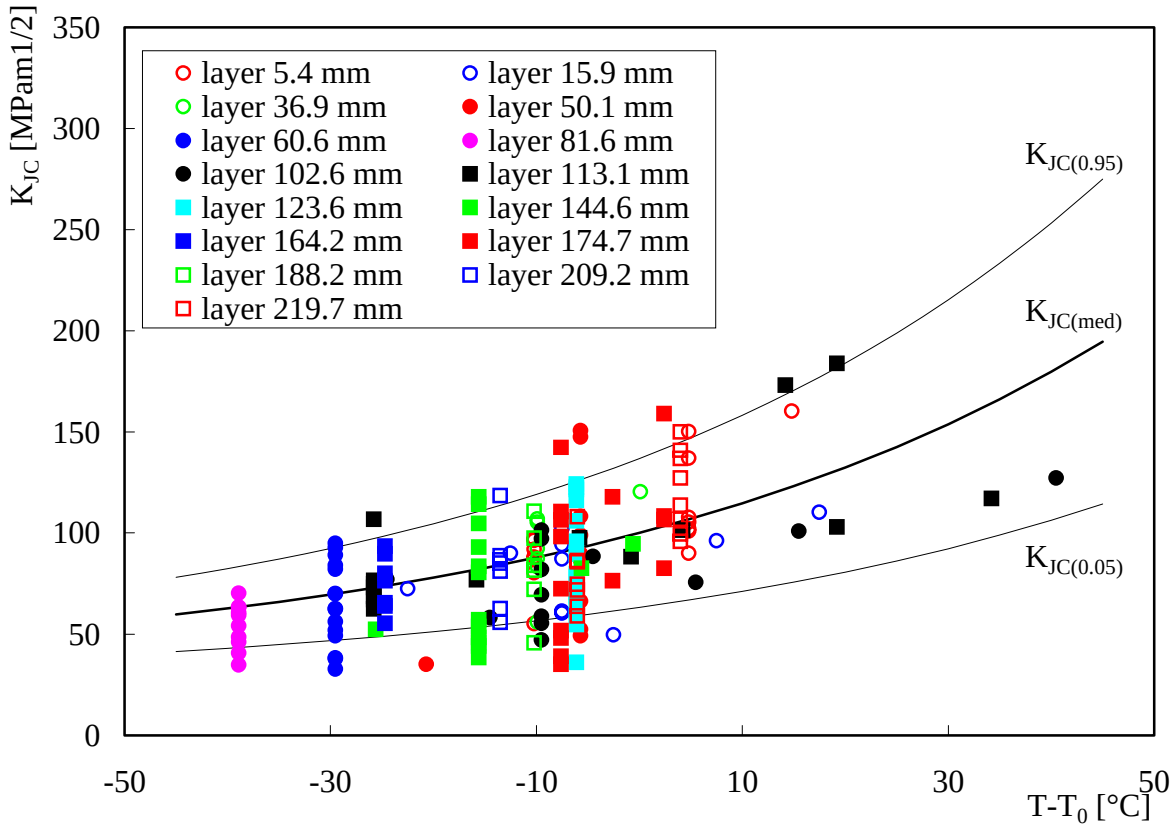

Fig. 1: Fracture toughness versus test temperature scaled on T_0 (m-t method)

Fig. 2 shows the evaluated T_0 temperatures in dependence on the thickness position. Obviously, T_0 increases from the surface to the middle. In general, the course of T_0 over the thickness is nearly equal for both methods. Strong scattering occurs between the transition temperatures at different through-the-thickness locations, especially within the middle range. It is supposed that the scatter is caused by the reticularly arranged martensitic structure in the inner range of the plate.

Fig. 3 shows the dependence of the evaluated Charpy V transition temperatures on the thickness.

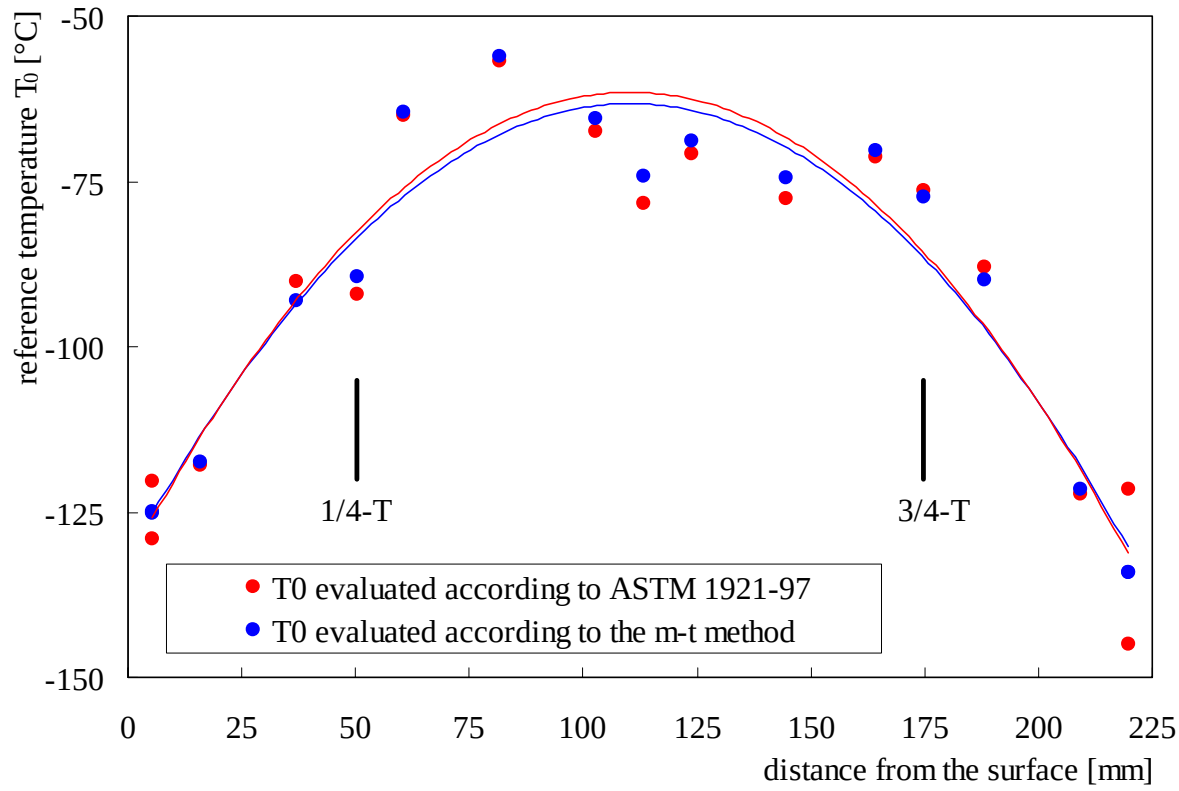

Fig. 2: Reference temperatures T_0 versus the distance from the surface

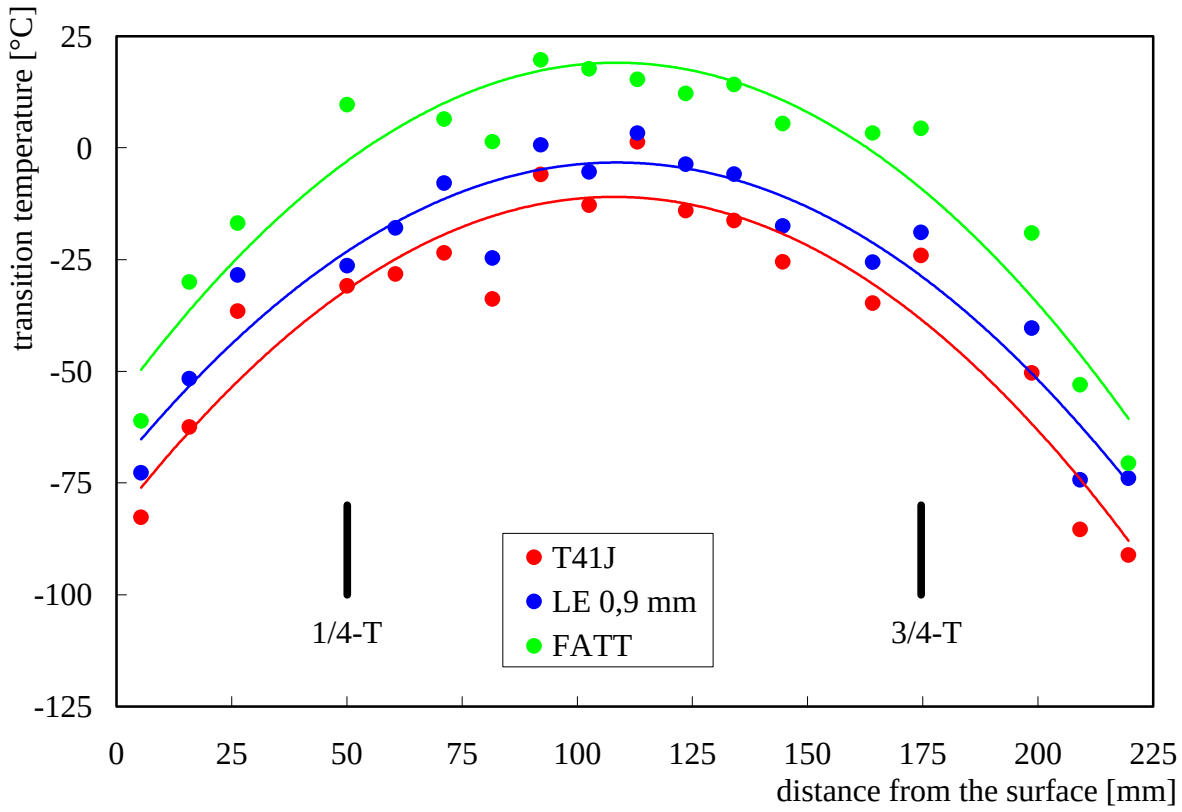

Fig. 3: Charpy V-transition temperatures versus distance from the surface

The course and the scatter of the Charpy V transition temperatures are comparable with T_0 in Fig. 2. There are no significant differences in the course of the scatter for the transition temperatures determined with the different Charpy V parameters (impact energy, lateral expansion and the percentage of shear fracture).

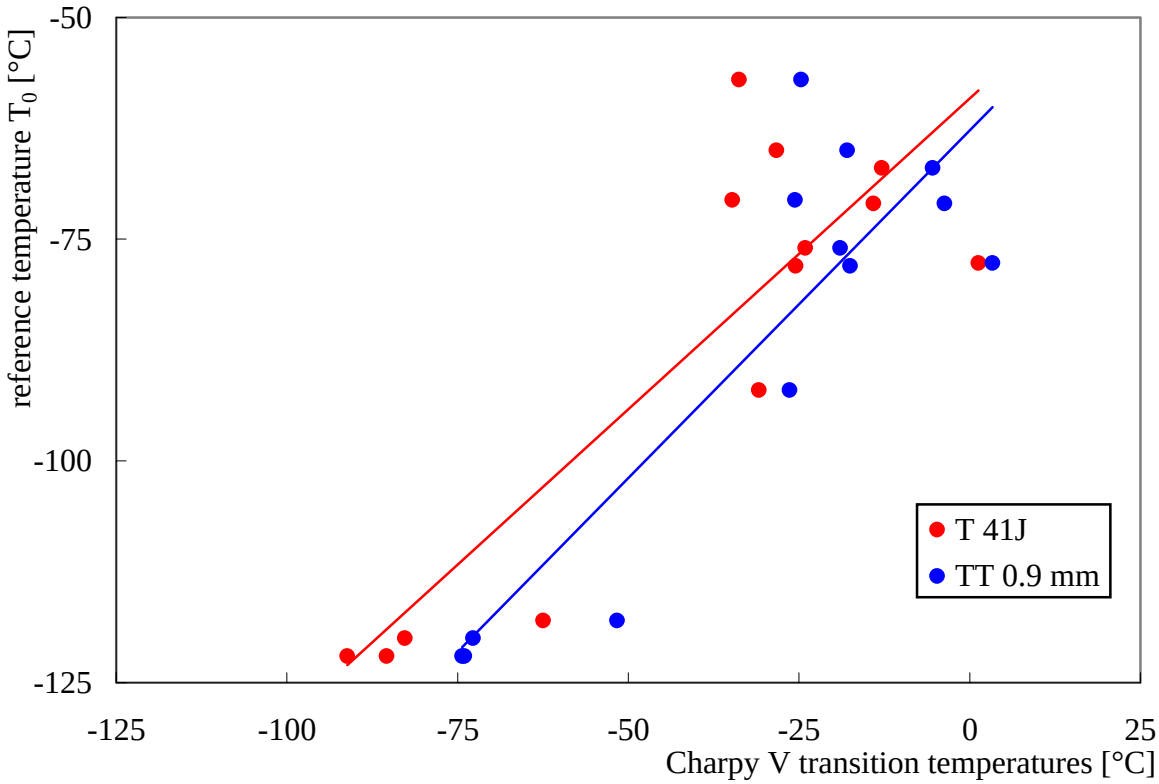

Fig. 4: Correlation between the temperature T_0 and Charpy V transition temperatures

Due to the scatter of the measured values there is no unambiguous correlation between the Charpy V transition temperatures and the reference temperatures T_0 as show in Fig. 4. At almost the same temperature T_0 different Charpy V transition temperatures occur. The bad correlation explains why it was very difficult to meet the right test temperature. The ASTM standard gives an aid to select the suitable test temperature. This aid is based on the Charpy V transition temperature at an impact energy of 28 J minus 50 K for Charpy size specimens. The experience shows that in this way unvalid tests were often obtained.

6. Conclusions

The master curve concept was applied to characterize the fracture toughness in different through-the-thickness locations of a plate of IAEA reference reactor pressure vessel steel. This plate shows an inhomogeneous structure within the inner range.

The following conclusions can be drawn from the test results:

1. The master curve concept is applicable to the fracture mechanical characterisation of structures with different toughness properties within a plate of RPV steel using small test

specimens.

2. A special problem with the use of small specimens is the definition of the test temperature at which fracture toughness values can be determined within the validity limits.

3. It is evident that the reliability of the master curve approach is restricted by the material quality. Inhomogeneously segregated materials provide large scattering in the measured fracture toughness values.

4. The criteria to define the test temperature and the minimum number of specimens for the evaluation of the temperature T_0, as indicated in the ASTM 1921-97 [5] standard is applicable and sufficient only for homogeneous materials.

5. The multi-temperature method offers the possibility to vary the test temperature within one test series. This method should be applied for materials with an inhomogeneous structure.

References

[1] J.G. Blauel, K. Wallin, and G. Nagel (1996), Comparison of Fracture Toughness Curves in the Transition Temperature Regime According to ASME and ASTM, in K. Kussmaul (Ed.), Proceedings of the 22. MPA-Seminar, Safety and Reliability of Plant Technology, Vol. 1, Paper 18, Stuttgart

[2] K. Wallin (1997), Statistical Re-Evaluation of the ASME KIC and KJR Fracture Toughness Reference Curves, in K. Kussmaul (Ed.), 23. MPA-Seminar, Safety and Reliability of Plant Technology, Vol. 1 (pp. 18.1 - 18.20), Stuttgart

[3] K. Wallin (1997), Small Specimen Fracture Toughness Characterisation-State of the Art and Beyond, in B.L. Karihaloo, Y.W. Mai, M.I. Ripley, R.O. Ritchie (Eds.), International Converence of Advances in Fracture Research, ICF 9 (pp. 2333-2344), Amsterdam, 1997

[4] K.-H. Schwalbe, B.K. Neale, and J. Heerens (1994), The GKSS Test Procedure for Determining the Fracture Behaviour of Materials, EFAM GTP 94, GKSS Report GKSS/E/60, Geesthacht.

[5] ASTM 1921-97 (1997), Test Method for the Determination of Reference Temperature, T_0, for Ferritic Steels in the Transition Range, Philadelphia

ANALYSIS OF THE FOREVER-EXPERIMENTS USING A FINITE ELEMENT MODEL

Eberhard Altstadt, Thomas Moessner, Baj Ral Sehgal [1], Hans-Georg Willschütz

1. Introduction

For future nuclear power plants it is demanded that there are no consequences for the environment and the population even in the closest vicinity of the plant during and after every possible accident scenario. This includes the hypothetical scenario of a severe accident with subsequent core meltdown and formation of a melt pool in the reactor pressure vessel (RPV) lower plenum of a Light Water Reactor (LWR). One accident management strategy is to stabilize the in-vessel debris configuration in the RPV as one major barrier against uncontrolled release of heat and radio nuclides. This strategy also applies to existing plants.

To get an improved understanding and knowledge of the melt pool convection and the vessel creep and possible failure processes and modes occurring during the late phase of a core melt down accident the FOREVER-experiments (Failure Of REactor VEssel Retention) are currently underway at the Division of Nuclear Power Safety of the Royal Institute of Technology Stockholm [1]. These experiments are simulating the behaviour of the lower head of the RPV under the thermal loads of a convecting melt pool with decay heating, and under the pressure loads that the vessel experiences in a depressurization scenario (see Fig. 1). The geometrical scale of the experiments is 1:10 compared to a common Light Water Reactor (LWR).

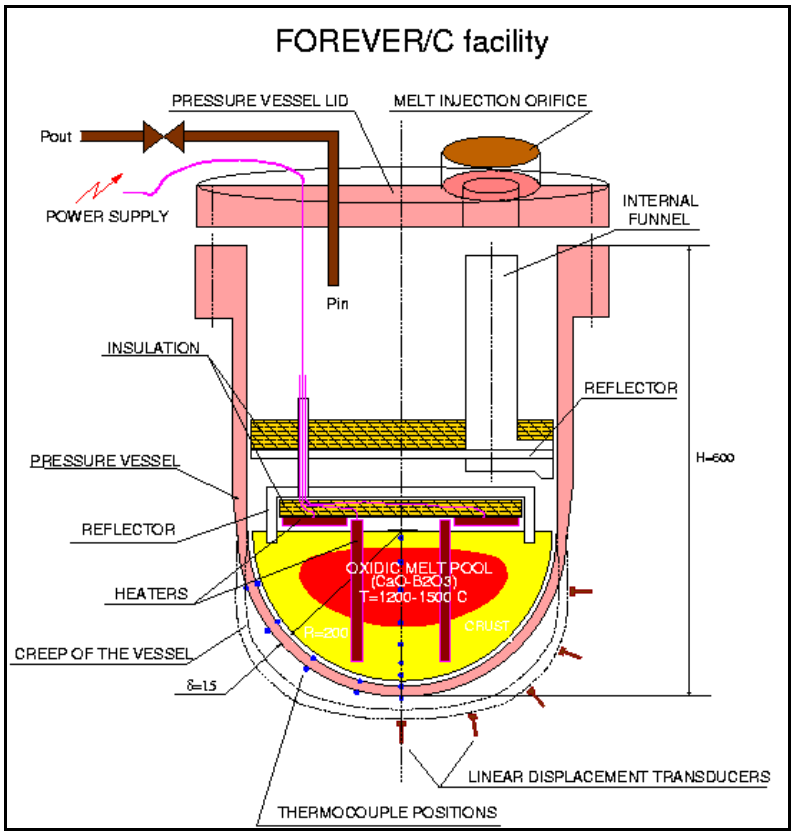

Fig. 1: Principal scheme of the FOREVER/Creep tests. Scheme is not to scale.

During the first series of experiments the creep behaviour (FOREVER-C) of the vessel under the thermal attack of the melt pool and varying internal pressure loads is investigated. It is intended to enforce the creep process until vessel failure. Due to the multi axial creep deformation of the vessel with a non-uniform

[1]Royal Institute of Technology, Division of Nuclear Power Safety, Stockholm, Sweden

temperature field these experiments are on the one hand an excellent source of data to validate numerical creep models which are developed on the basis of uniaxial creep tests. On the other hand the results of pre-test calculations can be used to optimize the experimental procedure with considerations of the uncertainties in the applied models and assumed boundary conditions.

Therefore an axis-symmetric Finite Element (FE) model is developed based on the multi-purpose code ANSYS/ Multiphysics®. Using the Computational Fluid Dynamics (CFD) module the temperature field within the melt pool and within the vessel wall is evaluated. The transient structural mechanical calculations are then performed applying a creep model which takes into account large temperature, stress and strain variations.

Taking into account both - experimental and numerical results - provides a good opportunity to improve the simulation and the understanding of the vessel failure mechanisms. Of particular interest are (i) the time to failure and (ii) the location and mode of failure.

2. Experimental results

The analysis of this work refers to the experiment FOREVER-C2. Due to a rather high heat power input (Q_{max}>40kW) the external temperatures reached more than 900°C in the hot focus region at the upper part of the hemisphere. In consequence a significant creep of the vessel wall was observed. The hemisphere was made of the French RPV steel 16MND5. The applied oxidic melt was a CaO-B_2O_3 mixture (30-70 wt.-%) which has a solidus temperature of T_s=1250K and is a rather aggressive oxide, especially at high temperatures. To model the internal decay heat generation special designed heater rods fixed to an internal insulation-reflector-lid are immersed into the melt from the top. The lid is fixed to the upper part of the vessel. After melt pouring the melt injection orifice in the vessel lid is closed and the vessel inside can be pressurized by Argon. The total duration of the experiment C2 was nearly 10 hours from the start of pre-heating the vessel to the stop of the data recording at the end of the cooldown and relaxation stage. After some 120 min there was a temporarily heater shut down to install additional cooling units to the power supply cables. With the re-gained power supply and temperature level the system was pressurized at t=200min. In Figure 2 the total displacement U_{sum} at different positions of the external vessel surface during the course of the experiment is shown. The thermal expansion of the vessel due to the hot melt pool can clearly be seen. The start of the pressurization indicates

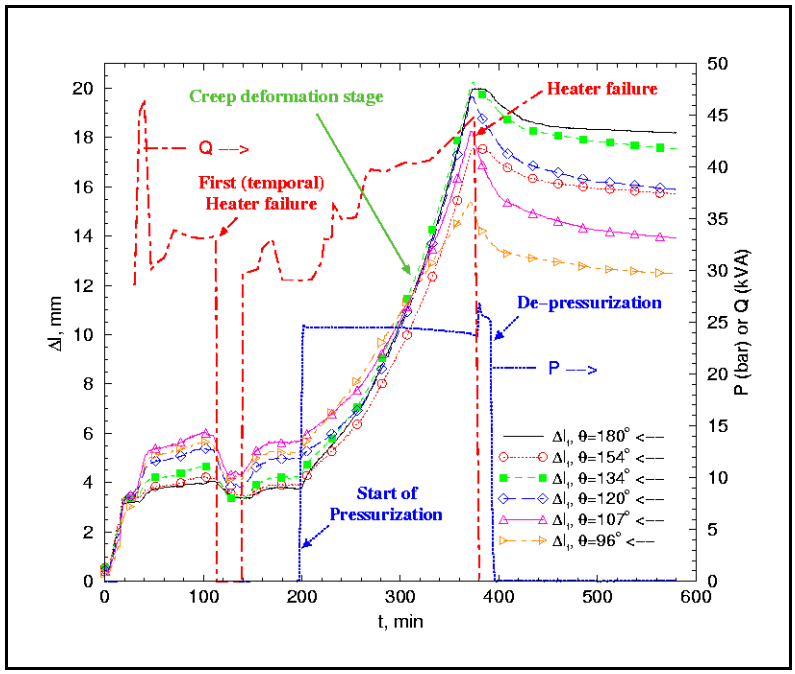

Fig. 2: General course of the experiment C2: power input Q/[kVA], pressure P/[bar] and total displacement U_{sum}/[mm] at different external positions of the hemisphere. Θ = 180° refers to the very bottom.

the beginning of the creep deformation stage. The creep curves show an acceleration of the creep strain which indicates normally tertiary creep. So far the reason for the observations in C2 is not exactly known.

Due to the creep expansion of the vessel the volume of the hemisphere is increasing to the third power of the increase of the radius. This causes a decreasing melt level and as a consequence in the experiment C2 the uppermost parts of the heater rods were no longer immersed in the pool. Therefore they burned out and the power supply was stopped (for a detailed description of the experiment see [1]).

3. CFD analysis of convection and heat transfer

For the evaluation of the temperature field within the vessel wall the CFD-module FLOTRAN® of the FE-code ANSYS® is used. A 2D-axis-symmetric model with appropriate boundary conditions and material properties is developed. A pure homogenous melt pool is assumed inside the vessel with the surface level set to the welding joint between hemisphere and cylinder. The mesh consist of 1740 elements of which 1400 belong to the liquid region at the beginning of the calculation. Due to some prior estimations it was found that the main heat transfer mechanism at the model boundaries is radiation. Therefore at the vessel outside an radiative heat transfer boundary condition is applied with an ambient temperature of T_{amb}=400K. A surface emissivity of e_{steel}=0.8 has been used. Also for the internal surfaces radiative boundary conditions have been modelled: between insulation and melt pool (cf. Fig. 1) T_{amb} was set to 1200K, above insulation it was 800K. The emissivity was the same as on the outside. A homogenous volumetric heat source is assumed which is applied to the volume within which the heaters are to be found. Especially at the very bottom the distance between the heater and the vessel wall has a significant influence to the crust formation. The internal Rayleigh number for this configuration is calculated in a range of $Ra_i=0.5\ 10^{10}$ to $Ra_i=1.0\ 10^{10}$.

To model the heat transfer within the pool the standard k-ε-turbulence model which is provided by FLOTRAN® is used. Assuming slow temperature changes in the vessel wall and in the lower part of the melt pool a dynamic crust is modelled by stopping the solution every 20 seconds and checking the temperature field. For those elements where the melt temperatures are below the solidus temperature of T_s=1250K at all nodes, the material number is changed so that these elements belong to

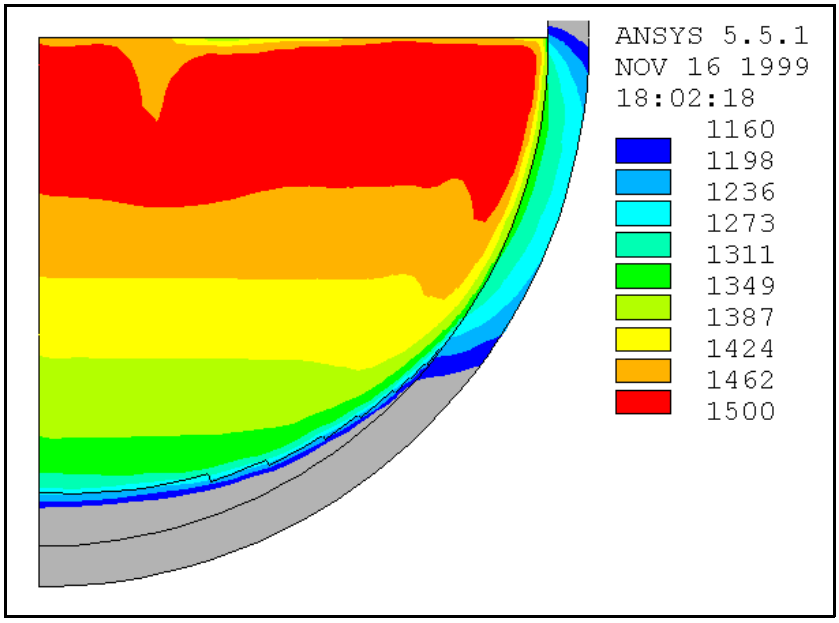

Fig. 3: Calculated temperature field in the hemispherical part with a power input of Q=35kW. T in [K], adjusted scale ranges from 1160K to 1500K, temperatures below 1160K are presented grey.

the solid region of the oxidic crust. So far different power inputs were modelled in transient calculations starting with homogenous initial temperatures within melt pool and vessel wall. The heat generation rates were chosen according to the experimental range which had changed from 30kW to 45kW. In these calculations a thermal steady state for the vessel wall was observed after some 20-30min. The calculated temperature profiles show a good agreement with the measurements in the high temperature region of the vessel. Figure 3 shows the temperature field for the heat generation rate of 35 kW. The melt shows a stable stratification. Therefore, the hottest region of the vessel wall is the upper part of the hemisphere.

4. Structural analysis of the vessel creep

The mechanical 2D-axis-symmetric model of the vessel wall consists of nearly 340 elements and some 410 nodes with 5 element layers over the wall thickness. A sufficient number of elements over the wall thickness is necessary to model the transient body load due to the temperature field which is taken from the CFD analysis.

Because of the large spatial and transient temperature and stress changes within the vessel wall an advanced approach for the numerical creep modelling has been developed. Usually creeping is described by analytical formulas (creep laws) with a number of free coefficients. The coefficients are used to adapt the creep laws to creep test results performed at constant load and temperature. However, it is difficult to achieve a satisfying adjustment for a wide range of temperatures and stresses with only one set of coefficients. Therefore a supplementary tool for the ANSYS code has been developed which allows to describe the creep behaviour of a material for different stress and temperature levels independently. Moreover, it is possible to calculate the creep damage and deactivate elements whose accumulated damage is greater or equal to one. The Digital® Fortran Compiler (Rev. 6.0A) was used for programming and for generating the customized ANSYS-executable on a Windows/NT® platform. The creep data base has been generated using an experimental results analysis performed by [2]. The covered stress range of the data base reaches from σ_{min}=5MPa to σ_{max}=285MPa and the temperature ranges from T_{min}=873K to T_{max}=1373K.

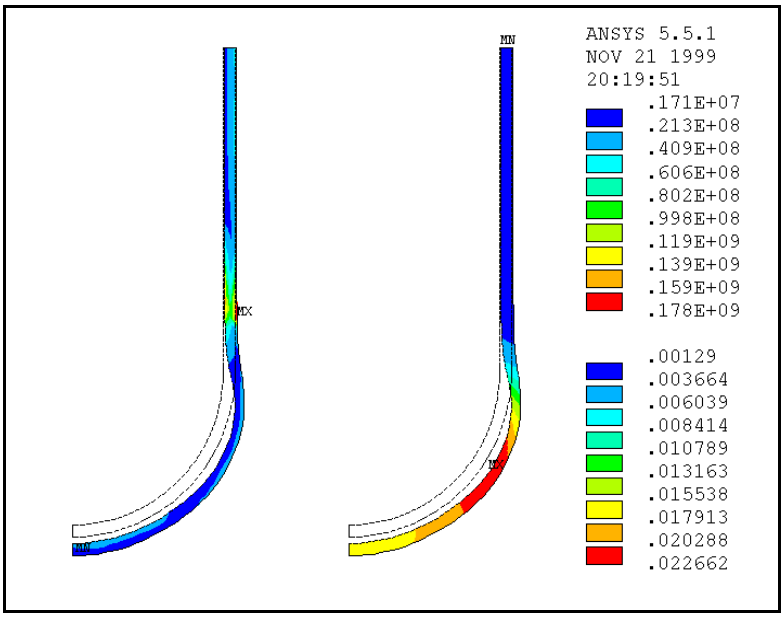

Fig. 4: Von Mises equivalent stress σ_{eqv} [Pa] (left side and upper scale) and total displacement U_{sum} / [m] (right side and lower scale) of the vessel after t=22800s (heater failure in the experiment).

Until pressurization of the system the displacement measured by the linear displacement transducers (LDT) is only due to thermal expansion. Therefore the transient creep calculation starts at the experimental pressurization time of t=12000s (cf. Fig. 5). Figure 4 shows the calculated equivalent stress and

the total displacement at the time 22800s (heater failure in the experiment). If a constant temperature field within the vessel wall is assumed for the transient creep calculation a typical creep curve will be calculated by the code (see Fig. 5, blue curve). This curve is characterized by a steep - but decreasing - increase of creep strain (primary creep stage). After that the creep strain rate becomes nearly constant (secondary creep).

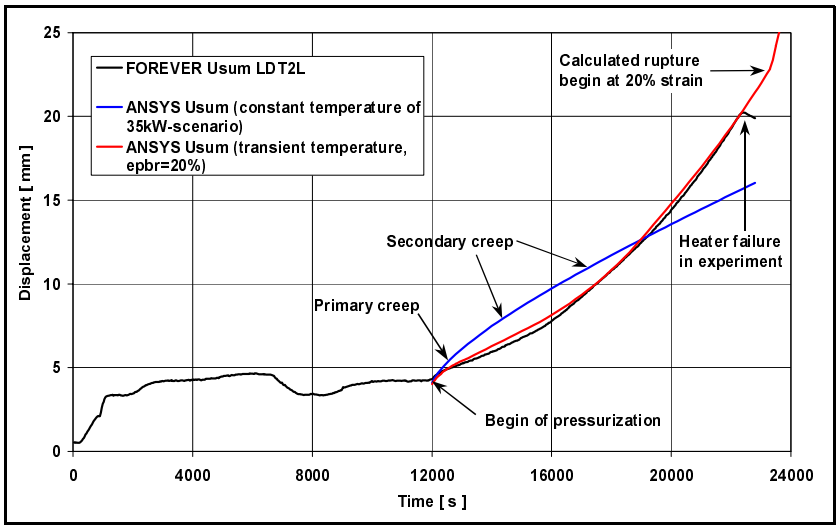

Fig. 5: Total displacement U_{sum} / [m] of the vessel external surface on the left side at position $\Theta = 134°$ over time t / [s].

In fact the total displacement in the experiment (black curve) shows the opposite behaviour to the calculation with constant temperature. The curve looks like a tertiary creep curve, but considering the stress and temperature regimes at this time and the total duration of 3 hours tertiary creep is very unlikely. Performing a transient calculation with a changing temperature field according to the recorded power input (cf. Fig. 2) the calculated creep follows the red curve in Figure 5. This causes a temperature drop at the beginning of the creep deformation stage and a temperature increase after the first half hour until heater failure. Of course this model has to be improved and this will be possible with a temperature field available from a future transient CFD-calculation.

The most interesting question for the next experiments is the vessel failure time. It is not intended to have the vessel failed at the high pressure load. Therefore, different scenarios have to be calculated. In the calculations shown here a slightly increasing heat input is assumed (instead of the unintentional heater failure). Thus the temperature increase has been set to 10K/h and the high pressure load was kept on until vessel failure. With an assumed very conservative creep rupture strain of ε^{frac}=20% for all stresses and temperatures this leads to a vessel failure after t_{frac}=23700s. This means just 15min after the heater failure the vessel would have failed. But considering the uniaxial creep test data of the 16MND5-steel [2] and the results of the Lower Head Failure Tests [3] at the Sandia National Laboratories even a creep

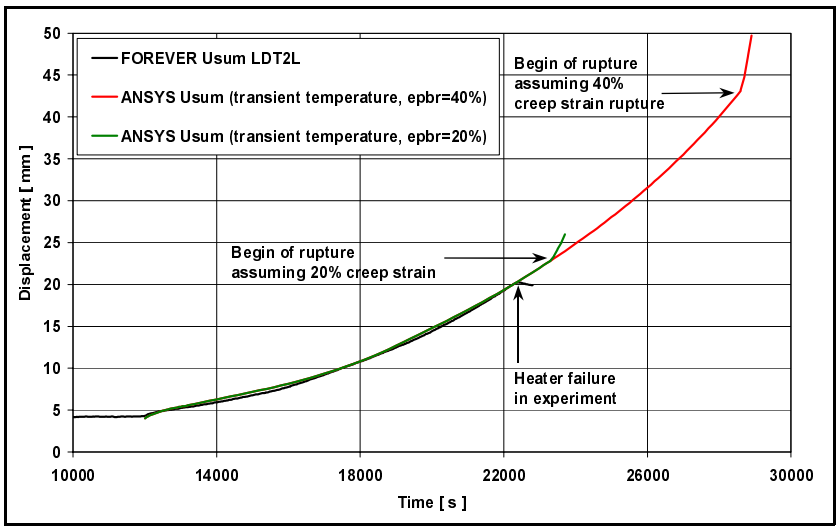

Fig. 6: Estimation of vessel failure time with different creep rupture strains. Total displacement U_{sum} / [mm] of the vessel external surface on the left side at position $\Theta = 134°$ over time t / [s].

rupture strain of ε^{frac}=40% can be stated as conservative. Figure 6 shows the total displacement at Θ=134° for both cases. In the 40%-scenario failure could be expected after t_{frac}=28800s, which means more than one hour after heater failure in FOREVER-C2. Of course, this is a first estimation and further investigations have to be performed.

5. Conclusions

The post test calculations of the FOREVER-C2 experiment show that the behaviour of the vessel - made of French RPV steel - is rather sensitive to temperature changes during the creep deformation stage. Therefore, it seems that the unexpected deformation behaviour during the experiment is caused by the transient temperature field in the vessel wall rather than by a tertiary creep process.

The model will be improved considering the transient thermal boundary conditions which have a great influence to the transient creep calculation. First rupture estimations made clear that one of the main mechanical parameters to be investigated in the future is the creep rupture strain.

References

[1] Sehgal, B.R., Nourgaliev, R.R., Dinh, T.N., Karbojian, A., 1999, "FOREVER experimental program on reactor pressure vessel creep behavior and core debris retention", Proceedings of the 15-th International Conference on Structural Mechanics in Reactor Technology (SMiRT-15), Seoul, Korea, August 15-20, 1999.

[2] Ikonen, K., 1999, "Creep Model Fitting Derived from REVISA Creep, Tensile and Relaxation Measurements", Technical Report MOSES-4/99, VTT-Energy, Espoo, Finland.

[3] Chu, T.Y., Pilch, M.M., Bentz, J.H., Ludwigsen, J.S., Lu, W.Y., Humphries, L.L., 1999, "Lower Head Failure Experiments and Analyses", Report, NUREG/CR-5582, SAND98-2047, Sandia National Laboratories, Albuqerque, NM, USA.

THREE-DIMENSIONAL INTEGRAL NEUTRON TRANSPORT CELL CALCULATIONS FOR THE DETERMINATION OF MEAN CELL CROSS SECTIONS

Carsten Beckert

1. Introduction

To calculate the neutron transport in a reactor, it is often necessary to treat the energy dependence with only a few energy groups. For example the program DYN3D, which has been developed here at the Research Center Rossendorf, computes the dynamics of a reactor in three dimensions. It determines the neutron transport with a diffusion approach and takes into account the energy dependence with two groups. The spatial discretization is done with the nodal method. The volume of the core is divided into height layers. A so created part of a volume of an assembly is called a node. The program assumes that the two group cross sections which determine the transport of the neutrons are constant in each node. So it needs for all nodes and the two energy groups the cross sections for each reaction type. To get these few group cross sections microscopic fine group cross sections are calculated, for example with the program NJOY [1], from evaluated data files. A fine discretization of the node volume is done and a cell calculation is made with the macroscopic fine group cross sections with the Integral Transport Method (ITM). The few group cross sections can be obtained as flux weighted averages over the fine group cross sections. It is assumed in the two-dimensional model, that in the horizontal plane, where the calculation is executed, the nodes continue periodically. The 2D-nodes are assumed to have an infinite height. This is only an approximation for example for the case of inserted control rods. Therefore it is necessary to study a three-dimensional cell calculation with the ITM and to compare it with the two-dimensional one.

Because of these considerations it is the aim to develop a two- and three-dimensional cell program to calculate mean cross sections with the ITM on a uniform data basis and to examine at which assemblies in the core a three-dimensional data preparation is necessary.

A two- and a corresponding three-dimensional cell program, called Transray2d and Transray3d, are being developed for a square lattice. The geometry part was taken from the Monte Carlo program MORSE-CGA [2]. The generals of the theory for the calculation of the mean cross sections and of the fine group fluxes with the ITM in three dimensions is briefly sketched in section 2. The transport equation for the neutron flux is transformed into the integral equation form and with a second equation for the currents, that leave the considered region, one gets a linear system of equations, the collision probability equations. The coefficients are the collision probabilities, which are obtained with the ray tracing method. The linear system is solved with the interface current (IC) method. Finally the fine group fluxes are calculated from the k-eigenvalue form of the transport equation using the inverse power method. Lewis [3] described the theory for two dimensions. Roy, Hébert and Marleau [4] considered the three-dimensional ray tracing, formulated the symmetric IC equations and solved them with an alternate direction implicite (ADI) iteration scheme. In section 3 some remarks are made on the programs Transray2d and Transray3d and a small flowchart of the iteration process is shown. The actual task is the verification of the programs. In section 4 results are

shown of the two-dimensional calculation of a criticality benchmark, the Babcock and Wilcox experiment [5].

2. Theory

2.1 Mean cross sections

In order to describe the exact neutron field with a model that is discrete in space and energy the mean cross sections for the considered region V and energy group G have to be evaluated with a suitable method. An appropriate method to calculate such macroscopic mean cross sections is

$$\sigma_{V,G} = \frac{\int_V dV \int_G dE\, \sigma(\vec{r},E) \int d\Omega\, \Psi(\vec{r},E,\Omega)}{\int_V dV \int_G dE \int d\Omega\, \Psi(\vec{r},E,\Omega)}, \tag{1}$$

where $\Psi(\vec{r},E,\Omega)$ is the exact, but unknown neutron flux. Now the region V and the energy group G are divided into fine groups f and g respectively. The microscopic fine group cross sections are computed from known data files (here with the program NJOY) and together with the nucleus densities of the isotopes the macroscopic fine group cross sections $\sigma_g^{(f)}$ are calculated (here with the program TRANS X). With these cross sections a cell calculation is done for the finely divided region. In this way the fine group scalar fluxes are obtained

$$\Phi_{f,g} = \int_f dV \int_g dE\, \Phi(\vec{r},E), \tag{2}$$

where the scalar flux is $\Phi(\vec{r},E) = \int d\Omega\, \Psi(\vec{r},E,\Omega)$. The mean total cross section can now be written as follows:

$$\sigma_{V,G} = \frac{\sum_{f\in V} \sum_{g\in G} \sigma_g^{(f)} \Phi_{f,g}}{\sum_{f\in V} \sum_{g\in G} \Phi_{f,g}}. \tag{3}$$

2.2 Collision probability equations

To get the fine group fluxes in equation (2) the collision probability equations are formulated assuming isotropic sources and scattering. Considering the time independent transport equation for the neutron flux, doing the energy discretization and looking back along the line with the direction $\hat{\Omega}$ from which the neutrons are coming, one gets the integral equation for the neutron flux in each energy group

$$\Psi(\vec{r},\hat{\Omega}) = \int_0^R q(\vec{r} - R'\hat{\Omega})\, e^{-\tau(\vec{r},\vec{r}-R'\hat{\Omega})} dR' + \Psi(\vec{r} - R\hat{\Omega},\hat{\Omega})\, e^{-\tau(\vec{r},\vec{r}-R\hat{\Omega})}, \tag{4}$$

where τ is the optical path and q the source including scattering, fission and external sources. R is the distance between $\vec{r}$ and the problem domain boundary. Integrating equation (4) over all directions $\hat{\Omega}$ one gets an equation for the scalar flux. Consideration of the outgoing current $J_+(\vec{r}) = \int_{\hat{\Omega}\cdot\hat{n}>0} \hat{\Omega}\cdot\hat{n}\, \Psi(\vec{r},\hat{\Omega})\, d\Omega$ provides a second equation. To obtain the discretized

forms of these both equations, the volume is divided into partial volumes and the boundary into partial surfaces. Taking the spatially averaged values of the fluxes, sources, incoming and outgoing currents over the volumes and surfaces one receives the collision probability equations

$$\sigma_i \, V_i \Phi_i = \sum_{i'} P\left[V_i \leftarrow V_{i'}\right] V_{i'} q_{i'} + \sum_{j'} P\left[V_i \leftarrow S_{j'}\right] S_{j'} J_{-j'} \,,$$

$$S_j J_{+j} = \sum_{i'} P\left[S_j \leftarrow V_{i'}\right] V_{i'} q_{i'} + \sum_{j'} P\left[S_j \leftarrow S_{j'}\right] S_{j'} J_{-j'} \,. \tag{5}$$

$P\,[V_i \leftarrow V_{i'}]$ is the first flight collision probability that neutrons emitted uniformly and isotropically in $V_{i'}$ will have their next collision in V_i, $P\,[V_i \leftarrow S_{j'}]$ is the probability that neutrons entering uniformly and isotropically through $S_{j'}$ will have their next collision in V_i, $P\,[S_j \leftarrow V_{i'}]$ and $P\,[S_j \leftarrow S_{j'}]$ are analogously the escape and transmission probabilities.

2.3 Ray Tracing

The collision probabilities are twofold and fourfold integrals in two and three dimensions respectively, which must be carried out numerically in a general geometry. For example the three-dimensional volume to volume probability is

$$P\left[V_i \leftarrow V_{i'}\right] = \frac{1}{4\pi\sigma_{i'}V_{i'}} \iint d\omega\, d\theta\, \sin\theta \int_{\xi^<}^{\xi^>} d\xi \int_{\eta^<}^{\eta^>} d\eta \left\{ exp(-\tau_{ii'}) - exp(-(\tau_i + \tau_{ii'})) \right. \tag{6}$$

$$\left. - exp(-(\tau_{ii'} + \tau_{i'})) + exp(-(\tau_i + \tau_{ii'} + \tau_{i'})) \right\} \quad \text{for} \quad i \neq i' \,,$$

where ω and θ are chosen as the azimuthal and polar angle describing the direction from where the neutrons are coming. ξ and η set up the plane perpendicular to the direction and the limits on ξ and η are functions of ω and θ. τ_i is the optical path through V_i and $\tau_{ii'}$ the optical path between the volumes. The numerical calculation of these integrals is often referred to as ray tracing. All probabilities are calculated simultaneously by drawing a set of lines (rays) for each direction and assigning the contributions from each line to the corresponding probabilities.

2.4 Interface Current (IC) Method

In the IC method the region that has to be analyzed is divided into subregions and the subregions are coupled with the incoming and outgoing currents of the neighboring subregions. So the equations (5) have to be solved for each subregion. If A is the number of volumes and B the number of surfaces, there are A+B equations and A+2B unknowns (A fluxes and 2B currents). The other B equations are received from the boundary conditions for the incoming currents. Either there is an outer boundary or the boundary is coupled with one of another subregion.

2.5 The k-eigenvalue

In analogy to the physical criticality a system is said to be critical mathematically, if a time-independent nonnegative solution of the source-free, that is no external sources but only the scattering and fission sources exist, transport equation can be found. For the k-eigenvalue form the average number of neutrons per fission ν is replaced by ν/k. There will be a largest value k, for which such a nonnegative solution exists. The system is critical, if this largest value k is equal to 1, subcritical, if k<1 and supercritical, if k>1. The k-eigenvalue form can be expressed in the compact form

$$\boldsymbol{M}\vec{\boldsymbol{\Phi}} = \frac{1}{k}\,\boldsymbol{X}\;\boldsymbol{F}\vec{\boldsymbol{\Phi}}\;, \tag{7}$$

where M is a linear operator, X the matrix with the fission spectra, F the matrix with the fission cross sections and $\vec{\Phi}$ the vector of the group fluxes. The problem of finding the greatest eigenvalue k of the eigenvalue equation (7) is solved with the inverse power method (outer iteration). In this way the fine group fluxes are obtained for this system, which has been made artificially critical with k. Now the averaging in equation (3) can be done.

3. The Program Transray2d and 3d

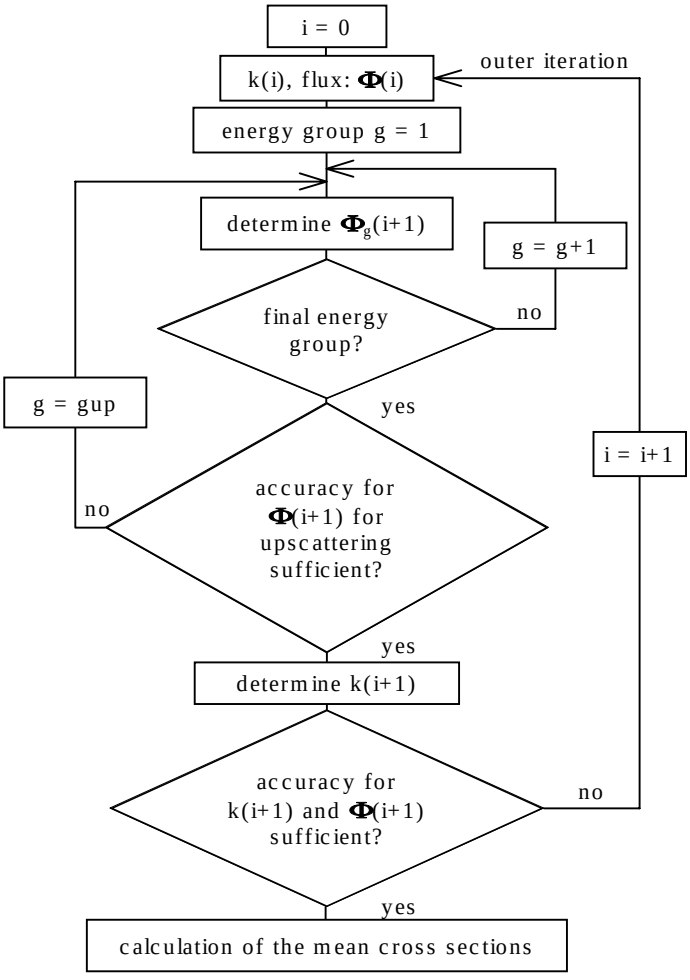

Fig. 1: Flow chart of the iteration process in the program Transray2d and 3d

After drawing the lines through the considered cell the geometry data are calculated for each line and the collision probability matrices are computed. This is done for each cell with or without considering the neighbouring cells. In the three-dimensional program symmetry properties are taken into account for larger problems, for example the assembly of the EPR (European Pressurized Water Reactor) contains a 17×17 rod array composed of 264 fuel rods and 25 guide tubes, 24 for the control rods and one for the instrumentation rod. If a height layer of the whole assembly is used as a cell, storage problems occur. So only a part of collision probabilities is computed and stored due to symmetry considerations.

The iteration procedure to get the fluxes consists of the outer iteration and the inner iterations. The outer iteration is the inverse power method for the determination of the fluxes. All iterations within an outer iteration step are the inner iterations. For the calculation of the fluxes in an iteration step

the elimination of the flux components Φ_i in the equations (5) yields a set of equations for the currents only. These are solved with the Gauss-Seidel method. If upscattering occurs, the Gauss-Seidel method is used too. Thereby the iteration is done from the lowest energy group (gup), where upscattering happens, to the last one. All iterations are stopped, if a maximum number of iterations is reached. Figure 1 shows a flow chart of the iteration process. After reaching convergence the mean cross sections are calculated according to (3).

4. Verification of the 2D-program Transray2d with a criticality benchmark

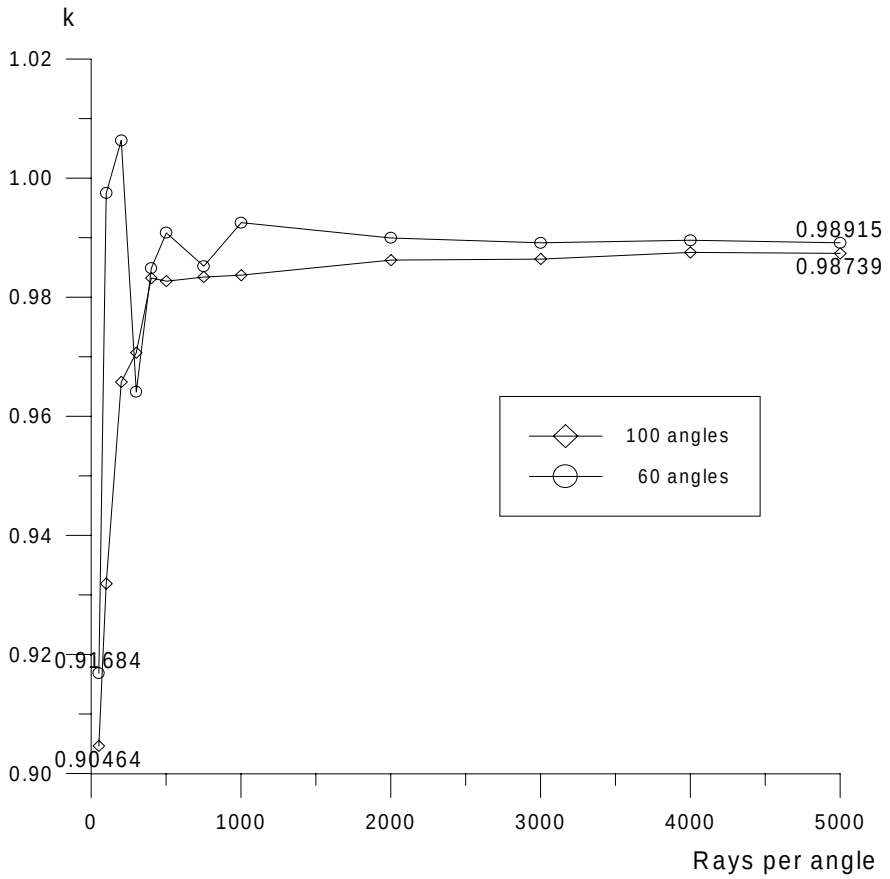

Fig. 2: Computed values of k for the B&W UO_2 experiment with the 2D-program Tranray2d

The Babcock and Wilcox UO_2 (B&W UO_2) experiment was performed at room temperature. The cylindrical UO_2 fuel rods (enrichment 2,5%) were in a square lattice (pitch=1,6256 cm). The clad consisted of aluminum. Criticality was reached adjusting the boron concentration. For the verification of the two-dimensional program the rod geometry pellet without the gap between pellet and cladding was considered. In this case the fuel was smeared into the gap. The value k was calculated with the two-dimensional program with 60 and 100 angles for ray tracing. Figure 2 shows the results for k for different numbers of rays per angle.

Outlook

It is the aim to verify the two- and three-dimensional program and then to compare the mean cross section calculations of both programs for special situations like partly inserted control rods.

References

[1] R. E. MacFarlane, D. W. Muir (1994), The NJOY Nuclear Data Processing System (Version 91), Los Alamos, LA-12740-M

[2] Oak Ridge National Laboratory, RSIC computer code collection MORSE-CGA, Oak Ridge Tennessee (1993)

[3] E. E. Lewis and W. F. Miller, Jr., Computational methods of neutron transport, Wiley-Interscience, New York (1984)

[4] R. Roy, A. Hébert, G. Marleau, A transport method for treating three-dimensional lattices of heterogeneous cells, Nucl. Sci. Eng., 101, 217-225 (1989)

[5] S. Sitaraman, MCNP: Light water reactor critical benchmarks, GE Nuclear Energy, NEDO-32028, March 1992

MONTE CARLO NEUTRON FLUENCE CALCULATIONS, ACTIVATION MEASUREMENTS AND SPECTRUM ADJUSTMENT FOR THE KORPUS DOSIMETRY EXPERIMENT

Hans-Ulrich Barz, Bertram Böhmer, Jörg Konheiser, Ingrid Stephan

1. Introduction

KORPUS is an irradiation facility located at the lateral core surface of the 6 MW experimental reactor RBT-6 in Dimitrovgrad [1]. The knowledge of the absolute space and energy dependent neutron fluences at the KORPUS irradiation positions is eminent for investigations of correlations between material properties deterioration and different types of damage parameters. The large gradient perpendicular to the irradiation rows, frequent changes in the irradiation environment and the necessity to plan the irradiation experiments in advance enhance the need for reliable and precise fluence calculations. Activation measurements are required to prove and adjust the calculation results.

In this work the KORPUS irradiation experiment has been used to demonstrate the capability of the pressure vessel dosimetry methodology developed in Rossendorf to solve these problems. At the same time the experiments were used to test recent improvements of this methodology including a new procedure for treatment of elastic scattering in the Monte Carlo code TRAMO and a new multispectrum version of the adjustment code. By means of a series of calculations the influence of model and data approximations were investigated aiming at an evaluation of the uncertainties of the calculations. Further, uncertainty investigations were carried out in connection with spectrum adjustment resulting in covariances of spectra, measured reaction rates and fluence integrals.

2. Model Description

A detailed three dimensional model was used for absolute calculations of the irradiation facility KORPUS and the RBT-6 reactor. A top view of the calculation model is shown in Fig.1. System boundary is a 15 cm water layer. The temperatures in the core and the facility were 55°C and 45°C respectively. The fuel assemblies of the RBT-6 reactor were homogenised as no data on the inner construction of the assemblies were available. The model includes all known details of the monitor capsules (stainless steel cover, cavity and irradiated steel block with the monitor hole). The capsules without monitors were homogenised. The channels with the FZR-monitors were located in the first (capsule

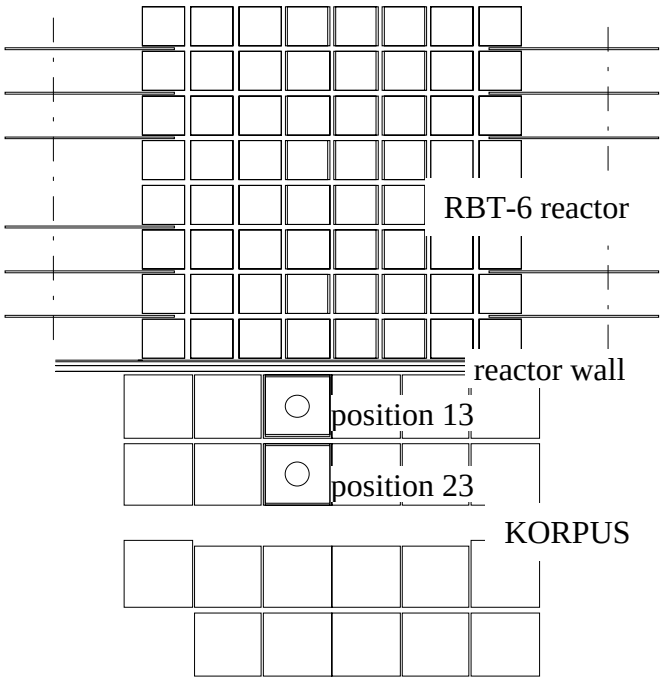

Fig. 1: Top view of the RBT-6 reactor and the KORPUS irradiation facility

13) and second (capsule 23) irradiation rows of the facility (Fig. 1). The vertical position of the monitors was in the middle plane of the reactor. The total neutron source for each assembly was calculated from the given relative power per assembly and the total thermal power. For all assemblies the same relative vertical power distribution was used.

3. Method of Calculation

TRAMO [2] is the main code of a code system, including codes for data preparation (MODAJ), data analysis, and the code TRAWEI for the calculation of space and energy dependent importance functions. This system was developed for the calculation of shielding problems. Recently, the geometrical capabilities were extended and the handling of elastic scattering was improved. The geometrical module now allows to define oblique cylinders and permits different geometrical structures in different horizontal layers. A new procedure for the treatment of elastic scattering using equiprobable angular intervals was included. In contrast to the formerly used Legendre polynomial expansion, the new procedure allows to apply any number of energy groups without loss of accuracy or significant increase of calculation time. This is important for calculations with more than 150 energy groups. It can be shown, that for elastic scattering the P_L-approximation then becomes too poor. Therefore, the P_L-approximation was substituted by angular probability distributions. A comparison for a VVER-1000 reactor pressure vessel [3] showed, that the fluences calculated with the P_L-approximation and a high number of energy groups are somewhat too large. A deterioration of the statistical accuracy is caused by the treatment of the negative differential cross sections connected with the P_L-approximation. Both problems are solved in the new procedure.

The RBT-6 reactor is operated with used fuel elements of the high flux reactor SM-2 with an initial enrichment of 90%. Therefore, the RBT-6 fuel elements contain up to 50% fission product nuclei and the 20 most frequent fission product isotopes were considered explicitely. The nuclear densities of the fission products were obtained by a calculation with the code ORIGEN using the burn-up values given in [2] for each fuel element. Ten different core data sets covering burn-up steps between 7% and 44 % were used in the calculations. The microscopic cross sections including self-shielding factors were calculated with the code NJOY on the basis of the ENDF/B-VI data library.

Unfortunately, no horizontal distribution and only one relative vertical power distribution were given inside the assemblies. Therefore, a linear interpolation in horizontal direction of the relative power values between the middle points of the assemblies was used. Equally probable intervals were created for the x- and y-directions and for each assembly. The same formalism was used in vertical direction. As energy spectrum of the neutron source the U235 fission spectrum was used. This approximation is justified as U235 contributes about 97% to the total number of fissions.

4. Calculation Results

The standard calculations were carried out with 123 groups and the full set of fission products. Position 13 was irradiated at another time than position 23 but with the same burnup and power distribution. Nevertheless, separate calculations for both positions were necessary, as during the second row irradiation the monitor hole in the first row capsule was filled with steel. For representation purposes and for the spectrum adjustment all results have been condensed to a 29 group

structure. For the material irradiation it is important to know the neutron spectrum and its deviation from the spectrum in the RPV. Therefore, the neutron spectra were calculated for central positions in all KORPUS irradiation rows. In Fig. 2 normalized spectra for the first two rows were compared with the spectrum at the ¼ thickness position of a VVER-1000 RPV. We observed a good agreement of the first row spectrum with the RPV spectrum. In the 2nd row the spectrum is too soft and in the 3rd and 4th rows not shown here even softer.

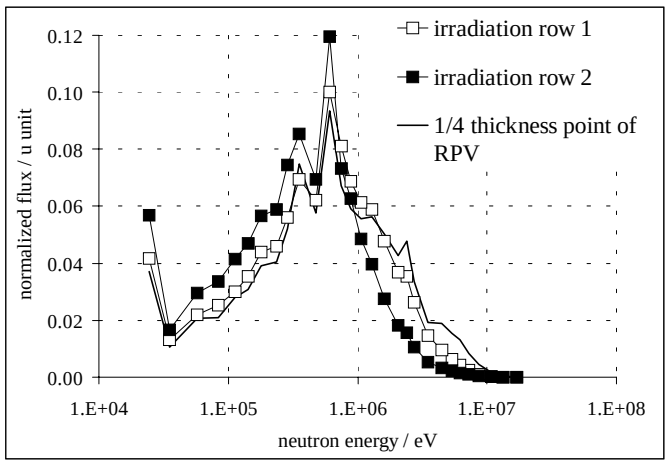

Fig. 2: Comparison of row 1 and row 2 spectra with the RPV spectrum

5. Calculations for Different Model Versions

Calculations with different model versions were compared in order to estimate uncertainties caused by approximations used in the standard calculation or in calculations of other authors neglecting some details of the here applied model. A summary of the results is given in Table 1.

Table 1: Deviations from the standard calculation for dosimetry relevant quantities

	Case A (492 neutron groups)	Case B (without fission prod.)	Case C (fresh fuel elements)	Case D (constant sources)	Case E (horiz. const. Sources)
Total flux	-2.2%	1.0%	-0.3%	1.8%	8.5%
Flux > 1.0 MeV	0.0%	1.5%	0.1%	0.3%	7.5%
Flux > 0.5 MeV	-0.6%	1.2%	-0.1%	1.0%	8.0%
Flux > 0.1 MeV	-2.2%	1.0%	-0.3%	1.6%	8.3%
Nb	-0.1%	1.6%	0.2%	0.5%	7.6%
^{54}Fe	0.9%	2.0%	1.3%	0.0%	6.8%
^{58}Ni	0.8%	1.9%	1.2%	0.0%	6.9%
^{46}Ti	1.1%	2.0%	2.0%	0.1%	6.4%
^{63}Cu	1.0%	2.4%	2.0%	-0.3%	6.5%
Dpa	-1.0%	1.3%	0.0%	1.0%	7.9%

To investigate the influence of the group approximation a calculation with 492 groups (case A) was carried out additionally to a calculation with 123 neutron groups (case B). For simplification, a model without fission products was used for this comparison. As can be seen in Fig. 3 and Table 1 the effect was small.

To investigate the influence of a simplified treatment of the fission products, results of the standard calculation were compared with a calculation without fission products (case B) and with a calculation assuming fresh fuel elements (case C). As can be seen in Fig. 4 and Table 1 the results for case B are at the average about 2% too high due to missing fission product absorption. For case C the differences to the standard calculation are smaller as fission product absorption is compensated by fuel absorption. Generally, the influence of fission products on fluence integrals

and dpa values was obtained smaller than expected.

Finally, the influence of the source distributions inside the fuel assemblies was estimated. Calculation D was carried out with a constant source distribution in both horizontal and vertical directions. The result was surprising. The $\Phi_{E>1.0\ MeV}$ value was identical with the standard calculation value. For $\Phi_{E>0.5\ MeV}$ and $\Phi_{E>0.1\ MeV}$ small differences of 1.0 % and 1.6% were obtained. The reason for that good agreement are compensation effects as the vertical homogenisation of the neutron sources produces a reduction and the horizontal homogenisation an increase of the results. That can be seen from the results of case E where the neutron sources differ from the standard calculation only by the constant horizontal distribution. In this more realistic case the corresponding differences are about 8%. The spectral differences to the standard calculation are shown in Fig. 5.

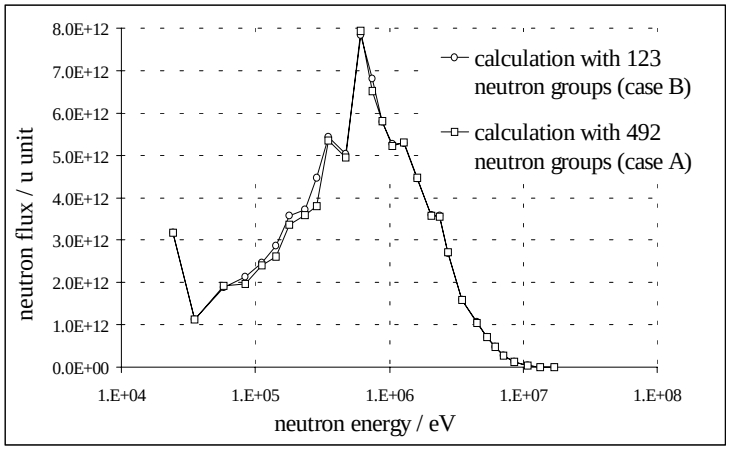

Fig. 3:Spectra calculated with 123 and 492 groups

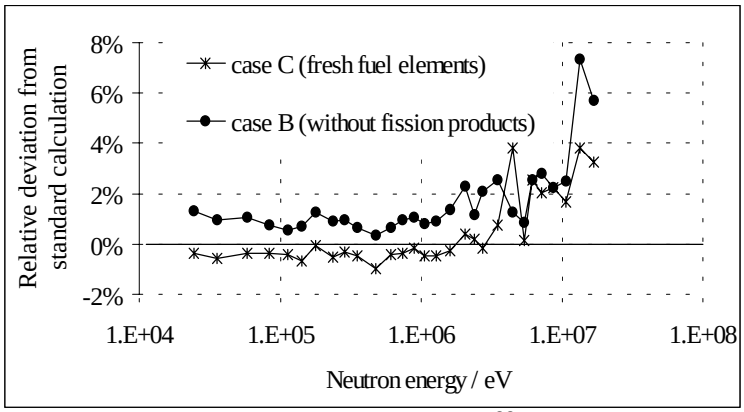

Fig. 4: Spectrum deviations due to different approximations for the fission products

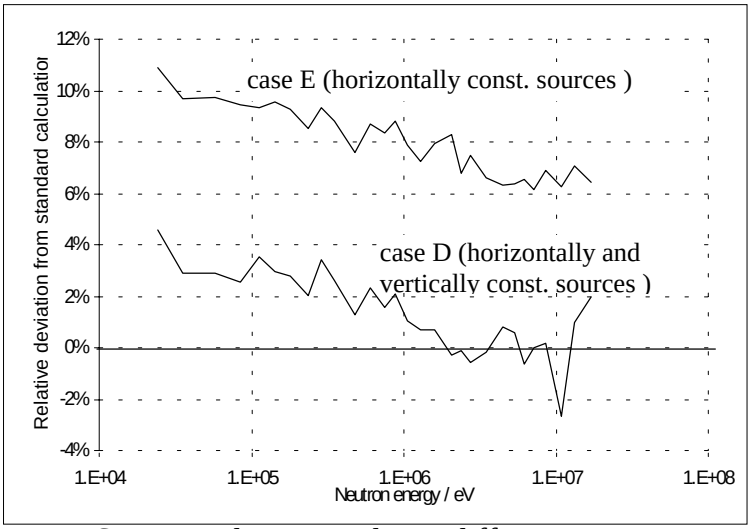

Fig. 5: Spectrum deviations due to different approximations for the source distributions inside assembly

6. Activation Measurements

The first irradiation was performed in capsule 23 between January 16 to 22, 1996 (147 h) and the second irradiation in capsule 13 between April 19 to 23, 1996 (97.38 h). Each ampulle contained 7 detector materials in an argon atmosphere. The following materials were activated: Cu, Nb, Fe, Ag, Co and in multicomponent monitors Ti-Fe-Ni and Ni-Mo-W-Au-Mn. A GMX-2800-Ge-detector including electronics and software was used for the gamma spectrum measurements. The sensitivity distribution over the Ge-detector surface was measured, as this information is important for measurements with a low distance between source and Ge-detector. The gamma transitions were calibrated with sources certified by the

German Calibration Service (DKD). Parallel measurements exist for the first irradiation from ECN Petten and for the second irradiation from SCK CEN Mol. Both results deviate less than 3%. The standard deviations of the measured activities were estimated to approx. 1 – 2%, depending on detector and measurement.

7. Calculation-Experiment Comparison

Reaction rates were derived from the measured detector activities and were compared with reaction rates calculated with absolute spectra, obtained by 123-group standard TRAMO calculations and detector cross sections from IRDF-90/Rev.2. Table 2 presents the ratios between calculated and measured reaction rates.

Table 2: Relations between calculated and measured reaction rate

No.	Position/Measurement	^{93}Nb(n,n')	^{54}FE(n,p)	^{58}NI(n,p)	^{46}TI(n,p)	^{63}CU(n,α)
1	Row1/13-fzr97	0.910	0.973	0.959	0.910	0.953
2	Row2/23-fzr97	0.835	0.925	0.925	0.859	1.018

We observe maximal relative deviations of 10% in the first and 17% in the second row, what is reasonable for absolute calculations. The calculated values are generally lower than the measured ones, especially for the ^{93}Nb(n,n')^{93m}Nb reaction. Possibly this can be explained by too low sources at the core boundary used in the calculation. Probably the 2cm water layer between the core and the first row of capsules caused an increase of the fission rate near the core boundary whereas the calculation assumed a smooth decrease. A similar effect has been discussed by Valenta [3] for the VVER-1000 core boundary.

8. Covariance Analysis

The statistical analysis of the discrepancies between calculation and measurement was based on an adjustment procedure using the multispectrum least squares adjustment code COSA3 [4]. This procedure assumes that all input quantities are characterized by expectation values and covariances. That requires an uncertainty analysis of the input data: reaction rates, calculated absolute spectra and detector cross sections. The detector group cross sections covariances were calculated on the basis of IRDF-90 Rev. 2 by standard methods. The spectrum and reaction rate covariances are more specific for this experiment and more difficult to obtain.

Due to the use of the Monte Carlo method the uncertainties of the calculated absolute fluence spectra are assumed to be caused solely by the input data of the calculation. These are the ENDF/B6-neutron data, the geometrical sizes, nuclear densities, and the neutron source distribution. As even a rough calculation of spectrum covariances is very time consuming and expensive relative standard deviations (RSD), auto-correlation and cross correlation matrices calculated for different locations in a VVER-1000 were taken from [4]. In the VVER-1000, the region near the core with the water cooled steel baffle and the steel shaft resembles the situation between the RBT-6 core and the KORPUS irradiation positions. Therefore two VVER-1000 calculation positions could be selected for which the thicknesses of steel between these positions and the core boundary were the same as the corresponding thicknesses of steel for the row 1 and row 2 KORPUS irradiation positions. The RSD, autocorrelations and cross-correlations obtained for these positions were used for the spectrum adjustment. The RSD of the 29 group spectrum are shown in Table 3. The RSD of the reaction rates used in the adjustment proce-

dure are considerably higher than those of the measured activities due to the uncertainty in the position of the detector in the irradiation capsule and due to an included 4.5% power uncertainty. Especially the last uncertainty component yields high correlations between different reactions and positions. The estimated uncertainties and autocorrelations for position 13 are given in Table 4.

Table 3: Group energy boundaries in MeV and RSD in % of the calculated group spectra

Group	1	2	3	4	5	6	7	8	9	10
E_{low} MeV	.029	.027	.046	.720	.098	.129	.158	.202	.273	.302
Row 1	15.1	15.1	17.6	17.6	18.2	18.2	18.2	18.4	18.4	18.3
Row2	18.9	18.9	19.9	19.9	18.6	18.5	18.5	18.1	18.1	17.9

Group	11	12	13	14	15	16	17	18	19	20
E_{low} MeV	.408	.550	.672	.821	.962	1.16	1.42	1.83	2.31	2.47
Row 1	15.8	15.8	15.4	9.8	9.8	9.6	5.9	5.9	5.9	8.5
Row 2	14.2	14.2	13.8	8.7	8.7	8.6	9.8	9.8	9.8	13.6

Group	21	22	23	24	25	26	27	28	29	30
E_{low} MeV	3.01	4.07	4.97	5.77	6.59	7.79	9.51	12.2	14.5	19.6
Row 1	9.7	12.9	12.9	12.9	16.2	16.2	16.2	23.3	30.2	
Row 2	15.4	19.1	19.1	19.1	21.3	21.3	21.1	26.4	33.0	

Table 4: RSD and autocorrelations of reaction rates for position 13 before adjustment

	RSD %	^{93}Nb(n,n')	^{54}Fe(n,p)	^{58}Ni(n,p)	^{46}Ti(n,p)	^{63}Cu(n,α)
^{93}Nb(n,n')	6.0	1.00				
^{54}Fe(n,p)	5.1	.56	1.00			
^{58}Ni(n,p)	5.2	.56	.83	1.00		
^{46}Ti(n,p)	5.1	.56	.81	.84	1.00	
^{63}Cu(n,α)	5.1	.56	.75	.80	.81	1.00

9. Adjustment Results

Some results of the spectrum adjustment are shown in Fig. 6 and Table 5. Due to the low C/E – values the adjustment leads to an increase of spectrum values and fluence integrals.

Table 5: Fluence integrals and RSD before and after adjustment irradiation time = 4.058 d

Position	$\Phi_{E>0.1MeV}$				$\Phi_{E>0.5MeV}$				$\Phi_{E>1MeV}$			
	before		after		before		after		before		after	
	10^{17} n/cm^2	%	10^{17} n/cm^2	%	10^{17} n/cm^2	%	10^{17} n/cm^2	%	10^{17} n/cm^2	%	10^{17} n/cm^2	%
13	28.83	12	30.81	8	17.71	8	18.71	6	9.73	5	10.12	4
23	6.74	13	7.32	9	3.36	9	3.61	7	1.34	8	1.42	5

At the same time the uncertainties of the spectrum decrease, but less than in earlier spectrum adjustments [5]. That is caused by the relatively high and highly correlated reaction rate uncertainties reflecting the reactor power uncertainty which is actually a component of the spectrum uncertainty.

The main characteristic of the consistency of the data χ^2/n was obtained to 2.79. As χ^2/n has an expectation value of 1 the analyzed data set is not consistent. That indicates that the estimated uncertainties are yet too low. That concerns probably mainly the source data which have higher

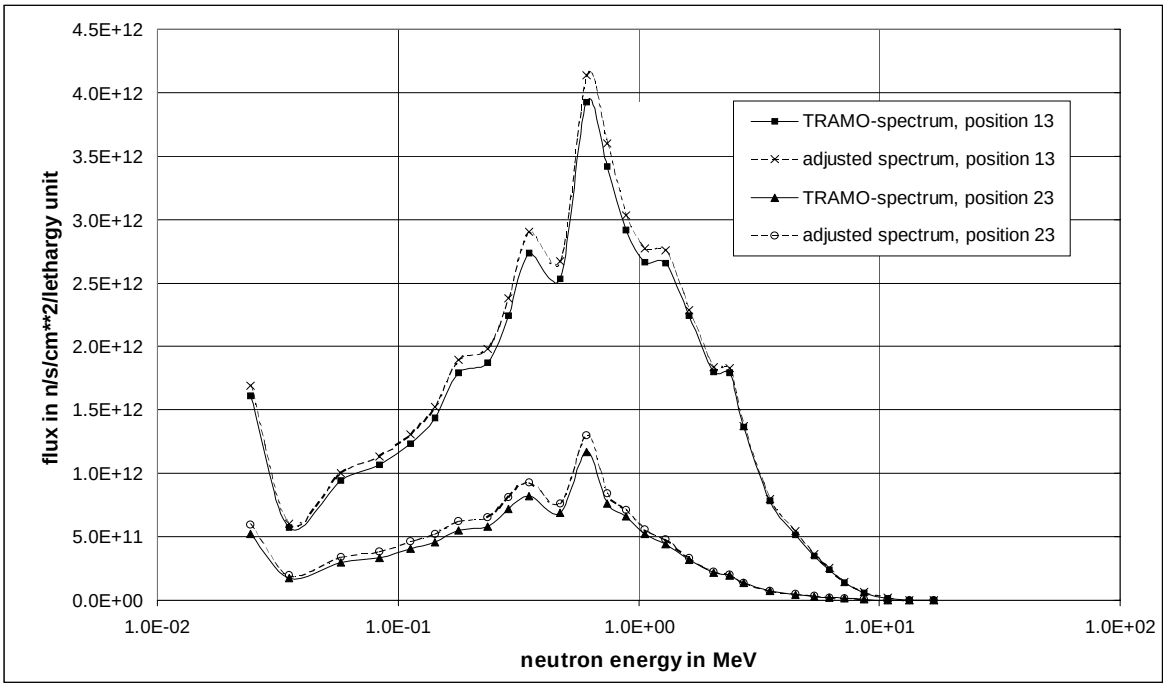

Fig. 6: TRAMO input spectra and adjusted spectra

uncertainties than in the VVER-1000 calculation from where the spectrum uncertainties were derived.

10. Conclusions

It was possible to calculate the absolute fluence values with reasonable accuracy. The main reason for the observed discrepancies between experiment and calculation probably are the incomplete source data, which should be complemented by source distributions inside the outer assemblies. The first row irradiation position was shown to have a neutron spectrum closely resembling the spectrum in the RPV. Multispectrum adjustment proved to be a reliable instrument for combining measurements with calculations, checking their consistency and improving the accuracy of the fluence determination.

References

[1] N. Markina, D. Ryazanov, A.Tellin, V. Lichadeev, V. Pavlov, V. Tsikanov, H. Ait Abderrahim, P. Vanmechelen, A. Paardekooper, W. Voorbraak, H. Nolthenius, T. Seren, I. Stephan, S. Zaritsky, (1998) " International Neutron Dosimetry Characterisation at KORPUS Facility: Inter-Laboratory Dosimetry Calibration Results ", *Proceedings ANS Radiation Protection and Shielding Division Topical Conference ' Technologies for the New Century'*, Vol. 1, p. 316-323, April 19-23, 1998, Nashville, Tennessee, USA, ISBN 0-89448-637-3

[2] H.-U. Barz, J. Konheiser, (1998) Monte-Carlo Programm TRAMO - Möglichkeiten und Anleitung zur Nutzung , *FZR Bericht-245,Rossendorf*

[3] W. Walenta, Z. Fritz, J. Hep, (1989), Vlijanije proizvodstvennych dopuskov i gabaritov konstrukzyionnych detaljei na opredelenije fluensov, Material of. Group L of the International Temporary Collective for VVER, UJV Rez , *private communication*

[4] B. Boehmer, B., G. I. Borodkin, G. N. Manturov, G. N (1999), "Improved Covariance Analysis and Spectrum Adjustment for VVER-1000 Pressure Vessel Fluences*", Proc. 10th Interational Symposium on Reactor Dosimetry*, Sep. 12-17, Osaka, Japan, ASTM STP 1398

[5] H.-U. Barz, W. Bertram, J. Konheiser, I. Stephan (1998), "High-Precision Monte Carlo Calculations, Experimental Verification and Adjustment of Fluences in the Pressure Vessel Cavity of a VVER-1000", *Proceedings ANS Radiation Protection and Shielding Division Topical ' Conference Technologies for the New Century'*, April 19-23, 1998, Nashville, Tennessee, USA, Vol. 1, p. 447-454, ISBN 0-89448-637-3

Summaries of research activities

Accident analysis

U. Grundmann, S. Kliem, S. Mittag, U. Rohde, A. Seidel, as guest scientist: I. Reiche

Development, validation and application of the code complex DYN3D - ATHLET

For the validation of the coupled 3D neutron kinetics/thermohydraulic code complex DYN3D-ATHLET, two international benchmark exercises comprising the analysis of main steam line break scenarios for a VVER-440 type reactor and a Western PWR have been solved. In both exercises, an asymmetrical overcooling in the different coolant loops was initiated. Therefore, the occurence of possible re-criticality of the shut down reactor due to the overcooling connected with positive reactivity insertion significantly depends on the adequate description of coolant mixing inside the reactor pressure vessel.

In the framework of an EU PHARE project under the leadership of FZR with participants from 8 EU and East European countries, measurement data on transients in nuclear power plants with VVER type reactors have been collected and documented. Two transients, the power drop of one generator down to house load level at NPP Loviisa (VVER-440) and turning off one from two working feedwater pumps at NPP Balakovo (VVER-1000), were selected for the analysis using different coupled code systems. For the key parameters, a good agreement between measurements and calculations was achieved. Remaining differences could partially be explained by uncertainties in the input information, like the control rod positions or pressuriser heater set points. It was found, that the correct modelling of the heat transfer in the gas gap between fuel and cladding is significant for the estimation of the fuel temperature Doppler feedback, which influences the change of power level during the transient. As a result of the project, the confidence of the results of the different codes has been improved.

A new nodal expansion method (HEXNEM) was developed and implemented into the code DYN3D. The significantly enhanced accuracy of the neutron flux calculation was shown in benchmark exercises. In co-operation with IPPE Obninsk (Russia), DYN3D was coupled to the internationally widely used thermohydraulic system code RELAP. Accident analysis calculations were performed for the small power, integral reactor concept ABV-67 designed in Obninsk.

supported by BMWi and EU

E. Krepper, F. Schäfer

Validation of thermohydraulic system codes

In the framework of a concerted action on the validation of the thermoydraulic code ATHLET (developed by Gesellschaft für Anlagen- und Reaktorsicherheit), an experiment performed at the Japanese test facility CCTF simulating a large break loss-of-coolant accident with combined cold and hot leg ECC injection was analysed. In this experiment, large counter current flows of water and steam with condensation occur. The analysis aimed at the validation of a new condensation model in ATHLET. In general, the course of the transient was calculated in good agreement with the experiment. However, in the case of high condensation rates in some thermo-fluid dynamics objects,

large oscillations of the vapour volume fraction occur, which lead to high computation times. It was concluded, that the numerical implementation of the new condensation model in ATHLET has to be improved.

Within the co-operation with HEW and TÜV Hannover, ATHLET input decks for German PWRs and BWRs have been modified and extended. The implementation of a cross flow model into the downcomer description of a BWR enables the user to estimate the asymmetrical distribution of the coolant mass flow rate and temperatures in total loss of feedwater scenarios.

supported by BMWi

E. Krepper, A.-K. Krüssenberg, T. Höhne, M. Kliem

Computational fluid dynamics simulations of one and two-phase flow

The experiments on coolant mixing in PWRs in the ROCOM test facility have been accompanied with CFD simulations. Experiments with the injection of plugs of a tracer fluid (salt water) into a steady state flow field or during the start-up of circulation have been analysed. These experiments simulate a temperature or boron concentration perturbation in one of the loops. Even the transport of the tracer in the complex instationary flow field during the start-up of the circulation was well reproduced in the calculations. The agreement between experiment and calculation was significantly improved, if the measurement data are averaged from experiments repeated under the same conditions. This is due to the fact, that fluctuations of the flow field observed in the experiments are partially damped in the calculations.

Using the CFD code CFX-4.2, experiments carried out at the Rossendorf two-phase flow test loop were numerically simulated. Velocity and void fraction profiles of water and air flows were measured with different gas and liquid superficial velocities in a vertical tube using high resolution two-phase instrumentation (wire mesh sensor). Taking into account different forces acting on the bubbles, radial velocity and void fraction profiles were calculated. Flow regimes showing a maximum of the void profile near the wall of the tube were well simulated with CFD. For flows with a higher part of larger bubbles, a maximum of the void distribution in the centre of the tube is observed. This was not reproduced in the calculations using the Euler/Euler approach. It was shown by a detailed simulation of one single large bubble, that it oscillates around the centre of the tube. This must be reflected in the description of the forces acting on the bubbles also in the Euler/Euler approach.

partially funded by BMWi (know how conservation program)

CFD simulations of a loss-of-vacuum accident in a fusion reactor were performed. Velocity, pressure and temperature distributions after air penetration into the vacuum were calculated. It was a special challenge to simulate the super-sonic air flow after opening of the leak.

Thermo-fluiddynamics

A. Böttger
G. Grunwald
T. Höhne
H.-M. Prasser
K.-H. Richter
J. Zschau

Coolant mixing in pressurised water reactors

The work aims at the determination of temperature and boron concentration distributions at the core entrance during main steam-line breaks and deboration transients. Experiments were carried out at the mixing test facility ROCOM modelling the German KONVOI type pressurised water reactor in the scale of 1:5. The disturbance is modelled by injecting salt water as a tracer into the affected loop. A new quality of tests is achieved by using mesh-sensors with numerous measuring positions in the downcomer and at the core entrance, the high measuring frequency (up to 200 Hz), the variability of the four-loop test facility and the direct comparison to CFD calculations. The mixing in the pressure vessel is incomplete. In case of running coolant pumps, the tracer arrives almost completely in the sector of the core that belongs to the disturbed inlet nozzle, the most affected fuel element receives about 90 % of the initial disturbance. Strong fluctuations of the tracer concentration are observed at the slopes of the tracer distribution. The mixing of short plugs is promoted by the non-uniform distribution of the travelling time in the downcomer, caused by large-scale vortices. The maximum observed concentration decreases with decreasing plug length. The injection of the tracer during the start-up of the coolant circulation leads to a maximum opposite to the angular position of the disturbed inlet nozzle.

A. Böttger
U. Hampel
F. Hensel
D. Hoppe
H.-M. Prasser
J. Zschau
C. Zippe
W. Zippe

Development and calibration of two-phase flow measurement techniques

The qualification of the diversified level indication system for boiling water reactors developed by FZR was started according to the German reactor safety regulations. The qualification procedure and the series production will be accomplished by an industrial supplier of measurement instrumentation. FZR contributes as a scientific consultant.

Partner:
TELETRONIC GbR
funded by: AiF

A new generation of signal acquisition units for the wire-mesh sensors for high-speed visualisation of two-phase flows was developed. The measuring frequency was increased from previously 1,200 to 10,000 frames per second. This results in a significant improvement of the resolution. The wire-mesh sensor is now capable of resolving individual bubbles in several successive frames at higher flow velocities (≈ 10 m/s). This is important for the investigation of the transition from slug to annular flow.

funded by BMWi

In co-operation with the Technical University of Nishny Novgorod (Russia) a new ultrasonic mesh sensor was developed. The sensor is based on a system of crossing ultrasonic wave-guides. It is complementary to the electrical wire-mesh sensors of FZR, because it can be applied to non-conducting fluids. The dimensions of the wave guides were decreased to minimise the disturbance of the flow.

funded by DFG

For the investigation of transport processes in bubble columns and foam layers, a PET detector is under construction. The scanner will allow to measure the distribution of a tracer marked by a positron emitting nuclide with a time resolution of better than 1 s. It consists of 8 axial layers with 16 BGO detectors each. The spatial resolution will be in the range of a centimetre. The mechanical construction of the detector arrays and the development of the signal acquisition circuitry was finished. The licence for operating the scanner with open radioactive sources was obtained. First tests are expected for the near future.

funded by SMWK

In co-operation with the Technical University Dresden, the development of a stroboscopic gamma-tomograph for an axial turbo pump was started. The work aims at the measurement of the gas fraction field inside the rotating impeller, when the pump is working in two-phase flow mode.

T. Kern
D. Lucas
H.-M. Prasser

Basic studies of two-phase flows with foam production

Needle probes were used to characterise the axial gas fraction distribution in foams. A method was developed to measure bubble sizes and the number of bubbles per unit volume in experiments with wet unstable foams of aqueous solutions of different alcohols. It is based on the analysis of the time derivate of the probe signal. The main goal is the development of coalescence models for wet unstable foams. Furthermore, a 10 l reactor of the Technical University Hamburg/ Harburg was equipped with needle probes to measure the transient axial gas fraction distribution during depressurisation tests with foaming liquids.

A. Grahn

Thermoconvection and instabilities at the boundary layer of two non-miscible liquid reacting components

Flow instability at the inter-phase surface between two non-miscible liquids were investigated for the cases of non-reactive mass transfer (extraction) and exothermal reactions at the phase boundary. Experiments were carried out in a capillary gap equipped with a shadowgraph set-up. A numerical model for the two-dimensional flow in the gap was developed, which considers the chemical reaction, the thermal and concentration effects on the fluid density and the surface tension. The model is capable of predicting all types of experimentally observed instabilities (density driven circulation cells, double-diffusive fingering regimes, Marangony type instabilities). The quantitative agreement concerning wave lengths and growth rates must be further increased.

D. Lucas,
E. Krepper,
H.-M. Prasser,
A. Schaffrath,
C. Zippe,
W. Zippe

Transient two-phase flows in pipelines

The wire-mesh sensor was used to study the transient flow pattern in an air-water flow in a vertical pipe. The superficial velocities of both phases were varied in a wide range, so that bubble, slug and annular flow regimes were covered. The evolution of the flow pattern along the vertical pipeline was studied by increasing the axial distance between air injection and sensor. Bubble size distributions were obtained from the

sensor data. The development of these distributions along the tube length allow to quantify the effects of both bubble coalescence and fragmentation. Furthermore, a new data evaluation method was developed to obtain gas fraction profiles for distinct classes of the bubble size. In a realistic turbulent two-phase flow, it was shown that the direction of the lateral motion of bubbles depend on the bubble size. The lift force acting on bubbles in the boundary layer changes its sign when the bubble diameter exceeds about 5-6 mm. This confirms theoretical findings for the motion of a single bubble known from literature.

On the basis of the experimental results, the development of a one-dimensional theoretical model of the behaviour of a large number of bubble classes was started. It describes the flow along the vertical pipe for a given bubble size distribution at the inlet. The model contains constitutive equations for bubble coalescence and fragmentation. For the calculation of the radial profiles of velocity and gas fraction, a second 1D model was elaborated, which considers all important fluid forces acting on the gas bubbles in dependence on the bubble size. The profiles are calculated under the assumption of quasi-stationary conditions, i.e. it is assumed that each bubble is in equilibrium concerning the acting forces.

funded by BMWi

Materials and Components Safety

J. Böhmert, A. Ulbricht, M. Grosse

Microstructural analyses of irradiated model Fe alloys

The effect of copper, phosphorus and nickel on the radiation embrittlement was investigated using an irradiation experiment at surveillance positions in two Russian VVER-type reactors with 8 iron based alloys. As well Charpy-V impact and tensile tests as small angle neutron scattering experiments were performed with specimens from these alloys. The specimens were tested in the as-received state, in the irradiated state (fluence $1x10^{19}$ and $8x10^{19}$ n/cm^2 [E > 0.5 MeV]) and in the post-irradiation annealed state.

Irradiation produces strong hardening and embrittlement. The effect increases with Cu and P content. Ni causes an additional embrittlement, which is superimposed to the effect due to Cu and P. The effect can be eliminated by annealing at 475°C/100h but not totally in the case of high Cu or P content.

Small angle neutron scattering measurements show that not only the volume fraction but also the type of the radiation defects varies in dependence on the composition of alloys. Independent on the Ni content, the volume fraction of irradiation defects increases with increasing Cu content. P has no influence. The fluence dependence of the irradiation defects differs for Cu-containing and Cu-free defects.

supported by BMWi

H.-W.Viehrig, J. Böhmert, H. Richter

Evaluation of the irradiation behaviour of Russian pressure vessel steels from the irradiation programme Rheinsberg

Different charges from VVER-type reactor pressure vessel steels were irradiated in the VVER-2 Rheinsberg. Four charges from 15Kh2MFA, two charges from 15Kh2NMFAA and one charge from 10KhGNMAA weld metal were tested by FZR. Testing comprises Charpy-V impact tests and quasi-static 3-point bending tests. In this way ductile-brittle transition temperatures and J-integral related fracture toughness according to the Master curve concept were determined. All charges show a good toughness in the initial state and meet the Russian standards. Irradiation shifts both the transition temperature determined by Charpy tests and the T_o reference temperature determined by the Master curve concept. The shift of the reference temperature T_o is higher than the shift of the Charpy transition temperature. The results permit to estimate the irradiation embrittlement coefficient. Based on that, shifts of the transition temperature were predicted in the range of 20° to >220°C for a 25-years reactor life. Whereas a shift of 20°C proves a very low irradiation sensitivity, values of more than 200°C cannot be accepted. The embrittlement can be, however, remedied by thermal annealing at 475°C/100h as shown by annealing experiments. The differences of the irradiation sensitivity for the different charges are not only due to composition effects, but also due to different textures.

supported by BMWi

H.-W. Viehrig, H. Richter

Reconstitution techniques qualification & evaluation to study ageing phenomena of nuclear pressure vessel materials

The assessment of the ageing behaviour of structural components especially of the nuclear reactor pressure vessel (RPV) requires material parameters. In some situations only small quantities of the material of interest are available. The technique of constructing specimens from small quantities of material is commonly called 'reconstitution'. The construction of compound specimens is achieved by attaching additional material (studs) around a material of interest - the insert material - to prepare a test specimen of standard dimensions.

An EU project was performed to stepwise qualify, verify and compare two different reconstitution techniques: stud-welding and electron-beam welding. The project aimed at identifying the limits of applicability of technical reconstitution parameters that have the potential to affect the experimental values measured with reconstituted specimens: i.e. the material and the insert length, the welding procedure, the heat input, the weld seam quality and strength. Two types of specimens that are most frequently used in RPV assessment were considered: Charpy V-notch impact and precracked Charpy size specimens for fracture toughness. The initial emphasis was put on un-irradiated material. Afterwards the optimum reconstitution procedure was verified with irradiated RPV steels.

The overall analysis of the data gathered from all project partners was summarised in a document that could serve as a European Code of Practice for the reconstitution of irradiated Charpy V-notch impact and Charpy size fracture toughness specimens.

supported by EU

H.-G. Willschütz, E. Altstadt

In-vessel retention of core melt

To get an improved understanding of the processes occurring during the late phase of a core melt down accident the FOREVER-experiments at the Royal Institute of Technology (Stockholm) are currently underway. These experiments are simulating the behaviour of the RPV lower head under the thermal loads of a convecting melt pool with decay heating and simultaneous pressure loads. The geometrical scale of the experiments is 1:10 compared to a common Light Water Reactor. Due to the multi axial creep deformation of the vessel with a non-uniform temperature field these experiments are on the one hand an excellent source of data to validate creep models for different pressure vessel steels. On the other hand the results of pre-test calculations can be used to optimize the experimental procedure. At FZR a finite element model is developed. Using the computational fluid dynamics module the temperature field within the melt pool and within the vessel wall is estimated. Transient structural mechanical calculations are performed applying an advanced creep model which takes into account large temperature, stress and strain variations. Post test calculations of the FOREVER-C2 experiment were performed. If the temperature field in the vessel wall is fixed along the creeping process, the calculated creep curves disagree with the measurement. Considering the variation of the temperature field, the calculated results show a good agreement with the measurements.

T. Repp

Waterhammers in pipelines

The pressure waves induced by a sudden slow down of the fluid flow in a pipe line are modelled using the finite element method. Special attention is put on the influence of fluid-structure interaction if the pipe diameter is relatively large in comparison with the wall thickness. The transient velocity and pressure distribution are calculated for a straight pipe and a 90° elbow assuming a slightly compressible fluid. The coupling between the elastic pipe wall and the fluid is realized by boundary elements. It is shown that there are local stresses in the elbow which are higher than those calculated with conventional uncoupled calculations. It was found that also pressure waves in radial direction occur. The radial waves are induced by the elastic deformation of the pipe (change of diameter). A test facility for waterhammer experiments has been built up (pipe diameter 200 mm), thus in 2000 a validation of the finite element simulation will be possible.

supported by VDEW

Simulation of Particle and Radiation Fields

B. Böhmer, J. Konheiser

Neutron and gamma dosimetry of reactor pressure vessels

The BMWi project „Influence of the gamma irradiation on the deterioriation of reactor pressure vessel materials and on reactor dosimetry measurements“ was started. Input data for neutron-gamma transport calculations for two Russian and two German reactor types have been collected. First calculations of neutron and gamma fluences and damage parameters for VVER-type reactors were performed in cooperation with Russian scientists.

As contribution to the EU TACIS project “Embrittlement Studies of the Reactor Pressure Vessel of the Greifswald-440 Reactors” neutron fluence and dpa-values for the inner and outer reactor pressure vessel walls, 10 angular and 10 height intervals were obtained for the whole lifetime of the Greifswald units 1 to 4 and for the operation time since vessel annealing (unit 1). Based on these data suitable positions for taking trepans during the planned Greifswald trepan investigation project could be proposed.

B. Böhmer, J. Konheiser

Increasing the accuracy of neutron and gamma fluence calculation

The Rossendorf Monte Carlo code TRAMO is being upgraded. The geometrical module now allows to define oblique cylinders and permits different geometrical structures in different horizontal layers. A new procedure for the treatment of elastic scattering using equiprobable angular intervals was included. In contrast to the formerly used Legendre Polynomial expansion, the new procedure allows to use any number of energy groups without loss of accuracy or significant increase of calculation time.

Fluence calculations for two irradiation positions in the KORPUS irradiation facility were performed with TRAMO using different versions of reactor models and numbers of energy groups. Comparing the results obtained with different versions the uncertainties of fluences caused by model deficiencies and group approximations could be evaluated. They were found to be smaller than 10%. A comparison between measured and calculated activation reaction rates and an adjustment of the calculated fluence spectra to the measured reaction rates has been carried out with the code COSA3. The calculations and measurements agreed within the error boundaries.

In cooperation with Russian scientists, space-dependent spectrum covariance matrices including the correlations between group fluences at different spatial locations were calculated for the ex-core region of a VVER-type reactor. Unexpected high positive correlations were found between fluences at different ex-vessel cavity detector positions. The calculated covariance matrices were used to test the new multi-spectrum adjustment code COSA3 developed from the code COSA2.

K. Noack, A. Rogov

Design of the neutron/gamma shields for the experiments PANDA and STRESS-SPEC at the FRM-II

In addition to the plan the neutron/gamma shields of the PANDA and STRESS-SPEC experiments at the new research reactor FRM-II has been designed on the base of results of neutron/gamma transport calculations performed with the Monte Carlo code MCNP. The PANDA spectrometer and the STRESS-SPEC diffractometer will be equipped and operated by the Technical University Dresden and by the Hahn-Meitner Institute Berlin, respectively. The tasks consisted in finding a technically feasible design of the shields which within the frame of given maximum geometric extensions must meet the demand that on the

outer surface a prescribed maximum value of the total biological dose is not exceeded. Additionally, among the possible solutions of this problem an optimisation had to be performed considering the following conditions:

– to minimise the cost of the shield,
– to minimise the weight of the shield and
– in case of PANDA the maximum possible use of nonmagnetic material in the neighbourhood of the measurement equipment.

The optimum solutions were defined and serve as the base for the engineering design of the shields which is under way.

R. Küchler, K. Noack

Model calibration and verification of radionuclid transport

A computer code has been developed to simulate the reactive transport of various chemicals in the unsaturated soil. For the calibration and verification of the code and of its mathematical models the following data from a natural field are necessary: chemical concentrations, rate constants of minerals and equilibrium coefficients of the involved chemical reactions. However, field data can be obtained only with great expenses so that they are often replaced by data from column experiments. Therefore, it is planned to perform systematic model experiments with unsaturated columns to verify the modelling of the diverse processes by the code. The construction of the column experiments is running parallel to the development and verification of hydraulic measurement techniques. The following preparatory works for the experiments were carried out:

- determination of hydraulic parameters of beach sand.
- measurement of the water distribution in the unsaturated columns at constant irrigation.
- automatisation of the data acquisition from the columns

The evaluation of the column test data will be based on the complete one-dimensional mathematical migration model. The elaboration of this model is in progress.

R. Koch

Calculation of effective two-group cross-sections

The neutron and gamma transport code HELIOS for lattice burnup in general two-dimensional geometry was implemented and tested under the operation system SunOS 5.3. In order to test the implementation and the processing code, the well known benchmark assembly of Babcock and Wilcox was used. The influence of different geometrical models was studied. The code was used to prepare two-group libraries of macroscopic cross sections for different loading pattern of the European Pressurized Reactor. These data can be used with the code DYN3D for the analysis of transient processes in nuclear reactors.

Safety and effectiveness of chemical processes

G. Hessel,
H. Kryk,
W. Schmitt,
T. Seiler,
F.-P. Weiß

Environmentally safe process control and state diagnostics in chemical plants using neural networks

The work aims at the development of a neural-network approach to the diagnosis of discontinuous chemical processes in a production plant.
To obtain scalable state features, a scaling model based on energy balances is being developed so that this method could also be used in geometrically dissimilar reactor vessels of different volumes. Scaling studies conducted in laboratory reactors and a pilot plant showed that very accurate measurements of process and plant variables are necessary to extract suited features for the state classification. For example, the industrial plant has to be equipped with sensors for the accurate measurement of the cooling power.

Moreover, the kinetic investigation of a complex three-phase hydrogenation has been completed to be able to apply the neural-network approach to monitoring of heterogeneous reactions. A specific procedure for a quantitative High Performance Liquid Chromatography (HPLC) analysis was developed to improve the modelling of the complex hydrogenation process by means of concentration profiles. The HPLC analysis revealed that two intermediates can play a role during the hydrogenation of an aromatic nitro compound.

supported by BMBF

G. Hessel,
H. Kryk,
W. Schmitt,
N. Tefera, ,
F.-P. Weiß,
T. Willms

Experiments and numerical simulations of exothermic chemical reactions

A two-years research program ”Grignard reactions” was started in co-operation with the Arzneimittelwerk Dresden (AWD). The molar reaction enthalpy of a Grignard reaction was measured in a closed reaction calorimeter as a function of temperature. The investigation of the spontaneous behaviour has shown that the initiation of the Grignard formation can be detected by a Fourier-Transform Infrared (FTIR)-spectro-meter much earlier than by using the temperature or the pressure signals. Further, by dosing the organic halide with different feed rates, reproducible induction times as a function of the concentrations were obtained, what is very important for a safe initiation (i.e. without runaway) of Grignard reactions.

The institute took part in the international benchmark DAKAPO (data acquisition by calorimetry for polymerisation reactions) and has in this way broadened the scope of activities by including polymerisation reactions. The benchmark aimed at establishing a standard polymerisation reaction and at the assessment of the accuracy of the calorimeters. The evaluation of the benchmark is still pending.

In the framework of an industrial contract, different exothermic polycondensation reactions (production of phenolic resin and expoxy resin) were studied regarding their hazardous potentials. The thermokinetic parameters obtained by calorimetric measurements are needed to design the cooling system for safe operation of poly-

condensation processes in a production plant. Besides thermal stability screening measurements carried out in a Differential Scanning Calorimeter (DSC), calorimetric profiles of these polycondensation reactions were recorded under similar operating conditions like in the production plant.

supported by industry

Liquid Metal Magnetohydrodynamics

V.Galindo, I.Grants, G.Gerbeth, T.Jung, A.Cramer, S.Eckert, Yu.Gelfgat, A.Bojarevics, D.Batic

Magnetic field applications in crystal growth and metallurgy

Numerical codes have been developed and used for melt flow and heat transport calculations of crystal growth problems. For the industrial Czochralski growth of silicon commercial codes were used in order to simulate the melt control by means of different magnetic fields. The calculations were compared with model experiments and real growth experiments of silicon single crystals. Parameter regions have been identified where the growth process and the grown crystal show clear improvements. Meanwhile the corresponding magnetic systems are successfully introduced into industrial growth facilities.

For simulations of transport phenomena and magnetic field influences on growth processes in ampulla an own spectral code was developed. These results are compared with InAs growth experiments performed at Bergakademie Freiberg where a rotating magnetic field is installed in order to enhance the convective transport within the melt.

In cooperation with the Fraunhofer institute IFAM-Dresden the stabilization of an inductively stirred melt surface by means of an external magnetic field was studied. The goal of that work is to improve the melt extraction process for the production of thin metallic fibres. The magnetic field leads to a serious stabilization of the melt surface which improved the process significantly. A model experiment has been built up using the lower melting fluid SnPb in order to study the effects at the wheel meniscus in more detail. Measurements with a high-speed camera show that the oscillating meniscus has a strong influence on the diameter distribution of the extracted fibres. The model experiments demonstrated that by means of special magnetic fields in the vicinity of the melt meniscus a significant reduction of the mean diameter and of the diameter distribution width can be obtained.

supported by DFG, SMWK, industry

Model experiments have been performed with a rotating magnetic field of variable frequency. The flow velocity driven by this field shows a significant maximum at some specific field frequency.

F.Stefani, A.Gailitis, G.Gerbeth, T.Gundrum

The Riga Dynamo experiment

The theory of magnetic field generation in cosmic bodies due to the homogeneous dynamo effect has been widely elaborated during the last decades. However, an experimental verification of this effect was missing until recently. At the Riga dynamo facility, self-excitation of a magnetic field in a liquid metal flow has been observed for the first time in November 1999. For increasing rotation rate of the driving propeller,

the amplification of an applied magnetic field has been measured. At the highest rotation rate of 2150 rpm, an exponentially increasing 1.3 Hz signal has been detected on the background of the amplified 1 Hz signal. Additionally, after switching off the excitation current, a slowly decreasing eigenmode was observed at the lower rotation rate of 1980rpm. The results correspond convincingly with numerical predictions.

supported by DFG

T.Weier, G.Mutschke, U.Fey, V.Avilov, G.Gerbeth

Electromagnetic boundary layer control for saltwater

The flow of saltwater around bodies can be controlled by electromagnetic forces localized directly on the surface of the body even though the elctromagnetic forces penetrate only slightly into the low-conducting fluid. With suitable arrangements of electrodes and permanent magnets Lorentz forces can be produced which for instance accelerate the fluid motion parallel to the body surface. This results in a stabilized flow, drag reduction of the body, and prevention of flow separation. All these effects have been convincingly demonstrated during experiments performed at the Shipbuilding Test Basin Hamburg in a saltwater flow. For example, the flow around a hydrofoil has been kept separationfree at angles of attack where the usual flow shows vortex separation. This is accompanied by a lift increase of about 90%.

supported by VDI and DFG

W.Witke, S.Eckert, T.Gundrum, G.Gerbeth

Measuring techniques for liquid metals

Liquid metals are non-transparent, typically hot and aggressive. There is almost no commercial measuring technique available for a determination of local velocities or pressure. A mechano-optical velocity probe was developed which is able to measure two components of local velocities. It is calibrated and tested in different melts like InGaSn, SnPb, SnBi or PbBi. The measuring principle consists in the velocity induced elongation of a glass rod which is encapsulated in a glass capillary. This elongation is then measured by optical means using an endoscope and a camera. Due to its measuring principle the probe is independent of any electromagnetic fields. It is now developed and tested up to temperatures of about 700°C.

Several successfull tests have been performed applying an ultrasound velocitymeter to liquid metal flows. Together with the primary producer of that system and some potential users from industry a European project proposal has been set up in order to further qualify this system for higher temperature applications up to liquid steel.

supported by DFG

J.Priede, V.Shatrov, G.Gerbeth, Yu. Gelfgat

Levitation of metallic samples

Electromagnetic levitation is a well-known method in order to support and fix metallic samples without any contact to some wall. However, these samples typically show a strong tendency to instabilities resulting in serious rotation or oscillation of the body. The physical reason of such spontaneous instabilities has been identified as being due to the finite skindepth of the levitator field. Frequency dependent threshold for the occurence of these instabilities have been calculated as main results of the theoretical investigations. Model experiments were performed

clearly confirming the theoretical results. Based on these investigations a method to stabilize the levitated samples by means of steady magnetic fields is developed. This method shall now be transfered into the existing levitation facilities with DASA-Dornier.

supported by DARA

Publications

Publications in scientific and technical journals and in conference proceedings

Altstadt, E.; Ohlmeyer, H.; Otremba, F.; Weiß, F.-P.
Elastic plastic finite element analysis of a BWR feed water distributor exposed to an extreme pressure load
15-th International Conference on Structural Mechanics in Nuclear Technology (SMIRT-15), Seoul, Korea, August 15-20, 1999, Proceedings Vol. VII pp. 177-184

Altstadt, E.; Ohlmeyer, H.; Otremba, F.; Weiss, F.-P.
Finite element analysis of a BWR feed water distributor under extreme transient pressure load
7th International Conference on Nuclear Engineering (ICONE-7), April 19-23, 1999, Tokyo, ICONE-7073

Altstadt, E.; Weiss, F.-P.
Finite element-based vibration analyses of WWER-440 type reactors
Nuclear Technology, Vol. 128 (1999) p. 46-57

Altstadt, E.; Weiss, F.-P.
Finite-element based vibration analyses of WWER-440 type reactors
Annals of Nuclear Energy, Vol 26 (12), 1999, pp. 1037-1052

Anikeev, A. V. et al.; Noack, K.
Study of Hot-Ion Plasma Confinement in the Gas-Dynamic Trap
26th EPS Conference on Controlled Fusion and Plasma Physics
Maastricht, The Netherlands, 14-18 June 1999, Proceedings Vol. 23J, pp. 1781-1784

Anikeev, A. V.; Noack, K.; Otto, G.
Numerical Studies of Neutron Distributions in GDT Experiments
26th EPS Conference on Controlled Fusion and Plasma Physics
Maastricht, The Netherlands, 14-18 June 1999, Proceedings Vol. 23J, pp.1497-1500

Aszodi, A.; Krepper, E.; Prasser, H.-M.
Investigation of heating up and evaporation processes of fluids in storage tanks by experiments and by numerical simulation
2nd International Symposium on Two phase Flow Modelling and Experimentation
Pisa, May 1999 Proc. Vol. III, pp. 1667-1674

Aszodi, A.; Krepper, E.; Schaffrath, A.
Numerical Simulation of the Emergency Condenser of the SWR1000
Ninth International Topic Meeting on Nuclear Reactor Thermal Hydraulics (NURETH-9), San Francisco, California, October 3 - 8, 1999, (Conference CD)

Bagryansky, P. A.; Bender, E. D.; Ivanov, A. A.; Karpushov, A. N.; Murachtin, S. V.; Noack, K.; Krahl, St.; Collatz, S.
Effect of Fast Ti-Deposition on Gas Recycling at the First Wall and on Fast Ion Losses in the GDT Experiment
Journal of Nuclear Materials 265 (1999) 124 -133

Beyer, M.; Carl, H.; Schumann, P.; Seidel, A.
Fernüberwachung ukrainischer Kernkraftwerke (in Russisch)
Atomnaja Technika sa rubeshom, Nr.8 (1999), page 3-8

Böhmert, J.; Große, M.; Ulbricht, A.
Nanoscale Precipitates in VVER-440-type Reactor Pressure Vessel Steels after Irradiation and Annealing
Third International Ural Seminar, Radiation Damages Physics of Metals and Alloys, Abstracts, 21-27 February 1999, Snezhinsk, Russia, p. 32

Böhmert, J.; Kryukov, A.; Nikolaev, Yu. A.; Erak, D. Yu.
Einfluss von Kupfer, Phosphor und Nickel auf die Neutronenversprödung von Eisenlegierungen
Jahrestagung Kerntechnik 1999, Karlsruhe, 18.-20. Mai 1999, Tagungsbericht, S. 663 ff.

Böhmert, J.; Müller, G.; Viehrig, H.-W.
Einfluss von Seigerungen in dickwandigen Teilen aus Druckbehälterstählen auf die Zähigkeitskennwerte
Tagung "Gefüge und Bruch", Internationale Werkstoffprüftagung, 17.-19. März 1999, Bochum, Vortrag Nr. 19

Böhmert, J.; Uhlemann, M.
Consideration of Environmental Degradation of Reactor Pressure Vessel Steels for the Safety Assessment
International Conference on Environmental Degradation of Engineering Materials, EDEM 99, 19.-23.09.1999, Gdansk-Jurata, Poland, 167-174

Cramer, A.; Bojarevics, A.; Gerbeth, G.; Gelfgat, Yu.
Stabilisation of the melt extraction process with a magnetic field
accepted at: El-Kaddah (Ed.): Fluid Flow Phenomena in Metals Processing, TMS, San Diego (USA)

Dudlik, A.; Prasser, H.-M.; Schlüter, S.
Visualization of cavitating liquid flow behind fast acting valve
ECCE 2 - Second European Congress of Chemical Engineering - Montpellier 05.-07.10.1999, paper CDROM 11270003.pdf.

Eckert, K.; Grahn, A.
Plume and finger regimes driven by an exothermic interfacial reaction
Physical Review Letters 82, 31 May 1999, Number22, 4436-4439

Fey, U.; Weier, T.; Lammers, G.
Elektromagnetische Grenzschichtkontrolle - Experimente an der Hamburgischen Schiffbauversuchsanstalt
Statusseminar "Technische Anwendungen von Erkenntnissen der Nichtlinearen Dynamik", Frankfurt, 23./24.02.1999, Tagungsband S. 205-208

Fiorini, G. L.; Friesen, E.; Van der Hagen, T.; Lopez Jimenez, J.; Meloni, P.; Rindelhardt, U.
BWR Physics and Thermohydraulics Complementary Actions to the IPSS - BWR R&D Cluster
Proc. of the FISA-99 Symposium on EU Research in Reactor Safety, Luxembourg, 29 November - 1 December 1999, p. 682

Grants, I.; Gerbeth, G.
Linearized solution of quasi-steady Stefan problem in vertical gradient freeze configuration
Journal of Crystal Growth Elsevier 207 (1999) 138-147

Grundmann, U.
HEXNEM - A Nodal Method for the Solution of the Neutron Diffusion Equation in Hexagonal Geometry
M&C'99 - Madrid, Proc. of the International Conference on Mathematics and Computation, Reactor Physics and Enviromental Analysis in Nuclear Applications, pp. 1086-1094, Madrid, 27 - 30 September,1999

Grundmann, U.
3D Nodal Expansion Method HEXNEM for Solution of the Neutron Diffusion Equation in Hexagonal Geometry
Jahrestagung Kerntechnik 1999, Karlsruhe, 18. - 20. Mai, Tagungsband S. 15 - 18

Grundmann, U.; Hollstein, F.
A Two-Dimensional Intranodal Flux Expansion Method for Hexagonal Geometry
Nuclear Science and Engineering 133 (1999) 201-212

Grundmann, U.; Kliem, S.; Rohde, U.
Analysis of the Exercise 2 of the OECD - MSLB Benchmark with the Code DYN3D/R
M&C'99 - Madrid, Proc. of the International Conference on Mathematics and Computation, Reactor Physics and Enviromental Analysis in Nuclear Applications, pp. 1794-1803, Madrid, 27-30 September 1999

Hessel, G.; Schmitt, W.; Tefera, N.; Weiß, F.-P.; Neumann, J.; Deerberg, G.
Identifikation und Bewertung prozeßrelevanter Zustände in Semibatch-Reaktoren mit neuronalen Netzen
DECHEMA-Jahrestagungen '99, Jahrestagung Sicherheitstechnik, 27. - 29. April 1999, Wiesbaden, Band II, S. 143

Hessel, G.; Schmitt, W.; Vorst, K. van der; Weiß, F.-P.
A Neural Network Approach for Acoustic Leak Monitoring in the VVER-440 Pressure Vessel Head
Progress in Nuclear Energy, Vol. 34, No. 3, pp. 173 - 183, 1999

Höhne, T.
Numerical Simulation of the Coolant Flow in Pressurized Water Reactors
CFX International Users Conference, Friedrichshafen, Germany 19-24 June 1999, CD-ROM, No. 27

Höhne, T.
Numerical Simulation of the Coolant Mixing in Pressurized Water Reactors
Jahrestagung Kerntechnik 1999, Karlsruhe,18.-20. Mai, Tagungsband S. 139

Höhne, T.; Rohde, U.; Weiss, F.-P.
Experimental and numerical investigation of the coolant mixing during fast deboration transients
9th AER symposium on VVER reactor physics and reactor safety, October 4-8 1999, Dämenovska Dolina, Slovakia, Proceedings pp. 327

Hoppe, D.
Ein akustisches Verfahren zur Klassifizierung von Füllständen
Technisches Messen 66 (1999) 6, S. 244-247

Ivanov, Kostadin N.; Grundmann, U.; Mittag, S.; Rohde, U.
Comparative Study of a Boron Dilution Scenario in VVER Reactors
Annals of Nuclear Energy 26 (1999) 1331-1339

Kliem, S.; Danilin, S.; Kyrki-Rajamäki, R.; Hadek, J.; Kereszturi, A.; Siltanen, P.
A Benchmark for Coupled 3D Neutron Kinetics/Thermohydraulics System Codes - Main Steam Header Break in a NPP with VVER-440 Reactor
Proc. International Conference on Mathematics and Computation, Reactor Physics and Environmental Analysis in Nuclear Applications (MC '99), vol. 1, pp. 359-368, Senda Editorial, S.A., Madrid (Spain)

Knebel, J.; Grötzbach, G.; Lischke, W.; Rohde, U.; Schaffrath, A.
Technische Sitzungen der Sektion 2 (Thermo- und Fluiddynamik) der Jahrestagung Kerntechnik 1999
atomwirtschaft - atomtechnik 44 (1999), Heft 7, S. 419-423

Krepper, E.
Natural circulation experiments at the ISB-VVER Integral Test Facility and Calculations using the Thermal-Hydraulic Code ATHLET
Ninth International Topical Meeting on Nuclear Reactor Thermal Hydraulics, San Francisco, California, October 3-8, 1999, (Conference CD)

Krepper, E.
Pre- and Posttest Calculations to Natural Circulation Experiments at the Integral Test Facility ISB-VVER Using the Thermalhydraulic Code ATHLET
Nuclear Engineering and Design 190 (1999) 341-346

Krepper, E.; Krüssenberg, A.-K.; Prasser, H.-M.; Schaffrath, A.
High Resolution Void Fraction Measurements for the Validation of Flow Maps and CFD Codes
2nd International Symposium on Two phase Flow Modelling and Experimentation, Pisa, May 1999, Proc. Vol. III, pp. 1371-1378, ISBN: 88-467-0177-1

Krepper, E.; Prasser, H.-M.
Measurements and CFX-Simulations of a Bubbly Flow in a Vertical Pipe
CFX International Users Conference, Friedrichshafen, 21.-24.6.1999 (Conference-CD)

Krepper, E.; Schäfer, F.
Post-Test Analysis of the BETHSY 9.3 Experiment- Steam Generator Tube Rupture with Failure of both the High Pressure Safety Injection and Auxiliary Feedwater Systems
Jahrestagung Kerntechnik 1999, Karlsruhe, 18.-20. Mai 1999, Tagungsbericht S. 103-106,

Krepper, E.; Schäfer, F.
Post-Test Analysis of the Experiment 5.2c- Total Loss of Feedwater at the BETHSY Test Facility
Jahrestagung Kerntechnik 1999, Karlsruhe, 18.-20. Mai 1999, Tagungsbericht S. 99-102

Krepper, E.; Schaffrath, A.; Aszódi, A.
Numerical Simulation of the Emergency Condenser of the SWR1000
Kerntechnik 64 (1999) 5-6, p. 243-252

Krepper, E.; Willschütz, H.-G.; Altstadt, E.; Weiß, F.-P.
Using ANSYS/FLOTRAN® and CFX-4® for the solution of a mixed convection flow benchmark
17. CAD-FEM Users´ Meeting, 6.-8. Oktober 1999, Sonthofen, Germany, Proceedings Paper No. I 2.4

Krepper, E.; Willschütz, H.-G.; Weiß, F.-P.
Calculation at a Mixed Convection Flow Benchmark Using Different CFD Codes
Jahrestagung Kerntechnik 1999, Karlsruhe, 18.-20. Mai 1999, Tagungsbericht S. 135-138

Krepper, E.; Willschütz, H.-G.; Weiß, F.-P.
Finite Volume and Finite Element Code Calculations to an IAHR-Benchmark Test
7th International Conference on Nuclear Engineering (ICONE-7), Tokyo, April 1999, Conference CD, ICONE-7072

Krüssenberg, A.-K.; Schaffrath, A.; Prasser, H.-M.
A New Criterion for the Bubble Slug Transition in Vertical Tubes
Ninth International Topical Meeting on Nuclear Reactor Thermal Hydraulics (NURETH-9), San Francisco, 5th Oct 1999, CD-ROM

Lucas, D.
A new one-dimensional Particle-In-Cell model for multiphase vessel flow
Journal of Thermal Sciences 38 (1999) 758-768

Lucas, D.
BRICK - a 1D tool for transient multiphase vessel flow simulations based on a new particle method
2nd International Symposium on Two-Phase Flow Modeling and Experimentation, Pisa, May 23-25, 1999, Volume 3, pp. 1657-1664

Lucas, D.
BRICK - Ein 1-D Simulationstool für Mehrphasenströmungen in Behältern
Chemie Ingenieur Technik 71 (1999) 713-717

Moormann, R.; Alberici, S.; Hinssen, H.-K.; Krüssenberg, A.-K.; Wu, C. H.
Oxidation Behaviour of Carbon-Based Materials Used for High-Temperature Gas-Cooled Reactors and Fusion Reactors
Advances in Science and Technology, Vol 24 (1999) 331-8

Mößner, R.; Gerbeth, G.
Bouyant Melt Flows Under the Influcence of Steady and Rotating Magnetic Fields
Journal of Crystal Growth, Vol.197, pp.341-354, 1999

Mutschke, G.; Avilov, V.; Gerbeth, G.
Elektromagnetische Grenzschichtkontrolle - Theorie und Numerik
Statusseminar "Technische Anwendungen von Erkenntnissen der Nichtlinearen Dynamik", Frankfurt, 23./24.02.1999 Tagungsband. S. 201-204

Neumann, J.; Deerberg, G.; Schlüter, S.; Schmitt, W.; Hessel, G.
Early Detection and Identification of Undesirable States in Chemical Plants Using Neural Networks
Keil, F., Mackens, W., Voß, H., Werther, J. (eds): Scientific Computing in Chemical Engineering II - Simulation, Image Processing, Optimization and Control, Springer-Verlag Berlin, Heidelberg, New York, 1999, S. 380-387

Prasser, H.-M.
Measurement of gas fraction, gas velocity and volume flow by electrode mesh sensors
ECCE 2 - Second European Congress of Chemical Engineering - Montpellier 05.-07.10.1999, paper CD-ROM 11280001.pdf.

Prasser, H.-M.
Messtechniken in der Zweiphasenströmung
Jahrestagung Kerntechnik 1999, Karlsruhe, 18.-20. Mai
Neue Ergebnisse aus F + E zur Fluiddynamik und Reaktorphysik,
Inforum Verlagsgesellschaft, Bonn, Juni 1999

Priede, J.; Gerbeth, G.
Oscillatory and rotational instabilities in electromagnetic levitation
Symposium „Fluid-Flow Phenomena in Metals Processing„ TMS Annual Meeting, San Diego, USA, February 27 - March 5, 1999
Fluid Flow Phenomena in Metals Processing, Eds.: N.El-Kaddah, D.G.C.Robertson, S.T.Johansen, V.R.Voller, The Minerals, Metals & Materials Society, Warrendale (USA), 1999, pp.593-601

Richter, H.; Böhmert, J.; Viehrig, H.-W.
The use of acoustic emission to determine characteristic dynamic strength and toughness properties of steel
Nuclear Engineering and Design 188 (1999), 241-254

Rindelhardt, U.
Auslegung und Erträge von netzgekoppelten Photovoltaik-Anlagen
Energie und Umwelt '99, 24.-25. März 1999, Freiberg, Tagungsband S. 81

Rohde, U.; Langenbuch, S.
Gekoppelte Berechnungen von Thermohydraulik und Neutronenkinetik
Jahrestagung Kerntechnik 1999, Karlsruhe, 18. - 20. Mai,
Neue Ergebnisse aus F+E zur Fluiddynamik und Reaktorphysik",
Inforum Verlagsgesellschaft, Bonn, Juni 1999

Schaffrath, A.; Fethke, M.; Ringel, H.
Experimentelle Untersuchungen zur Wirksamkeit passiver Komponenten für den SWR1000
atomwirtschaft - atomtechnik 44 (1999)1, S. 35-36

Schaffrath, A.; Fjodorow, A.; Gocht, U.; Krüssenberg, A.-K.
Vergleich von Modellen zur Berechnung der Kondensation in horizontalen Rohren
Jahrestagung Kerntechnik 1999, Karlsruhe, 18.-20. Mai, Tagungsbericht S. 111-115

Schaffrath, A.; Hicken, E. F.; Jaegers, H.; Prasser, H.-M.
Experimental and Analytical Investigation of the Operation Mode of the Emergency Condenser of the SWR1000
Nuclear Technology 126 (1999), May 1999, p. 123-142

Schaffrath, A.; Hicken, E. F.; Jaegers, H.; Prasser, H.-M.
Operation Conditions of the Emergency Condenser of the SWR1000
Nuclear Engineering and Design 188 (1999), p. 303-318

Schaffrath, A.; Krüssenberg, A.-K.; Fjodorow, A.; Gocht, U.; Lischke, W.
Modelling of Condensation in Horizontal Tubes
Ninth International Topical Meeting on Nuclear Hydraulics (NURETH-9),
San Francisco, California, 5th Oct 1999, CD-ROM

Schaffrath, A.; Krüssenberg, A.-K.; Lischke, W.; Gocht, U.; Fjodorow, A.
Comparative assessment of condensation models for horizontal tubes
Kerntechnik 64 (1999) 4, p. 204-208

Schneider, C.
Fluidmechanics of Electrolytic Cells
2nd Intern. Symposium "Two-Phase Flow Modelling and Experimentation",
Pisa, Italy, 23-26 May 1999, proceedings vol. 2, pp. 1085-1092

Schneider, C.
Two-phase flow in the anode chamber of alkaline chloride electrolysis cells
ECCE 2 - Second European Congress of Chemical Engineering - Montpellier 05.-07.10.1999, paper CD-ROM 09170010.pdf.

Stefani, F.; Gerbeth, G.
Velocity reconstruction in conducting fluids from magnetic field and electric potential measurements
Inverse Problems, 15 (1999), pp. 771-786

Stefani, F.; Gerbeth, G.
Velocity reconstruction in electrically conducting fluids from external electromagnetic measurements
APS Bulletin vol. 44, no. 4, pp. 106 (1999)

Stefani, F.; Gerbeth, G.; Galitis, A.
Velocity Profile Optimization for the Riga Dynamo Experiment
A. Alemany, Ph. Marty, .P. Thibault (ed.), Transfer Phenomena in Magnetohydrodynamic and Electroconducting Flows, Kluwer Academic Publishers, Dordrecht 1999, pp. 31-44

Viehrig, H.-W.; Böhmert, J.
Die Radionuklidlaboratorien zur Untersuchung bestrahlter Werkstoffproben im Institut für Sicherheitsforschung des Forschungszentrums Rossendorf
Jahrestagung Kerntechnik 1999, Karlsruhe,18.-20. Mai, Tagungsbericht S. 687 ff.

Viehrig, H.-W.; Böhmert, J.
Some Issues by Using the Master Curve Concept
Proc. of the 15th International Conference on Structural Mechanics in Reactor Technology (SMIRT-15), Seoul, Korea, August 1999, Vol. 5, p. 383-390

Viehrig, H.-W.; Böhmert, J.; Richter, H.
Common German/Russian Irradiation Experiment at Rheinsberg NPP - Results of the Mechanical Testing
IAEA Specialists Meeting Neutron Embrittlement and Mitigation, 26-29 April 1999, Madrid, Spain, IAEA Working Document IWG-LMNPP-99/2, pp. 271-282

Weier, T.; Fey, U.; Gerbeth, G.; Mutschke, G.; Gad-el-hak, M.
Control of Flow Separation from a Hydrofoil Using Lorentz Forces
DFD 99 Meeting of The American Physical Society APS Bulletin vol. 44, no. 4, pp. 164 (1999)

Weier, T.; Fey, U.; Gerbeth, G.; Mutschke, G.; Lielausis, O.; Platacis, E.
Electromagnetic flow control for drag reduction and separation prevention
Proceedings of the 11th European Drag Reduction Working Meeting, Prague, Sept. 15-17 1999, pp.84-85

Weier, T.; Fey, U.; Mutschke, G.; Gerbeth, G.; Lammers, G.; Lielausis, O.
Electromagnetic Control of Flow Separation
2nd International Conference on Marine Electromagnetics, July 5--7, 1999, p. 197-205

Other oral presentations

Altstadt, E.
Schwingungsmodellierung zur Unterstützung der Diagnostik an Druckwasserreaktoren
Sächsisches Kolloquium Technische Diagnostik, TU Dresden, 29.01.1999

Deerberg, G.; Wack, T.; Schmitt, W.; Kryk, H.; Bothe, H.; Hulzer, G.
Ermittlung kinetischer Parameter für eine heterogene katalysierte Mehrphasenreaktion
GVC/DECHEMA - Fachausschuss "Prozeß- und Anlagentechnik, Bad Honnef, 25./26. Oktober 1999

Eckert, S.; Gerbeth, G.; Guttek, B.; Stechemesser, H.; Lielausis, O.
Investigation of liquid metal two phase flow characteristics by means of local resistivity probes and X-ray screening technique
International Workshop on Measuring Techniques for Liquid Metal Flows (MTLM), Dresden, October 11-13, 1999

Eckert, S.; Witke, W.; Pisseloup, L.; Gerbeth, G.
Local velocity measurements in high temperature liquid metals by means of mechano-optical probes
International Workshop on Measuring Techniques for Liquid Metal Flows (MTLM) , Dresden, October 11-13, 1999

Fietz, J.
Rolle und Akzeptanz der Kernenergie in einem zukunftsfähigen Stromversorgungskonzept
VDI-KTG-Seminar, Dresden, 17.6.1999

Gerbeth, G.
Electromagnetic control of flow around bodies
Einladungsvortrag am LEGI Grenoble (04.02.1999)

Gerbeth, G.
Kontrolle der Nichtlinearen Dynamik von Strömungsgrenzschichten - Anwendung bei Schiffen
Statusseminar Nichtlineare Dynamik, Frankfurt, 23./24.02.1999

Höhne, T.
1:5 scaled Plexiglas Mixing Model of the PWR Konvoi
International Conference on Nuclear Engineering (ICONE-7), April 19-23,1999, Tokio, Japan

Lucas, D.
Erste Nachrechnungen von Druckentlastungsexperimenten bei durchgehender Reaktion mit dem Programm BRICK
47. Sitzung des DECHEMA/GVC-Arbeitsausschuß "Sicherheitsgerechtes Auslegen von Chemieapparaten", Frankfurt am Main, 9./10. März 1999

Lucas, D.
Investigations on Pressure Relief at Forschungszentrum Rossendorf
Presentation at the DIERS User Group meeting, Las Vegas, NV, April 14-16, 1999

Prasser, H.-M.
Meßtechniken in der Zweiphasenströmung
Vortrag am IKE des Forschungszentrums Karlsruhe am 04.05.1999

Prasser, H.-M.
Schnelle Gittersensoren für Gasgehalt, Gasgeschwindigkeit und Volumenstrom in einer Zweiphasenströmung
Seminarvortrag Universität GH Essen, 06. Mai 1999

Rindelhardt, U.
Windenergienutzung in Sachsen
Einladungsvortrag Graduiertenkolleg "Lokale innovative Energiesysteme", TU Dresden, 14.1.1999

Stefani, F.; Gerbeth, G.
An inverse problems approach to velocity reconstruction from measurements of electromagnetic fields
International Workshop on Measuring Techniques for Liquid Metal Flows (MTLM) Dresden, October 11-13, 1999

Willschütz, H.-G.
Applying ANSYS/Multiphysics to In-Vessel and Ex-Vessel Core Melt Phenomena
Seminar held at the Division of Nuclear Power Safety at the Royal Institute of Technology, Stockholm

FZR-Reports and other publications

Beyer, M.; Carl, H.; Kriks, J.
Unterstützung der ukrainischen Genehmigungs- und Aufsichtsbehörde bei der Einrichtung einer verbesserten betrieblichen Überwachung für das KKW Rovno (5. Realisierungsstufe)
Wissenschaftlich-Technische Berichte / Forschungszentrum Rossendorf; FZR-260 Mai 1999

Beyer, M.; Carl, H.; Nowak, K.; Schumann, P.; Seidel, A.
Unterstützung der ukrainischen Genehmigungsbehörde NARU beim Aufbau eines technischen Systems zur verbesserten betrieblichen Überwachung des KKW Saporoshje (4. Realisierungsstufe)
Wissenschaftlich-Technische Berichte / Forschungszentrum Rossendorf; FZR-259 Mai 1999

Böhmert, J.; Kryukov, A.; Nikolaev, Yu. A.; Korolev, Yu.; Erak, D. Yu.; Gerashenke, S.
Einfluß der Zusammensetzung auf die Strahlenversprödung von Eisenlegierungen
Wissenschaftlich-Technische Berichte / Forschungszentrum Rossendorf; FZR-255 Februar 1999

Gerbeth, G.; Eckert, S. (Editors)
International Workshop on Measuring Techniques for Liquid Metal Flows (MTLM), Rossendorf, 11.-13.10.99, Proceedings
Wissenschaftlich-Technische Berichte / Forschungszentrum Rossendorf; FZR-278 November 1999

Grundmann, U.; Mittag, S.; Rohde, U.
The 3-Dimensional Core Model DYN3D
Wissenschaftlich-Technische Berichte / Forschungszentrum Rossendorf; FZR-248 Januar 1999

Hensel, F.
Methodische Untersuchungen zum Einsatz von Positronenemittern für die Dichtebestimmung in leichten Medien
Wissenschaftlich-Technische Berichte / Forschungszentrum Rossendorf; FZR-254 Februar 1999

Hoppe, D.
Die Verknüpfung von Teilmodellen auf der Grundlage der Dimensionsanalyse
Wissenschaftlich-Technische Berichte / Forschungszentrum Rossendorf; FZR-263 Juni 1999

Prasser, H.-M.; Böttger, A.; Zschau, J.
Entwicklung von Zweiphasenmeßtechnik für vergleichende Untersuchungen zur Beschreibung von transienten Strömungen in Rohrleitungen
Wissenschaftlich-Technische Berichte / Forschungszentrum Rossendorf; FZR-233 Februar 1999

Prasser, H.-M. (Editor)
3. Workshop "Meßtechnik für stationäre und transiente Mehrphasenströmungen", 14. Oktober 1999 in Rossendorf
Wissenschaftlich-Technische Berichte / Forschungszentrum Rossendorf; FZR-281, Dezember 1999

Weiß, F.-P.; Rindelhardt, U. (Editors)
Institute of Safety Research; Annual Report 1998
Wissenschaftlich-Technische Berichte / Forschungszentrum Rossendorf; FZR-268 Juli 1999

Weiß, F.-P.; Rindelhardt, U. (Editors)
Institute of Safety Research Research; Report January 1998-June 1999
Wissenschaftlich-Technische Berichte / Forschungszentrum Rossendorf; FZR-273 September 1999

Willschütz, H.-G.
CFD-Calculations to a Core Catcher Benchmark
Wissenschaftlich-Technische Berichte / Forschungszentrum Rossendorf

Patents

Patents

Rindelhardt, U.; Teichmann, G.
Verfahren und Schaltungsanordnung zur Maximum-Power-Point-Steuerung von Solargeneratoren
Anmeldung: 4.2.1999

Eckert, S.; Witke, W.; Gerbeth, G.
Einrichtung zur lokalen Messung von Strömungsgeschwindigkeiten
Anmeldung: 25.3.1999

Stefani, F.; Gerbeth, G.; Cramer, A.; Eckert, S.; Thess, A.; Priede, J.
Einrichtung und Verfahren zur Bestimmung von räumlichen Geschwindigkeits-verteilungen in elektrisch leitfähigen Flüssigkeiten
Anmeldung: 14.5.1999

Prasser, H.-M.; Schlüter, St.; Dudlik, A.
Anordnung zur Verhinderung unerwünschter Drücke beim Absperren oder Drosseln der Flüssigkeitsförderung in einer Rohrleitung
Anmeldung: 24.8.1999

Lielausis, O.; Eckert, S.; Gerbeth, G.
Verfahren und Anordnung zur Steuerung der Größe der Gasblasen in elektrisch leitfähigen Flüssigkeiten
Anmeldung: 8.10.1999

Awards

Awards

Dr. V. Galindo, Dr. G. Gerbeth
Forschungspreis des FZR 1999
"Magnetfelder für Kristallzüchtungstechnologien - Theorie, Numerik und industrielle Umsetzung"

Dr. H.-M. Prasser
Technologiepreis des FZR 1999
"Entwicklung von Zwei-Phasen-Messtechnik"

Meetings and Workshops

Meetings and Workshops

AER Work Group Meeting
Rossendorf, 10.-12. Mai 1999

3d Meeting EU-Projekt "RESQUE"
Rossendorf, 27.-28. Mai 1999

CONDOR-Projekt
Meeting zum 5th EU-FWP
Rossendorf. 31. Mai - 01. Juni 1999

Betriebliche Fernüberwachung KKW Saporoshje
Rossendorf, 07.-11. Juni 1999

International Workshop on Measuring Techniques for Liquid Metal Flows (MTLM)
Rossendorf, 11.-13. Oktober 1999

3. Workshop "Messtechnik für stationäre und transiente Mehrphasenströmungen"
Rossendorf, 14.-15. Oktober 1999

IAEA-Meeting "Fine Group Spectrum Calculation and Comparison with Experimental Results"
Rossendorf, 25.-29. Oktober 1999

Seminars of the Institute

SEMINARS

Dr. J. U. Knebel (Forschungszentrum Karlsruhe)
Stand der Arbeiten zu einer beschleunigergetriebenen Anordnung (ADS) am Forschungszentrum Karlsruhe zur Transmutation von Aktiniden
14.01.99

Dr. P. Hübner (Bergakademie Freiberg)
Korrelation zwischen Kerbschlagarbeit und bruchmechanischen Kennwerten
28.01.99

M. Große
Beiträge zur Charakterisierung von bestrahlungsinduzierten Ausscheidungen in RDB-Stählen
11.02.99

Dr. D. Hoppe
Modellbildung durch Auswertung von Fehlerdimensionen
25.02.99

Dr. E. Franke, Dr. I. Reiche (VKTA Rossendorf)
Neutronentransportrechnungen für Reaktorkerne vom Typ WWER-440 mit dem Code HELIOS
11.03.99

Dr. D. Lucas
BRICK – ein 1D Simulationstool für Mehrphasenströmungen in Behältern
25.03.99

Dr. D. Parker (University Birmingham)
Application of PET and other positron tracer techniques in engineering and the physical sciences
31.03.99

D. Klotz (Gesellschaft für Strahlenforschung Neuherberg)
Experimente zum Schadstofftransport
08.04.99

Dr. Steinwarz (Siempelkamp, Nuklear- und Umwelttechnik GmbH & Co., Krefeld)
Repräsentative Experimente zur Beherrschung von Kernschmelzunfällen
20.04.99

Prof. F. Wagner (Max-Planck-Institut für Plasmaphysik Greifswald)
Die physikalischen Grundlagen des Fusionsprojektes Wendelstein - 7X
22.04.99

Dr. U. Fey
Experimente zur elektromagnetisch kontrollierten Körperumströmung
06.05.99

Dr. G. Grunwald
Experimente zur Kühlmittelvermischung in Druckwasserreaktoren
03.06.99

T. Willms
Kalorimetrische Untersuchungen zur Kinetik der Alkoholyse von Acylchloriden
15.06.99

H.-G. Willschütz
Simulation der Thermofluiddynamik einer segregierten Metall-Oxid-Schmelze
17.06.99

G. Hessel, Dr. W. Schmitt, Dr. H. Kryk
Reaktionskinetische Untersuchungen mittels FTIR-Spektroskopie
01.07.99

Dr. G. Manturov, (Institute of Physics and Power Engineering, Obninsk, Russia)
Works on civil uses of Plutonium from dismantled Russian nuclear weapons
22.07.99

Dr. E. Pridöhl (FhG-EADQ Dresden)
Zerstörungsfreie Prüfung als Werkzeug der Qualitätssicherung
23.09.99

Dr. E. Steichele (TU München)
Der neue Forschungsreaktor FRM II und seine wissenschaftliche und praktische Nutzung
07.10.99

Dr. P. Satyamurthy (Liquid Metal MHD Section, Bhaba Atomic Research Centre Mumbai/India)
Two-Fluid Model for Liquid Metal MHD Power Systems
19.10.99

Dr. G. Grunwald, Dr. H.-M. Prasser, T. Höhne
Experimente und Rechnungen zur Kühlmittelvermischung beim Anlaufen der Kühlmittelzirkulation in einem DWR
21.10.99

Dr. S. Zaritsky (RRC Kurchatov-Institute, Moscow), Dr. B. Osmera (NRI Rez)
Results and new requirements in VVER RPV dosimetry
28.10.99

Dr. U. Grundmann
3D nodale Methode HEXNEM zur Lösung der Neutronendiffusionsgleichung in hexagonaler Geometrie
04.11.99

Dr. S. Eckert
Messtechnik für Flüssigmetallströmungen
18.11.99

Dr. A. Krüssenberg, Dr. A. Schaffrath
Modellierung des Containments des KKW Stade - Vorarbeit für Rechnungen mit dem Programm RALOC
09.12.99

Prof. E. F. Hicken (FZ Jülich)
Betriebserfahrungen mit der NOKO-Versuchsanlage und experimentelle Ergebnisse zur Wirksamkeit von passiven Sicherheitssystemen
10.12.99

Dr. H.-M. Prasser, Dr. E. Krepper
Experimente und numerische Simulation zu turbulenten Zweiphasenströmungen in Rohren
16.12.99

Lecture Courses

Lectures

Frank-Peter Weiß
Zuverlässigkeit und Sicherheit technischer Systeme
TU Dresden, Fakultät Maschinenwesen
SS 99 und WS 99

Udo Rindelhardt
Erneuerbare Energien I und II
Universität Leipzig, Fakultät für Physik und Geowissenschaften
SS 99 und WS 99

Departments of the Institute

Institute of Safety Research

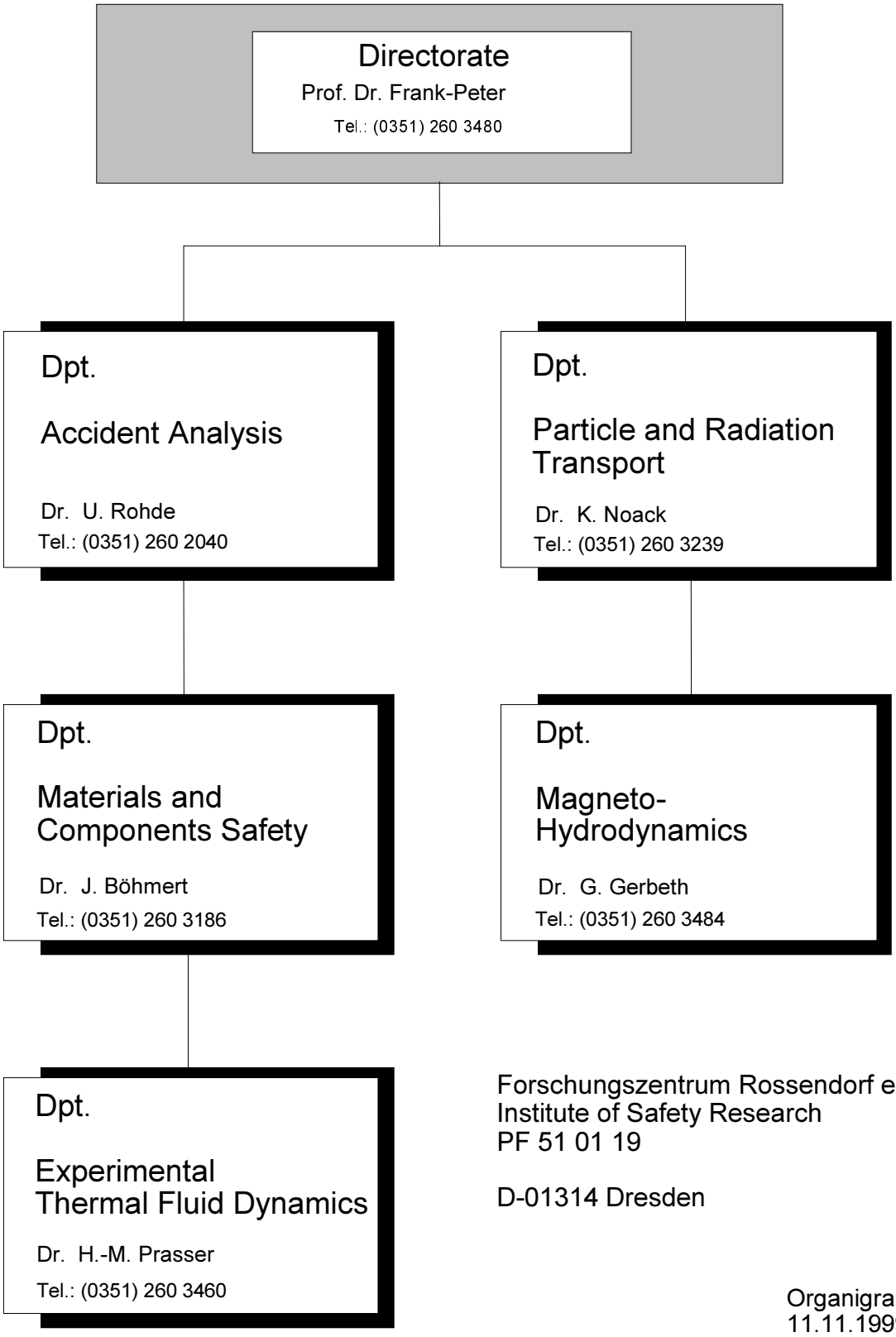

Forschungszentrum Rossendorf e.V.
Institute of Safety Research
PF 51 01 19

D-01314 Dresden

Organigram
11.11.1999

Personnel

Director: Prof. Dr. F.-P. Weiß

Scientific Staff

Altstadt, Eberhard Dr.
Beyer, Matthias
Böhmer, Bertram
Böhmert, Jürgen Dr.
Carl, Helmar Dr.
Cramer, Andreas Dr.
Eckert, Sven Dr.
Fey, Uwe Dr.
Fietz, Jürgen Dr.
Galindo, Vladimir Dr.
Gerbeth, Günter Dr.
Grants, Ilmars Dr.
Große, Mirco
Grundmann, Ulrich Dr.
Grunwald, Gerhard Dr.
Hensel, Frank, Dr.
Hessel, Günter
Hoppe, Dietrich Dr.
Hüller, Jürgen Dr.
Kliem, Sören
Koch, Reinhard Dr.
Konheiser, Jörg
Krepper, Eckhard Dr.
Krüssenberg, Anne-Kathrin Dr.
Kryk, Holger Dr.
Küchler, Roland Dr.
Lindau, Bernd Dr.
Lucas, Dirk Dr.
Mittag, Siegfried Dr.
Mössner, Thomas
Müller, Gudrun Dr.
Mutschke, Gerd
Noack, Klaus Dr.
Prasser, Horst-Michael Dr.
Richter, Holger
Rindelhardt, Udo PD Dr.
Rohde, Ulrich Dr.
Schaffrath, Andreas Dr.
Schmitt, Wilfried Dr.
Schäfer, Frank
Seidel, Andre
Seiler, Torsten
Stephan, Ingrid Dr.
Stephani, Frank Dr.
Teichmann, Günther
Viehrig, Hans-Werner Dr.
Werner, Matthias Dr.
Willms, Thomas Dr.
Willschütz, Hans-Georg
Witke, Willy
Zschau, Jochen Dr.

PhD Students

Batic, Davide
Beckert, Carsten
Grahn, Alexander
Höhne, Thomas
Kern, Tommy
Kliem, Margarita
Repp, Thomas
Schneider, Carola
Ulbricht, Andreas
Weier, Tom

Technical Staff

Baldauf, Dieter
Behrens, Sieglinde
Blumentritt, Thea
Bombis, Doris
Borchardt, Steffen
Böttger, Arnd
Eichhorn, Christine
Erlebach, Stephan
Forker, Klaus
Futterschneider, Hein
Gundrum, Thomas
Kunadt, Heiko
Leonhardt, Wolf-Dietrich
Leuner, Bernd
Losinski, Claudia
Mansel, Catrin
Nowak, Bernd
Opitz, Ruth
Otto, Gerlind
Pietzsch, Jens
Richter, Annett
Richter, Henry
Richter, Joachim
Richter, Karl-Heinz
Richter, Petra
Rott, Sonja
Russig, Heiko
Schleßiger, Heike
Schneider, Gisela
Schütz, Peter
Seidler, Christa
Skorupa, Ulrich
Tamme, Marko
Tamme, Günther
Utke, Holger
Webersinke, Steffen
Weiß, Rainer
Zimmermann, Wilfried
Zippe, Winfried Dr.
Zippe, Cornelius Dr.